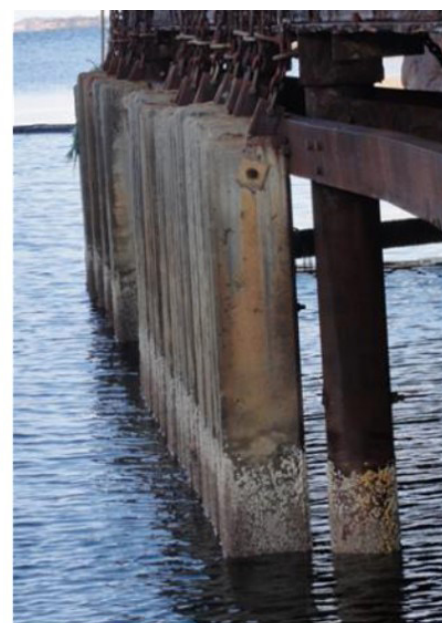


Field station Sandnessjøen

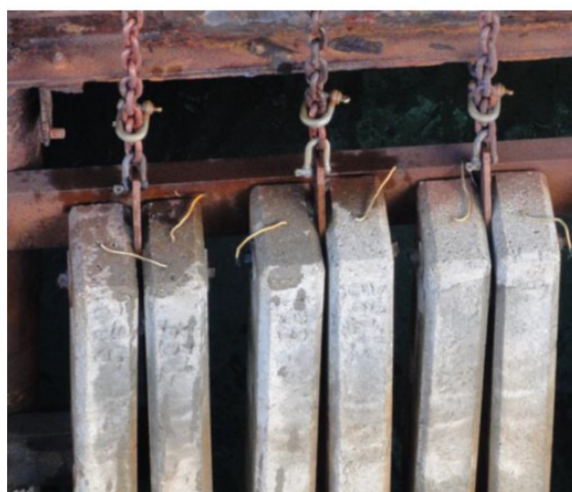
Effect of cracks in concrete after 25 years - Data report

STATENS VEGVESENS RAPPORTER

Nr. 374



Tobias Dammer



Tittel

Feltstasjon Sandnessjøen

Undertittel

Effekt av riss i betong etter 25 år - Datarapport

Forfatter

Tobias Danner, Andres Belda Revert, Mette Rica Geiker (NTNU)

Avdeling

Konstruksjoner

Seksjon

Konstruksjonsteknikk

Prosjektnummer

L10078

Rapportnummer

Nr. 374

Prosjektleder

Bård Magne Pedersen

Godkjent av

Karla Hornbostel

Emneord

betong, riss, armeringsstoler, langtids marin eksponering, armeringskorrosjon, selvreparasjon

Sammendrag

Tre opprissede betongbjelker støpt med forskjellige bindemiddelsammensetninger ble undersøkt etter 25 års marin eksponering ved feltstasjon Sandnessjøen. Betongbjelkene ble undersøkt med tanke på effekten av riss på inntrengning av sjøvann (klorider, sulfat) og armeringskorrosjon. I tillegg ble selv-reparasjon av riss undersøkt med tanke på effekt av bindemiddelsammensetning og eksponeringszone (atmosfærisk, tidevann, neddykket). Dypere kloridinntrengning ble observert ved riss; men samtidig ble det funnet lite korrosjon ved riss. Betydelig korrosjon (groptæring) ble kun funnet lokalisert ved armeringsstoler. Evnen til selvreparasjon av riss gjennom utfelling av kalsium- og magnesiumrike mineraler ble funnet å være uavhengig av bindemiddelsammensetning.

Title

Field station Sandnessjøen

Subtitle

Effect of cracks in concrete after 25 years - Data report

Author

Tobias Danner, Andres Belda Revert, Mette Rica Geiker (NTNU)

Department

Structures

Section

Structural engineering

Project number

L10078

Report number

No. 374

Project manager

Bård Magne Pedersen

Approved by

Karla Hornbostel

Key words

concrete, cracks, spacers, long-term marine exposure, reinforcement corrosion, self-healing

Summary

Three pre-cracked concrete beams prepared with different binders were investigated after 25 years' marine exposure at the field station Sandnessjøen, Norway. The concrete beams were investigated with respect to the impact of cracks on ingress and reinforcement corrosion. Furthermore, the impact of binder type and exposure (atmospheric, tidal, submerged) on the self-healing ability of cracks was investigated. Deeper chloride ingress was observed at cracks; however, minor corrosion was only found at two cracks in the tidal zone. Severe pitting corrosion was found at spacers. There was no impact of the binder type on the extent of self-healing and the composition of the self-healing products. The main mechanism of self-healing appeared to be precipitation of magnesium and calcium rich phases.



Field station Sandnessjøen

Effect of cracks in concrete after 25 years - Data report

Date: March 2020

Authors: Tobias Danner (NTNU/SINTEF)
Andres Belda Revert (NTNU/Norconsult)
Mette Rica Geiker (NTNU)

NTNU: Department of Structural Engineering, Norwegian University of Science and Technology, Trondheim, Norway

SINTEF: SINTEF Community, Architecture, Materials and Structures, Trondheim, Norway

Norconsult: NORCONSULT AS, Oslo, Norway

Sponsor: Norwegian Public Roads Administration (NPRA)
Statens vegvesen
Pb. 1010 Nordre Ål
2605 Lillehammer, Norway

Project name: “Ferry-free coastal route E39”, subproject 7.1.1 Influence of crack width on the durability of reinforced concrete structures (*Betydning av krav til rissvidder og trykkavlastning for bestandighet av armerte betongkonstruksjoner*)
The beams were prepared and exposed as part of the internal NPRA R&D project “Utvikling av kloridbestandig betong”, (Development of chloride resistant concrete)

Project no: NTNU: 25135402

Preface

The work documented in this report was performed within the project WP 7.1.1 “Relevance of crack width and decompression requirements (limits) due to durability aspects of conventional reinforcement”, which is part of the “Ferry-free coastal route E39” project initiated by the Norwegian Public Roads Administration (NPRA). Mette Geiker (NTNU) is the project leader of WP 7.1.1.

Through a collaboration with NPRA, NTNU got access to three concrete beams. The concrete beams were exposed for 25 years to seawater at NPRA's field station near Sandnessjøen. The beams are part of a R&D project initiated by NPRA named “Utvikling av kloridbestandig betong” (Development of chloride resistant concrete).

If not mentioned specifically, all measurements were performed or supervised by Tobias Danner (NTNU, now SINTEF Community).

The concrete beams were removed from the field station and transported to NTNU, Trondheim under the supervision of Karla Hornbostel (NPRA).

Karla Hornbostel (NPRA) and Eva Rodum (NPRA) participated in the planning of the investigations, the initial visual investigation and the electro-chemical potential, resistivity and moisture measurements.

Drilling and cutting of concrete beams and cores as well as quantitative chloride analysis and standard moisture and porosity measurements (drying at 105°C and relative humidity) were performed by SINTEF Community, Trondheim. Supplementary moisture measurements were performed at by Tobias Danner.

Andres Belda Revert (NTNU, now Norconsult AS) participated in investigations and reporting on the extent of reinforcement corrosion.

Parts of the investigations were undertaken by Solveig Larsen Myklebust and Ragnhild Moastuen, in connection with their master project at NTNU.

Besides this report, data retrieved from the three investigated concrete beams is published in two research articles:

- Geiker, M., Danner T., Michel A., Revert A.B., Linderoth O., Hornbostel K., "25 years' field exposure of pre-cracked concrete beams; combined impact of spacers and cracks on reinforcement corrosion", submitted to Cement and Concrete Research, February 2020
- Danner T., Jakobsen U.H., Geiker M., "Mineralogical sequence of self-healing products in cracked marine concrete, Minerals", Vol. 9, No. 5, pp.: 284-304, 2019

Acknowledgement

This research was part of the Norwegian Public Roads Administration (NPRA) “Ferry-free coastal route E39” project. The beams were prepared and exposed as part of the internal NPRA R&D project “Utvikling av kloridbestandig betong”, (Development of chloride resistant concrete). Professor Klaartje De Weerd, NTNU, is acknowledged for discussions on the application and interpretation of μ -XRF analysis and obtaining funding for the apparatus.

Summary

In 1993, the Norwegian Public Roads Administration (NPRA) established the test program “Utvikling av kloridbestandig betong” (Development of chloride resistant concrete). Concrete elements with 17 different concrete compositions are exposed at four field stations in Norway; Sandnessjøen field station being one of them.

In the present study, three pre-cracked concrete beams prepared with different binders were investigated:

- B: Portland cement + 4% silica fume
- E: Portland cement + 4% silica fume and 20% fly ash
- F: Portland cement + 12% silica fume

After 25 years marine exposure the beams were removed from the field station and sent to Trondheim. The exposure is divided into three zones: atmospheric, tidal and submerged. However, due to the limited length of the beams (3 m), the exposure in the atmospheric zone includes splash. The impact of cracks on chloride ingress and reinforcement corrosion was investigated determining, among others, chloride ingress, concrete resistivity, half-cell potentials, and state of reinforcement by excavating the reinforcement from the concrete. The effect of binder and exposure on the self-healing ability of cracks was studied using micro x-ray fluorescence (μ -XRF). The following observations were made.

Impact of cracks on ingress

- A white precipitate was observed in all zones on the crack surfaces and at the steel-concrete interface near cracks, indicating the ingress of seawater
- At cracks in the tidal zone (width 0.15-0.20 mm), deeper chloride ingress was observed with μ -XRF at cracks compared to the bulk of the concrete.
- At cracks in the atmospheric and submerged zone (width 0.075-0.10 mm), indications of deeper ingress were observed at cracks
- Sulphate and chloride were observed along cracks and the steel-concrete interface at the reinforcement.

Impact of multiple horizontal cracks on reinforcement corrosion

- Besides severe pitting at spacers (mainly in the tidal zone), the reinforcement was in general in good condition
- Minor corrosion was observed at in total two cracks, both in the tidal zone.

Impact of exposure and binder type on self-healing ability of cracks

- Substantial self-healing was observed in all exposure zones and for all binder types
- The main mechanism of self-healing seems to be precipitation of magnesium and calcium rich phases
- The precipitation of magnesium and calcium rich phases appears independent of the exposure (atmospheric, tidal, submerged)
- There was no indication of an impact of the binder type on the extent of self-healing and composition of the self-healing products.

List of content

Preface.....	i
Acknowledgement	ii
Summary	iii
1. Background and objectives.....	1
2. Field Station Sandnessjøen.....	2
3. Concrete Beams.....	4
4. Concrete cores	8
5. Investigations.....	12
5.1 Visual inspection and surface crack width measurements	13
5.2 Cover measurements.....	14
5.3 Half-cell potential measurements	14
5.4 Resistivity measurements	14
5.5 Carbonation depth measurements.....	14
5.6 Moisture and porosity measurements	15
5.7 Chloride ingress depth measurements	16
5.8 Chloride profiles measurements	16
5.9 Elemental mapping using μ -XRF.....	16
5.10 Degree and composition of self-healing in cracks.....	16
5.11 Excavation of reinforcement, characterisation of pits and estimation of corrosion rate 17	
6. Results	19
6.1 Visual appearance, crack width and concrete cover.....	19
6.1.1 Concrete beams.....	19
6.1.2 Concrete cores.....	23
6.2 Half-cell potential	24
6.3 Resistivity	27
6.3.1 Concrete beams.....	27
6.3.2 Concrete cores.....	27
6.4 Carbonation depth.....	28
6.5 Moisture and porosity	30
6.6 Chloride ingress	33
6.6.1 Chloride profiles	33
6.6.2 μ -XRF chloride maps.....	34
6.6.2.1 Unreinforced cracked and uncracked concrete cores	34

6.6.2.2	Spacers	37
6.7	Precipitation on crack surfaces and along reinforcement	40
6.8	Self-healing of cracks	43
6.8.1	Degree of self-healing	43
6.8.2.	Composition of self-healing products	47
6.9	Extent of reinforcement corrosion	53
	References	58

List of appendices

Appendix 1: Drawings of the concrete beams	61
Appendix 2: Location of concrete cores	62
Appendix 3: Pictures of top surface of concrete beams	65
Appendix 4: Half-cell potential measurements	68
Appendix 5: Resistivity	74
Appendix 6: Moisture – Raw data and comparison of different methods	77
Appendix 7: Chloride profiles	93
Appendix 8: Ingress of chloride and sulfate in cracks and along reinforcement	94
Appendix 9: Overview and detailed pictures of self-healing in cracks	99
Appendix 10: Steel-concrete interface	105

1. Background and objectives

NTNU collects long-term field data to study the extent of corrosion at and near cracks. This was a central activity in project WP 7.1.1 “Relevance of crack width and decompression requirements (limits) due to durability aspects of conventional reinforcement”, which is part of the “Ferry-free coastal route E39” project initiated by Norwegian Public Roads Administration (NPRA).

Corrosion propagation in cracked concrete is not fully understood and contradicting conclusions are reached based on short- and long-term observations [1-4]. There is consensus that cracks promote the ingress of CO₂ and chloride ions and thus facilitate corrosion initiation of exposed reinforcement in cracks. However, the impact of cracks on corrosion propagation is still not clear. Thus, there is a need for detailed investigations and long-term data to improve the understanding of the mechanisms of propagation of corrosion of steel reinforcement embedded in cracked concrete as well as documentation of the performance.

Self-healing is often suggested as a potential reason for the limited long-term impact of cracks on corrosion propagation sometimes observed. For autogenous self-healing to occur, the presence of water is the most important factor [5]. Thus, limited self-healing is expected in the atmospheric zone compared to the submerged zone. Faster self-healing was observed in mortars exposed cyclically to an aqueous solution, compared to mortars continuously immersed [6]. Some short-term laboratory studies showed a positive effect of cement substitution by fly ash on self-healing in mortars [7-9]. In contrast, it was shown that the addition of silica fume might reduce the ability of concrete to self-heal [10, 11]. There is a lack of long-term field data available on the impact of exposure and binder type on self-healing of cracks.

In 1993, NPRA established a marine field station near Sandnessjøen. Concrete beams with 17 different concrete compositions are mounted from a ferry quay in marine exposure. The upper part of the beams is exposed to atmospheric/splash zone, the middle part of the beams is exposed to tidal changes and the lower part is permanently submerged in seawater. Some of the concrete beams are loaded to maintain open cracks.

The objectives of the present study are to investigate the long-term

- 1) impact of cracks on chloride ingress
- 2) impact of cracks on the extent of reinforcement corrosion
- 3) impact of exposure and binder type on self-healing ability of cracks.

Self-healing is used as a general term covering both self-healing and self-sealing.

2. Field Station Sandnessjøen

In 1993, NPRA established a test program called “Utvikling av kloridbestandig betong” (Development of chloride resistant concrete) by exposing concrete elements at four different field sites in Norway; Field Station Sandnessjøen being one of them. Elements of in total 17 different concrete compositions were prepared [12].

Of each concrete composition four (4) beams (3000 x 300 x 150 mm) were cast. One beam was crack free, one with closed cracks, and the two other beams were cracked and kept loaded to maintain open cracks. The cracks were produced and maintained by 3-point bending (Figure 1). Right after loading the beams in 1993, the distance between the cracks was 100-150 mm, the crack depth of 70-90 mm, and the crack width of 0.1-0.2 mm [12]. More details on the loading of the concrete beams can be found in the report from Holtmon and Isaksen, 1994 [12].

The beams are mounted from a quay near Sandnessjøen (Figure 2, Figure 3 and Figure 4). The mean water level is about at the middle of the beams and the tidal changes are between ± 0.5 to ± 1.4 m [13]. Information on temperature and precipitation can be obtained from yr.no and no.climate-data.org, respectively. In 2017 the minimum and maximum temperatures were -10 and 24°C, and the average temperature during the coldest and warmest month was -2 and 16°C. The monthly precipitation was 100-267 mm.

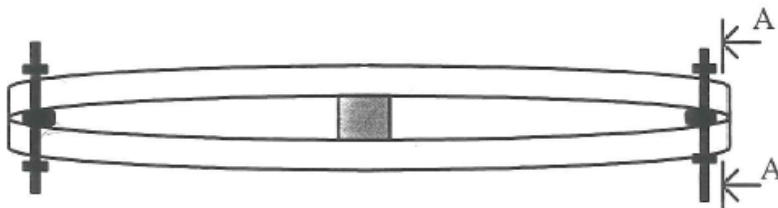


Figure 1: Illustration of coupling of 2 beams together in 3-point bending mode [12]



Figure 2: Location of field station near Sandnessjøen (gulesider/kart.no)



Figure 3: Field Station Sandnessjøen showing the concrete beams exposed to tidal water (14th March 2018 – Photo: Tobias Danner)



Figure 4: Concrete beams (concrete P, E, B and D from left to right) mounted from the ferry quay at the Field Station Sandnessjøen (14th March.2018 – Photo: Tobias Danner)

3. Concrete Beams

The 14th March 2018 between 09:00-11:00 a.m, three pairs of beams (concrete B, E and F; original marking BB1 and BB2, EB1 and EB2, FB1 and FB2) were taken out of the water with a crane. (Figure 5). Shells were partly removed from the concrete surface directly after lifting the beams out of the water. The beams were packed tightly in thick plastic foil (Figure 6) and transported to Trondheim the same day. The concrete beams were transported on an open truck and arrived in Trondheim around 19:00 the 14th March. The following day, the concrete beams were cleaned and moved into the laboratory.



Figure 5: Removal of a pair of concrete beams and preliminary surface cleaning (14th March.2018 – Photo: Tobias Danner)



Figure 6: Packing of concrete beams before transport to Trondheim (14th March 2018 – Photo: Tobias Danner)

In 2014, cores were drilled on one beam from each pair of concrete beams [14]. For the investigations of this report, only the “untouched” concrete beams were used. That means, from three pairs of concrete beams (6 beams) only 3 beams were investigated. From here on, the beams will be called Beam B, Beam E and Beam F for simplicity (original marking: BB2, EB2, FB1). The orientation of the investigated beams at the ferry quay was different as illustrated in Figure 7.

The concrete composition of the investigated beams is given in Table 1. The composition of the cement and fly ash used in the different concretes is given in Table 2. The exact composition of the fly ash used in cement MP30 in 1993 is not known. However, Norcem also supplied fly ash cement to a similar project of NPRA for a field station at Solsvik near Bergen in 1996 [15]. Norcem only uses class F fly ash according to ASTM C618-17a, and it is assumed that the composition of the fly ash did not change significantly between 1993 and 1996.

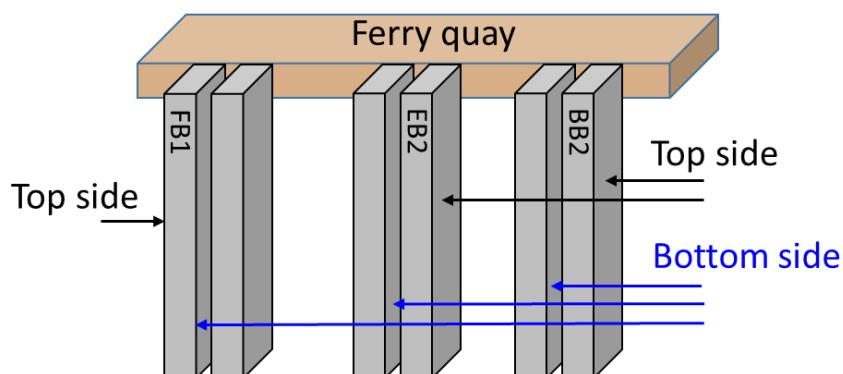


Figure 7: Illustration of orientation of investigated concrete beams at the ferry quay

Table 1: Composition of concrete used in Beam B, E and F

Component	Unit	Beam B	Beam E	Beam F
Cement (c)	kg/m³	373 (CEM I, Norcem P30)	384 (CEM II, Norcem MP30 ^a)	398 (CEM I, Norcem P30)
Silica fume (sf)	% (bwc)^b	4	4	12.5
Fly Ash (fa)^a	% (bwc)^b	-	(20) ^a	-
Free water (w)	kg/m³	160.5	166.6	198.7
Aggregate 0-8 mm	kg/m³	928	1014	881
Aggregate 0-19 mm	kg/m³	904	820	841
Air entrainer	kg/m³	0.3	0.6	0
Plasticizer	kg/m³	6.0	7.9	8.5
Paste volume	%	28.6	29.5	34.8
Theoretical density	kg/m³	2.38	2.40	2.37
Equivalent w/c^a	-	0.40	0.40	0.40

^a equiv. w/c = $w/(c+(k*sf))$; $k_{sf} = 2$; The fly ash was intermixed with the cement at the cement plant and thus part of the cement and given efficiency factor, $k_{fa} = 1$. The resulting fly ash cement was called CEM II, MP30.

^b bwc: by weight of cement

Table 2: Cement composition of cement (CEM I, P30 Norcem), fly ash and silica fume (composition of fly ash and silica fume used in parallel project [15])

Cement	Unit	CEM I	Fly ash	Silica fume
CaO (%)	wt%	63.3	3.6	0.1
SiO₂ (%)	wt%	20.6	55.4	95.1
Al₂O₃ (%)	wt%	4.8	27.4	1.0
Fe₂O₃ (%)	wt%	3.5	3.9	0.1
MgO (%)	wt%	2.2	1.0	0.4
SO₃ (%)	wt%	2.8		0.0
K₂O (%)	wt%	1.0	1.1	1.0
Na₂O (%)	wt%	0.35	0.3	0.1
LOI (%)	wt%	1.0	N/A	N/A
Free CaO (%)	wt%	1.1	N/A	N/A
Specific surface (m²/kg)	m ² /kg	341	N/A	N/A

N/A = not available

The concrete beams had a dimension of 3000 x 300 x 150 mm with truncated corners. Ribbed reinforcement bars with 16 mm diameter were used. One U-bended rebar providing two parallel legs (“Rebar 1” and “Rebar 2”) was used in each beam. The U-bend was facing up (in the atmospheric zone) where the beams were fastened; the bend is not shown in the sketches (e.g. Figure 12). The prescribed concrete cover was 25 mm from the top side and 75 mm from the sides (Figure 8). The position of the reinforcement in the concrete beams was located with a cover meter. The measured concrete cover was in agreement with the drawings. Plastic spacers were used to keep the reinforcement in place during casting of the beams.

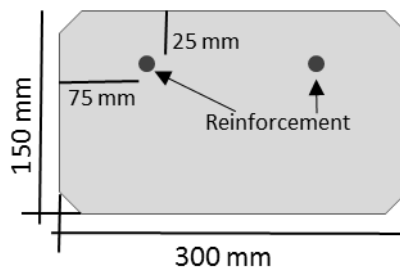


Figure 8: Illustration of top and bottom side on concrete beams (see also Figure 7). Measures in mm. Top side up.

The casting direction of the beams is illustrated in Figure 9. The drawings of the beams are given in Appendix 1.

Before moving the pairs of concrete beams in the laboratory, the concrete surfaces were cleaned outside. A pair of concrete beams before cleaning (as received at NTNU) is shown in Figure 10. The tidal and submerged zone are visible to the right in Figure 10 by shells covering the concrete surface. The concrete surface in the atmospheric zone was free of shells and algae. Remaining shells and algae were scratched off the surface with a big spatula before cleaning the concrete beams with water using a pressure washer (Figure 11).

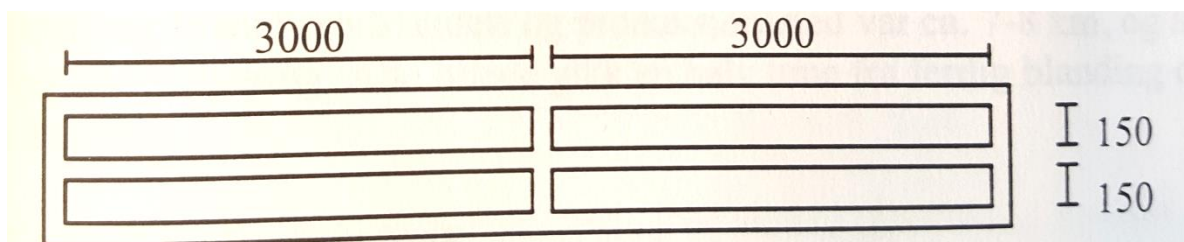


Figure 9: Illustration of formwork for casting of 2 pairs (2x2) concrete beams. Measures in mm [12]



Figure 10: Pair of loaded concrete beams as received at NTNU before cleaning the surface, submerged part of the beam to the right (15th March 2018 – Photo: Ragnhild Moastuen)



Figure 11: Surface cleaning of concrete beams. Left: Scratching of shells and algae; Right: Washing with pressure washer (15th March 2018 – Photo: Ragnhild Moastuen)

4. Concrete cores

Concrete cores with and without cracks were drilled between the reinforcement in all exposure zones. In addition, concrete cores were drilled with reinforcement in the tidal zone. The location of the drilled cores is illustrated in Figure 12. Table 4, Table 5 and Table 6 give an overview of the concrete cores taken from Beam B, Beam E and Beam F. An explanation of the core IDs is given in Table 3. Pictures of the core locations are given in Appendix 2. In between the different investigations, the concrete cores were packed tightly in plastic and stored in a 5°C room.

The concrete cores were drilled according to [16]. A water-cooled concrete drill was used. Concrete cores for chloride ingress, moisture measurements and sorption isotherms were taken with a concrete drill of 100 mm outer diameter. Cores taken in the tidal zone with cracks were taken with a concrete drill of 75 mm outer diameter. All concrete cores were drilled through the whole depth of the concrete beams, i.e. 150 mm. After drilling, the surface of the concrete cores was tapped dry with a moist cloth and the cores were packed in several layers of plastic and stored at $5 \pm 1^\circ\text{C}$. For concrete cores taken for moisture measurements, special care and fast treatment was applied.

Reference cores and cores with cracks were cut in two halves to get a flat surface for μ -XRF analysis. All cores were cut in the vertical direction of the beams; i.e. concrete cores with cracks were cut perpendicular to the crack. One half of each concrete core was taken for μ -XRF analysis, the other half of the uncracked cores was used for chloride profile grinding. A water-cooled concrete saw was used. Directly after cutting, the surfaces were tapped dry with a moist cloth and the cores were packed in plastic and stored at $5 \pm 1^\circ\text{C}$ in between measurements.

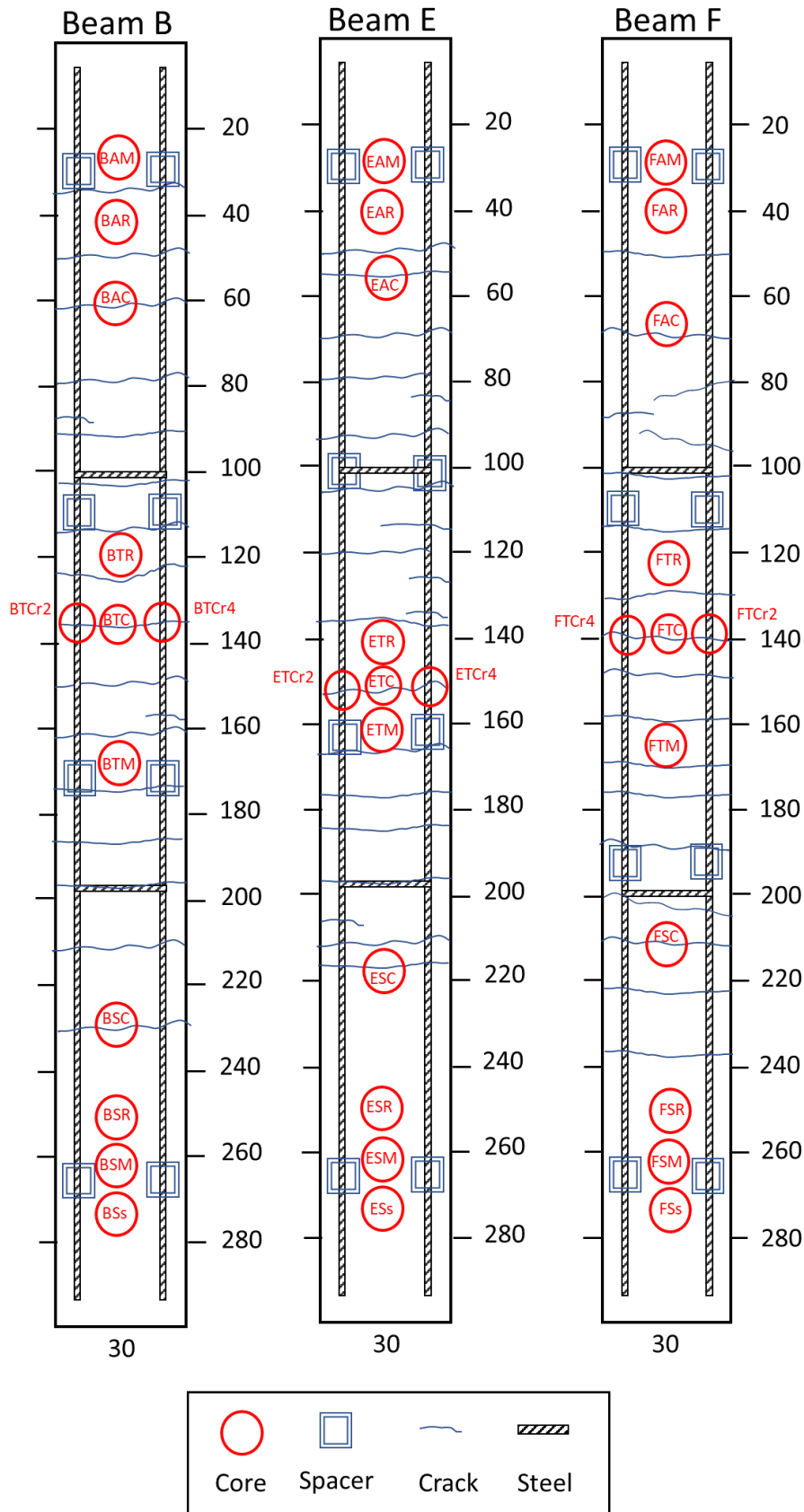


Figure 12: Location of concrete cores taken from Beam B, Beam E and Beam F. Note different orientation of Beam F at the ferry quay. Results of the visual inspection of the concrete beams is given in Chapter 5.1. Distance from the top in cm, width in cm

Table 3: Explanation of symbols used in Core IDs

Symbol	Position	Description
B, E, F	1	Concrete composition
A, T, S	2	Exposure zones (atmospheric, tidal, submerged)
R	3	Reference core (off crack)
C	3	Core taken on crack
M	3	Core for moisture measurements (off crack)
r	4	Core taken on reinforcement
s	3	Core taken for sorption isotherms

Table 4: Concrete cores taken from Beam B

Core ID	Exposure zone	Distance from top of atmospheric zone (cm)	Crack	Reinforcement
BAM	Atmospheric	30	-	-
BAR	Atmospheric	40	X	-
BAC	Atmospheric	60	-	-
BTR	Tidal	130	-	-
BTC	Tidal	140	X	-
BTCr2	Tidal	140	X	X
BTCr4	Tidal	140	X	X
BTM	Tidal	170	-	-
BSC	Submerged	230	-	-
BSR	Submerged	250	X	-
BSM	Submerged	260	-	-
BSs	Submerged	270	-	-

Table 5: Concrete cores taken from Beam E

Core ID	Exposure zone	Distance from top of atmospheric zone (cm)	Crack	Reinforcement
EAM	Atmospheric	30	-	-
EAR	Atmospheric	40	X	-
EAC	Atmospheric	60	-	-
ETR	Tidal	140	-	-
ETC	Tidal	150	X	-
ETCr2	Tidal	150	X	X
ETCr4	Tidal	150	X	X
ETM	Tidal	160	-	-
ESC	Submerged	220	-	-
ESR	Submerged	250	X	-
ESM	Submerged	265	-	-
ESs	Submerged	275	-	-

Table 6: Concrete cores taken from Beam F

Core ID	Exposure zone	Distance from top of atmospheric zone (cm)	Crack	Reinforcement
FAM	Atmospheric	30	-	-
FAR	Atmospheric	40	X	-
FAC	Atmospheric	70	-	-
FTR	Tidal	120	-	-
FTC	Tidal	140	X	-
FTCr2	Tidal	140	X	X
FTCr4	Tidal	140	X	X
FTM	Tidal	160	-	-
FSC	Submerged	210	-	-
FSR	Submerged	250	X	-
FSM	Submerged	260	-	-
FSs	Submerged	270	-	-

5. Investigations

Table 7 gives an overview of the investigations performed on concrete beams and the extracted concrete cores. Table 8 gives a summary of the timeline from removal of the concrete beams from the field station to the finalization of the investigations.

Five parallel lines were drawn over the whole length of the concrete beams in longitudinal direction (L1, L2, L3, L4, L5 in Figure 13). Line 2 and Line 4 were drawn above the reinforcement on the top surface of the beams. Line 3 was drawn in the middle of the top surface between the reinforcement of the beams. Line 1 and Line 5 were drawn above the reinforcement on the side surfaces of the concrete beams. The bottom side of the beams was not investigated. Crack width and half-cell potential was measured along lines L1-L5 as described in Chapter 5.1 and 5.3. Resistivity measurements were only taken on the top surface in between the reinforcement (Chapter 5.4). All results will be presented with the atmospheric zone on the left in case of horizontal oriented figures or top in case of vertical oriented figures.

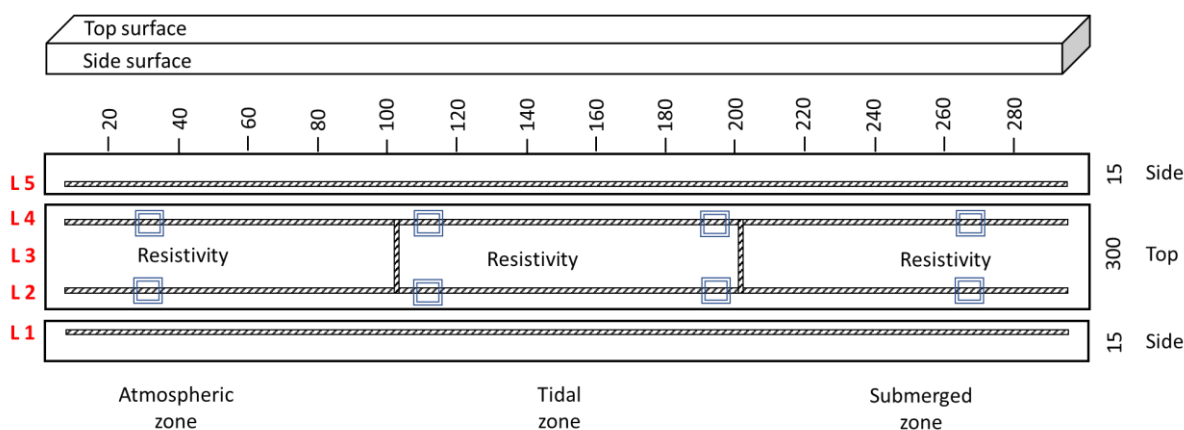


Figure 13: Template for crack mapping and experimental approach. Specific measurements were performed along five lines (L1-L5) on the side and top surface of the concrete beams. Measures in cm

Table 7: Overview of investigations performed on concrete beams and extracted concrete cores

Material	Property
Concrete beam	Visual appearance, crack width, concrete cover
	Half-cell potential (HCP)
	Resistivity
	Extent of corrosion
Concrete core	Visual appearance, crack width, self-healing
	Moisture and porosity
	Carbonation depth
	Crack width and depth
	Chloride ingress (quantitative)
	μ -XRF analyses: elemental distribution, chloride ingress (qualitative), self-healing of cracks

Table 8: Timeline of performed actions

Date	Action	Comment
13.03.2018	Removal of concrete beams from field station and transport to Trondheim	Packed in plastic, Temperature 1°C
14.03.2018	Arrival of concrete beams in Trondheim	Temperature 3°C
15.03.2018	Surface cleaning of concrete beams	Temperature 3°C
15.03.2018	Setting up of beams in the NTNU laboratory	Lab temperature 20°C
16.03.2018	Visual inspection. Measurement of concrete cover, half-cell potential (HCP), concrete resistivity, surface crack width	Equipment from Proceq, Cu/CuSO ₄ electrode, Wenner probe, temperature 20°C
16.03.2018	Packing of beams in plastic with small cups of water to maintain high humidity	Lab temperature 20°C
21.03.2018	Unloading pairs of concrete beams and repeated measurement of surface crack width	Lab temperature 20°C
21.03.2018	Moving beams to temperature-controlled room. From this date the beams were stored sealed at 5°C between examinations	Temperature 5°C
03.04.2018	Marking of locations for coring	
04.04.2018	Start of drilling and visual inspection of concrete cores (cores were stored sealed at 5°C)	Water-cooled concrete drill
09.04.2018	Start of moisture and porosity measurements	See methods and results for detailed information
10.04.2018	Cutting of concrete cores	Water-cooled concrete saw
12.04.2018	Examination of carbonation on concrete cores	See methods and results for detailed information
15.04.2018	Quantitative determination of chloride profiles	See methods and results for detailed information
18.04.2018	Crack width measurements on concrete cores	See methods and results for detailed information
April-June 2018	μ-XRF analyses: chloride ingress (qualitative), elemental mapping, analysis of cracks and self-healing	See methods and results for detailed information
June 2018	Investigation of the extent of corrosion	See methods and results for detailed information

5.1 Visual inspection and surface crack width measurements

The visual inspection included documentation of location of spacers, crack pattern, spalling, and precipitations.

The crack width was measured with a crack width ruler (accuracy 0.05 mm). The crack width was measured along all five lines (Figure 13). Additionally, the crack width was measured at several places after unloading the concrete beams. The crack pattern and surface crack width was documented in crack maps. The surface crack width was also measured on the surface of concrete cores after drilling.

5.2 Cover measurements

A covermeter from Proceq (Profometer) was used to locate the reinforcement in the concrete beams. The location of the reinforcement was drawn on the concrete surface to support later measurements of half-cell potential, concrete resistivity and surface crack width.

The cover measurements were checked when opening the beams.

5.3 Half-cell potential measurements

Half-cell potential measurements (HCP) were performed above the reinforcement according to [16]. The half-cell potential was measured with a Profometer wheel electrode collecting data every 5 cm. The potential was mapped above the reinforcement of the concrete beams along Lines L1, L2, L4 and L5 (see Figure 13). A copper–copper (II) sulphate electrode was used. To check the accuracy of the wheel electrode, the potential difference between the wheel electrode and a rod electrode (as well CSE) was measured. The difference was 3mV which is considered negligible.

5.4 Resistivity measurements

Resistivity measurements on the concrete beams were performed at selected areas of 40 cm x 10 cm on the top surface of the concrete beams in the atmospheric zone (20-60 cm), tidal zone (120-160 cm) and submerged zone (240-280 cm) (see Figure 13). The measurements were taken between reinforcement (around Line 3) at 20°C in the laboratory using a Proceq Resipod Wenner probe (4-electrode setup, 50 mm probe spacing). Twenty (20) resistivity measurements were taken and the average value was calculated.

Additional resistivity measurements were performed on concrete cores according to [17]. Metal-plates were placed on the two flat sides of the concrete cores with moist cloths between the metal plates and concrete surfaces. Tap water was used as contact solution. The electrode plates were coupled to an Agilent LCR meter and measurements were taken with a frequency of 100 and 120 Hz, 1 and 10 kHz. Measurements were taken at $5 \pm 1^\circ\text{C}$ in the cooling room where the concrete cores were stored.

It was found that resistivity is decreased with increased temperature and vice versa, and that the effect of temperature on resistivity depends on the moisture content in the concrete. Laboratory data indicate a resistivity change of 3% for saturated and 5% for dry concrete per degree Celsius change [18].

5.5 Carbonation depth measurements

The cylindrical surface of the newly drilled concrete cores and freshly split concrete when opening the beams were sprayed with pH indicator according to [17] to check possible pH changes due to carbonation or leaching. Instead of phenolphthalein, thymolphthalein was used as indicator. 1 g of the indicator (powder, grade “ACS, Reag. Ph Eur” (VWR)) was dissolved in a mix of 30 ml deionized water and 70 ml ethanol [19].

5.6 Moisture and porosity measurements

Figure 14 illustrates the utilization of concrete cores for moisture and porosity measurements. Concrete cores of 100 mm diameter and 150 mm length were taken from all three exposure zones of each concrete beam. The concrete cores were split in three slices of approximately 50 mm thickness each. Each slice was then split further into four parts. All steps were undertaken fast to reduce disturbance of the sample during subdivision. The arrow on the surface of the concrete cores indicated the orientation of the core towards the atmospheric zone in the concrete beam. The left side of each concrete core layer (quadrant II and III) was taken for degree of saturation and porosity measurements. Quadrant IV was used for a modified procedure of moisture measurements not described in this report. The upper right side of each concrete core (quadrant I) was reserved for RH measurements.

Degree of capillary saturation (DCS), and suction and macro porosity measurements were performed according to [17]. The following procedure was applied:

1. Splitting of concrete cores
2. Weighing of samples directly after splitting
3. Submersion in water and weighing in air after 7 and 21 days and in water after 7 days
4. Drying at 105 °C for 7 days
5. Submersion in water and weighing in air after 7 and 21 days and in water after 7 days
6. Submersion in pressure tank (50 mbar) for 2 days
7. Drying at 105 °C and weighing after 7 days

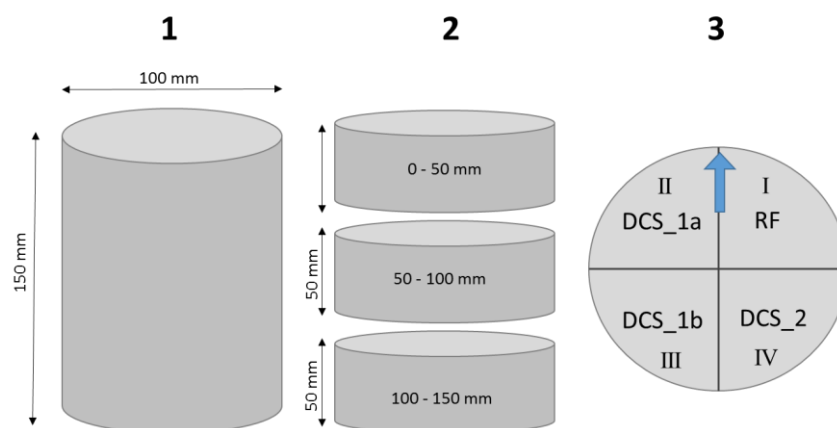


Figure 14: Principle drawing of utilization of concrete cores for moisture measurements. 1: Concrete cores of 100 mm diameter and 150 mm length; 2: Splitting of concrete cores in 3 layers (0-50 mm, 50-100 mm, 100-150 mm), 3: Splitting of each layer in 4 parts for DCS and RH (in figure RF) measurements

To investigate the effect of drying temperature on the measured DCS and suction porosity, an additional set of samples was measured in the following steps:

1. Splitting of concrete cores
2. Weighing of samples directly after splitting
3. Submersion in water and weighing in air and water after 21 days
4. Drying at 50°C for 21 days
5. Drying at 105°C for 21 days

Equations for calculation of DCS, suction and macro porosity are given in Appendix 6 together with the raw data.

The relative humidity (RH) was measured as described in [20]. For measurements of RH the samples were split to smaller pieces (max 5 mm) and aggregates were to the extent possible separated from the cement paste and discharged. Grains of cement paste were transferred into a test tube; filling half of the tube. The tube was placed in an isolated box in a climate-controlled room (20°C). Readings were performed daily for approximate a week, and the maximum value was used. For most of the samples the maximum value was observed after a few days of equilibrations; however, for unknown reasons some of the samples showed decreasing RH from the beginning (BAM, BTM, FAM; data marked with \geq). The RH was measured with calibrated Vaisala sensors “HM44”. The reported accuracy of the sensors is $\pm 2\%$ in the range of 0–90% RH and $\pm 3\%$ in the range of 90–100% RH [21].

5.7 Chloride ingress depth measurements

To check the chloride ingress depth, freshly cut or split concrete surface was sprayed with 0.1 M AgNO₃ solution according to [17]. However, for unknown reasons no sufficient contrast was obtained to make conclusions on the chloride ingress depth using this method.

5.8 Chloride profiles measurements

Profile grinding and chemical analysis was performed according to [17]. The layer thickness for profile grinding was 0-3, 3-6, 6-10, 10-15, 15-20, 20-30, 30-40, 40-50 mm. About 5g of the concrete powder of each layer was dried at 105°C overnight. The dried powder was dissolved in 50 ml 80°C (1:10) HNO₃ and filtrated after 1 h. The chloride content in the filtrated solution was determined by potentiometric titration with a Titrand 905 titrator from Metrohm using 0.01 M AgNO₃.

5.9 Elemental mapping using μ -XRF

Micro X-ray fluorescence (μ -XRF) elemental mapping and qualitative determination of chloride ingress were performed using a M4 Tornado from Bruker. The procedure was similar to the method described in [22]. Elemental mapping was performed at 50 kV accelerating voltage and 600 μ A with a silver X-Ray tube. Two silicon drift detectors were used simultaneously for fast data collection. Elemental mappings were performed with 80 μ m distance between each pixel and 1 ms/pixel collection time. The whole area of the taken concrete cores was mapped, i.e. 95 x 150 mm and 70 x 150 mm. Note that intensities are relative to the maximum intensities detected in each individual map.

5.10 Degree and composition of self-healing in cracks

Self-healing of cracks was studied with μ -XRF. The M4 Tornado is equipped with a camera of 10x and 100x magnification. Overview pictures of the cracks were taken with 10x magnification. Detailed pictures with 100x magnification were taken at different crack depth. The line scan tool of the μ -XRF software was used to measure the crack width at 100x magnification in steps of 5 mm from the concrete surface to the bulk of the concrete and the extent of self-healing was investigated visually. In selected areas, point measurements were

performed to study the composition of self-healing products. 3-5 measurements were taken in each area and average results are reported. Results are reported in atomic percent (atom%). Point measurements were acquired with 50 kV, 600 μ A and two detectors switched on. The measurement time was 30 sec per point with a spot size of 20 μ m.

5.11 Excavation of reinforcement, characterisation of pits and estimation of corrosion rate

The concrete cover was completely removed from the reinforcement to determine the extent of corrosion. First, the beams were cut in sections of about 50 cm in length. Then the beams were cut longitudinally from the bottom side following the reinforcement (Lines L2 and L4) to a depth of about 10 cm (without cutting the reinforcement), see Figure 15. Each of the 50 cm long pieces was then split along the cut notches. Pictures including the reinforcement imprint at Line L2 and L4 are presented in Appendix 11.

Corrosion pits were characterized by measuring the maximum depth and length. The corrosion rate was calculated based on two assumptions: a) maximum pit depth and length being representative for the whole length of the anodic site (see Figure 16 and Figure 17), b) constant and uniform corrosion development during the exposure period (25 years); c) cross section,. The first assumption leads to an overestimation of the corrosion rate, while the latter assumption leads to an underestimation, and the calculations should therefore only be taken as indicative.

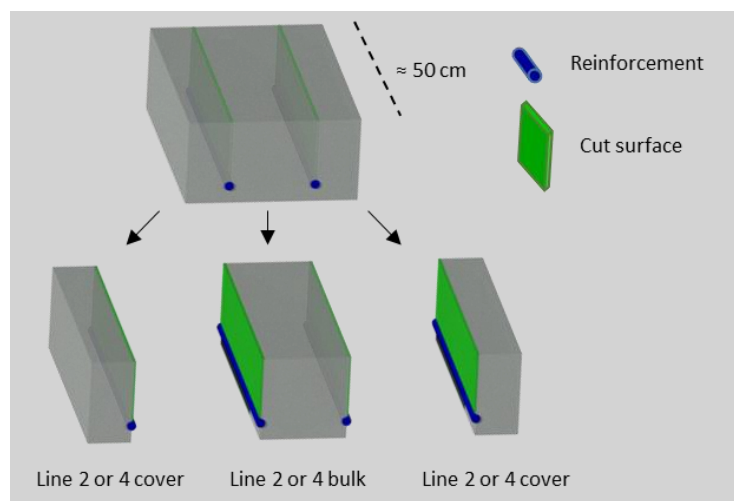


Figure 15: Illustration of cutting and removing the concrete cover for determination of extent of reinforcement corrosion

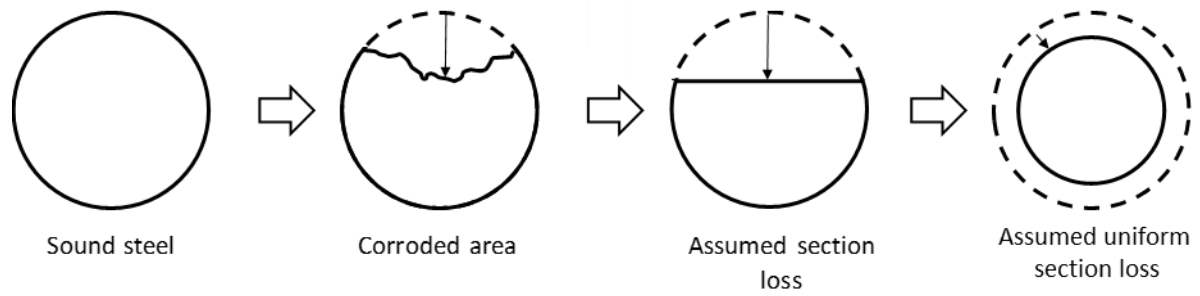


Figure 16: Cross section of rebar. Illustration of calculation of cross section loss based on measured maximum pit depth

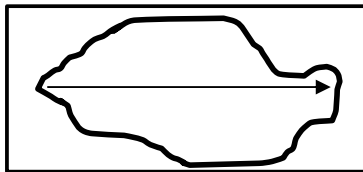


Figure 17: Longitudinal section of rebar. Illustration of determination of (maximum) pit length

6. Results

6.1 Visual appearance, crack width and concrete cover

6.1.1 Concrete beams

After moving the concrete beams to the laboratory, pictures of the top surfaces were taken with a digital camera (see Appendix 3).

The visual appearance of the beams, including possible spalling and cracks, is documented in crack maps. Explanations of the symbols used are given in Figure 18. Figure 19, Figure 20 and Figure 21 show crack maps of Beam B, Beam E and Beam F. Crack widths were measured on every crack along all 5 lines (L1-L5) (see Figure 13). After unloading, crack width measurements were repeated on the widest cracks. Within the accuracy of the measurement (0.05 mm) no change of the crack widths was observed after unloading. In between measurements, the concrete beams were packed in plastic and stored at 5°C.

The distance between cracks was 10-15 cm. In general, 15-17 cracks were found on the surface of each concrete beam. The crack depths measured on the sides of the concrete beams was 50-90 mm. The largest surface crack widths were measured in the middle of the beams (tidal zone). For concrete beams B and F, the largest observed crack width was 0.20 mm. For Beam E, the largest measured crack width was 0.35 mm. In the atmospheric and submerged zone, the crack width usually varied between <0.05 (marked as <) and 0.10 mm. Most cracks had a larger surface crack width between the reinforcement compared to above the reinforcement. No signs of corrosion were observed on the concrete surface at cracks. However, concrete spalling and corrosion products were observed at locations of spacers in concrete Beam B and F (see Appendix 3). In general, the crack mouth on the surface of the concrete beams appeared open (not sealed). However, in some locations the crack mouths were closed (see Figure 22); the approximate locations are marked with green in the crack maps of Figure 19 and Figure 20. Minor precipitate was observed around some cracks on the concrete surface most likely originating from leaching of the cement paste.

Concrete cover measurements were performed on the top surface of the concrete beams and the results are reported in [23]. The cover was in general 25 ± 2 mm. Larger variations were found in some places in the atmospheric and submerged zone due to disturbing signals from stirrups or overlapping reinforcement (see drawings in Appendix 1). Due to unknown reasons, high variations in cover were measured in Beam E (20-37 mm). However, when opening the concrete beam for investigations of the extent of corrosion, the cover was found to be around 25 mm in all places.

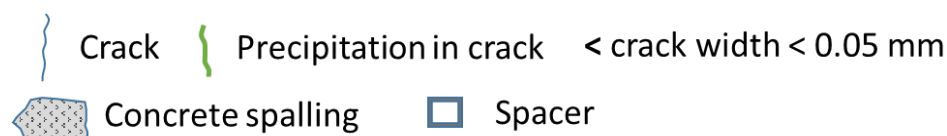


Figure 18: Explanation of symbols in crack maps

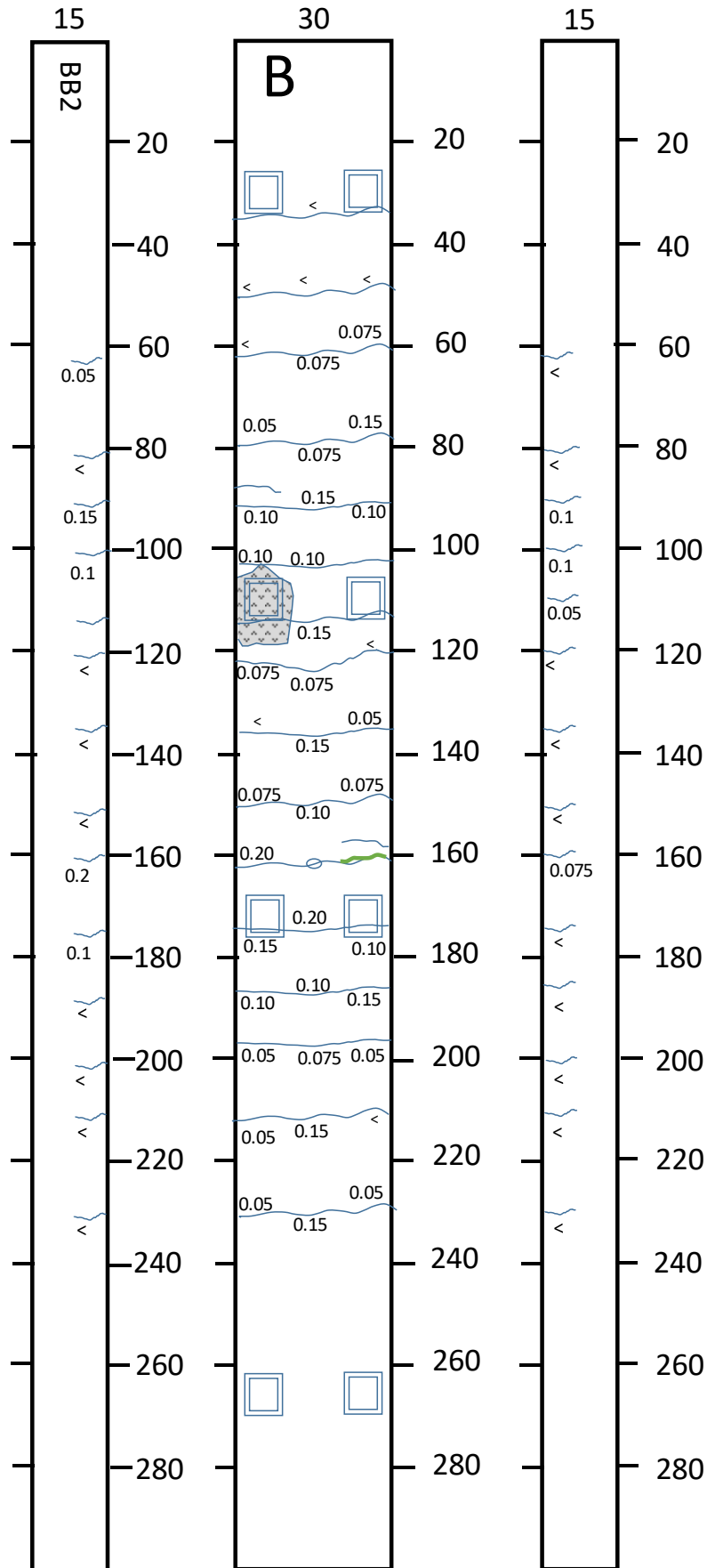


Figure 19: Crack map of Beam B (atmospheric zone at top). Distance from top in cm; crack width in mm. Legend in Figure 18

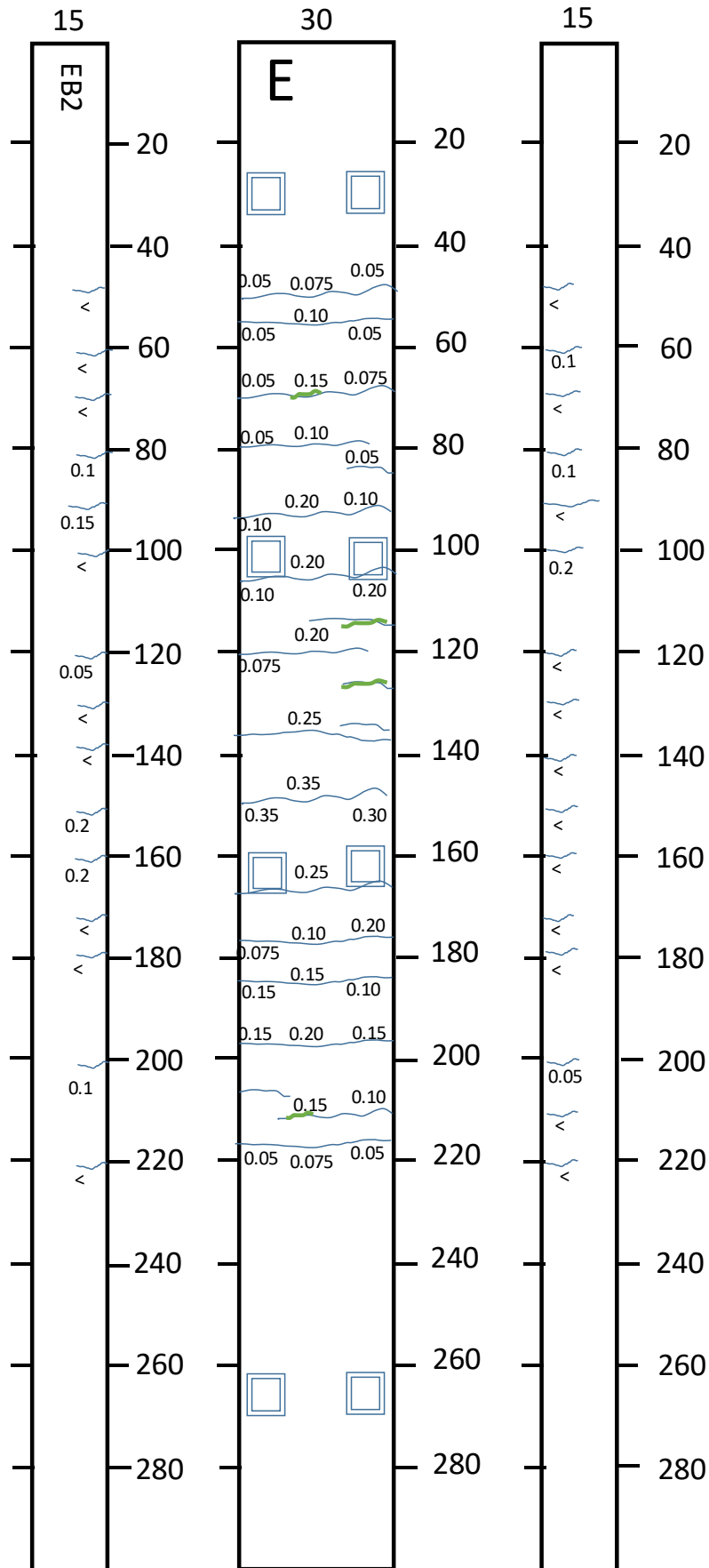


Figure 20: Crack map of Beam E (atmospheric zone at top). Distance from top in cm; crack width in mm. Legend in Figure 18

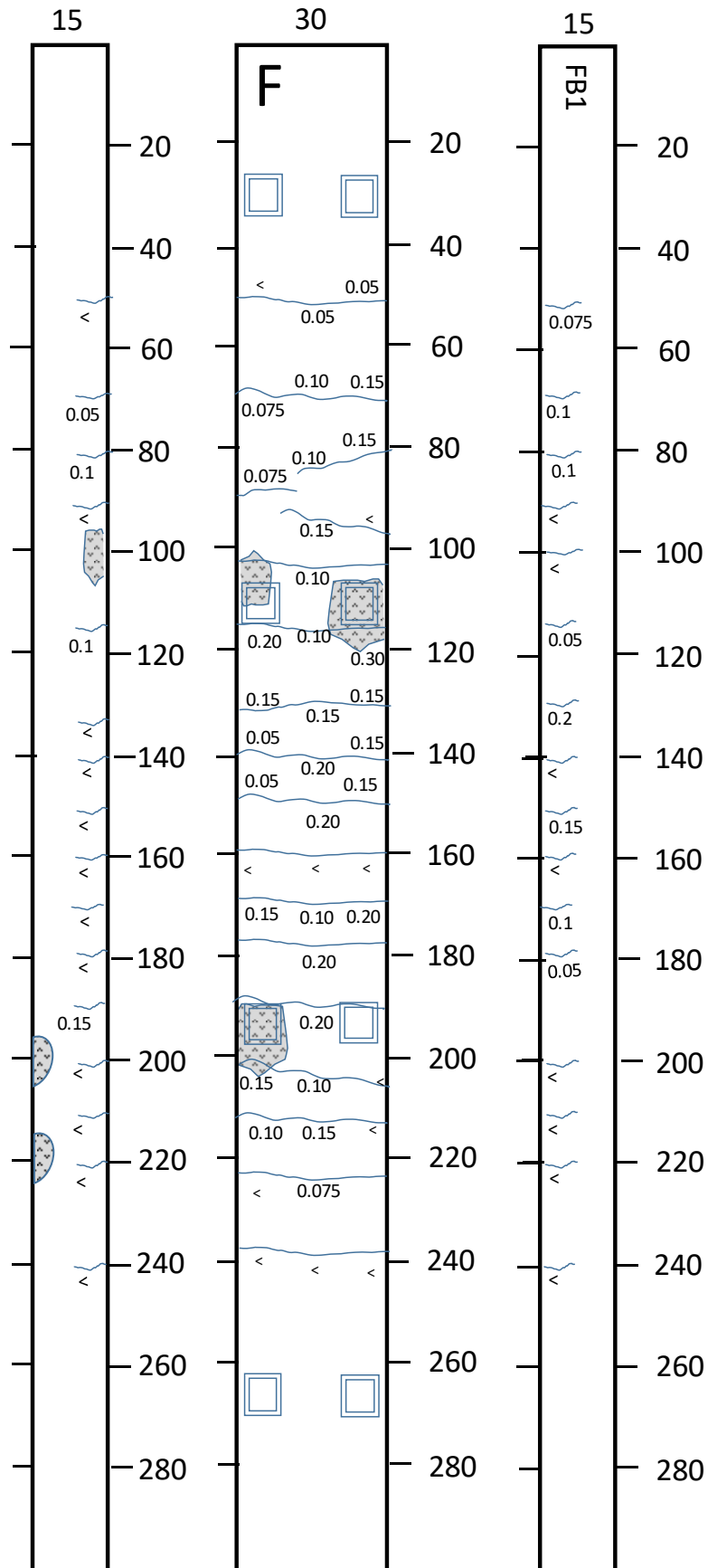


Figure 21: Crack map of Beam F (atmospheric zone at top). Distance from top in cm; crack width in mm. Note: different orientation on ferry quay (see Figure 7). Legend in Figure 18



Figure 22: Example of a partly closed crack mouth (marked with grey circle) next to an open crack on the surface of Beam E. Location: 80 cm

6.1.2 Concrete cores

After drilling the concrete cores, the surface crack width was measured at different places along the crack. The following results were recorded; a) on lines (L2, L3 and L4), b) maximum crack width, and c) average crack width (average of min. 5 measurements along the crack). The different crack widths and the crack depths on the left and right side of the concrete cores (cylindrical surface) is given in Table 9. The crack widths measured in the tidal zone of Beam E and F decreased when measured on the drilled concrete core surfaces compared to the crack width on the beam surface. Otherwise, there was no change in crack width.

Table 9: Surface crack width and crack depth measured on left and right side (cylindrical surface) of the concrete cores drilled with cracks, compared to surface crack width measured on the concrete beam before drilling the concrete cores

		Crack width (mm)			Crack depth (mm)
Beams		Cores			Cores
Core ID	On line	On line	Maximum	Average	(Left/right) ^a
BAC	0.075	0.05	0.10	0.075	n.v. ^b
BTC	0.15	0.15	0.20	0.15	(60/70)
BTCr2	0.05	0.05	0.075	0.075	(n.v./45)
BTCr4	0.05	0.15	0.20	0.15	(70/75)
BSC	0.15	0.075	0.15	0.10	(n.v./40)
EAC	0.10	0.075	0.075	0.075	n.v
ETC	0.35	0.25	0.30	0.20	(80/70)
ETCr2	0.35	0.30	0.30	0.25	(80/60)
ETCr4	0.30	0.20	0.25	0.20	(60/60)
ESC	0.075	<0.05	0.075	0.075	n.v
FAC	0.10	0.075	0.10	0.10	(30/30)
FTC	0.20	0.15	0.15	0.15	(70/30)
FTCr2	0.05	<0.05	0.10	0.10	(60/60)
FTCr4	0.15	0.10	0.15	0.10	(30/35)
FSC	0.15	<0.05	0.10	0.10	(20/20)

^a left and right (cylindrical surface) with orientation to top/atmospheric zone of concrete beam

^b n.v.: not visible

6.2 Half-cell potential

Figure 23, Figure 24 and Figure 25 show the results of half-cell potential mapping of the concrete beams. These measurements were taken with a wheel electrode from Proceq. Additional measurements were taken with a rod electrode on Line 2 (L2) and Line 4 (L4) for comparison. All measured values for wheel and rod electrode are given in tabular form in Appendix 4. The half-cell potentials measured with the wheel and rod electrodes were in general similar. However, it seems that small areas with a potential drop are more easily detected with the wheel electrode.

For all beams the potential was decreasing from atmospheric to submerged zone. A possible explanation is the different moisture content. Higher moisture content in the submerged zone results in decreased access of oxygen and thus leads to a decreased potential. Beam B and Beam F had potential values between -200 to -300 mV in the atmospheric zone and -400 to -500 mV in the submerged zone. The potential values of Beam E ranged between -50 to -200 mV in the atmospheric zone and -300 to -400 in the submerged zone. In Beam B, the potential appeared to decrease almost continuously from the atmospheric to the submerged zone with a short plateau in the tidal zone, between 100-180 cm distance from the top of the beam. In Beam

E and F, the potential decreased continuously from atmospheric to the tidal zone. Whereas in the lower tidal and submerged zone the potential values appeared almost constant.

In Line 2 on Beam B a peak of -500 mV was observed in the tidal zone. This peak coincides with a spacer (see Figure 19). Around the spacer, concrete spalling and signs of corrosion were observed (Appendix 3). Similarly, a smaller peak was observed at the location of a spacer at 30 cm in Line 2. Also on Beam F, potential drops were coinciding with concrete spalling and signs of corrosion around spacers at about 100 cm (Line 4) and 200 cm (Line 2) (see Appendix 3 and Figure 19). In addition, a peak of -320 mV on Line 4 at 30 cm coincided with the location of a spacer where no surface damage or corrosion was observed.

The results indicate ongoing corrosion at the location of the spacers.

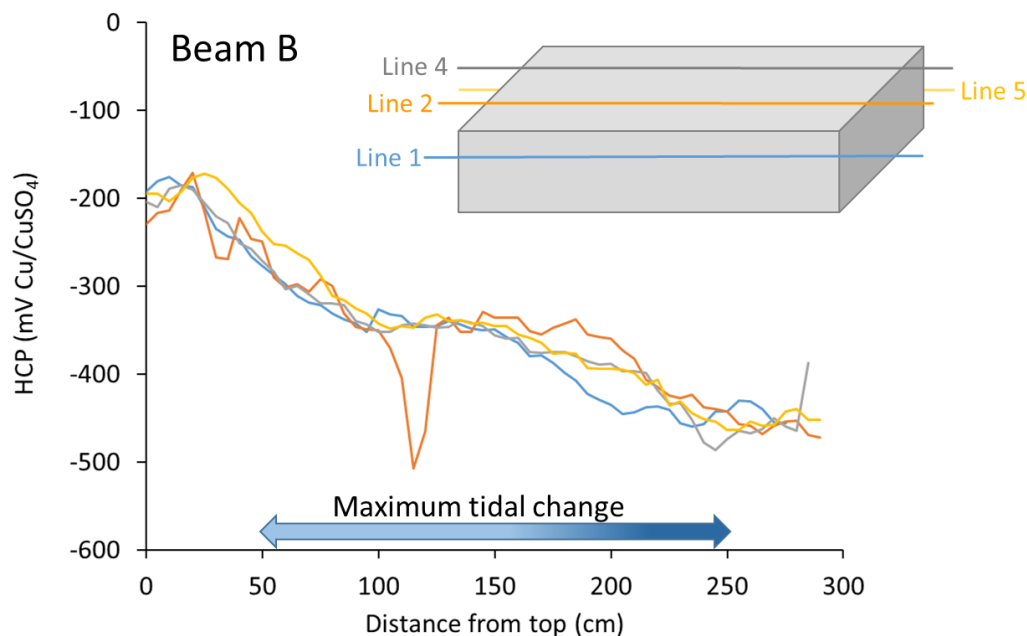


Figure 23: Half-cell potential (HCP) on the sides (Line 1 and Line 5) and top surface (Line 2 and Line 4) of Beam B. Measurements were performed with a wheel electrode above the reinforcement

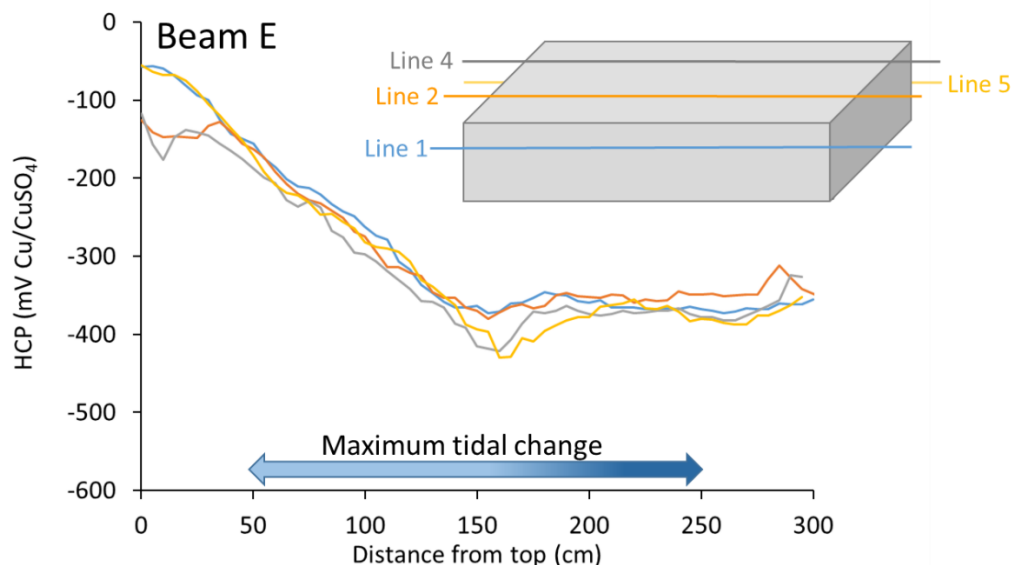


Figure 24: Half-cell potential (HCP) on the sides (Line 1 and Line 5) and top surface (Line 2 and Line 4) of Beam E. Measurements were performed with a wheel electrode above the reinforcement

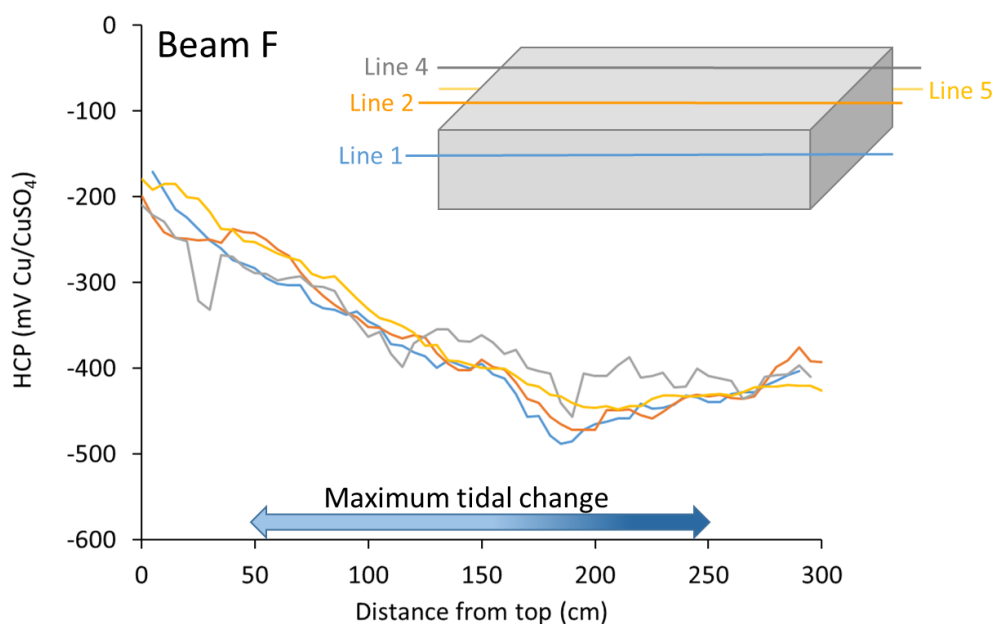


Figure 25: Half-cell potential (HCP) on the sides (Line 1 and Line 5) and top surface (Line 2 and Line 4) of Beam F. Measurements were performed with a wheel electrode above the reinforcement

After 12 days storage at $5 \pm 1^\circ\text{C}$, measurements were repeated with the wheel electrode on the top surface (Line 2 and Line 4) of all concrete beams (see Appendix 4). The measurements were performed at room temperature (20°C) 2 h after taking the beams out of the 5°C room. For Beam B, the observed trends were similar to the first measurements (Figure 23). In Beam E the half-cell potential was decreasing from the atmospheric to the tidal zone, but increasing from the tidal to the submerged zone. In the initial measurements (Figure 24) the half-cell potential was about constant from the tidal to the submerged zone. In Beam F, there was only little variation in the half-cell potential after 12 days storage at $5 \pm 1^\circ\text{C}$. The half-cell potential

was decreasing from -150 to -300 mV from the atmospheric to the tidal zone, with no further change from the tidal to the submerged zone.

6.3 Resistivity

6.3.1 Concrete beams

Resistivity measurements were taken at room temperature (approximately 20°C) in all three exposure zones of Beam B, Beam E and Beam F, two days after removal of the concrete beams from the field station and 1 day after moving them into the laboratory. Twenty measurements were taken with a Wenner probe in each region. The average results of the resistivity measurements are shown in Figure 26. All measured values are given in tabular form in Appendix 5. In all beams, the resistivity was decreasing from the atmospheric via the tidal to the submerged zone. The reason for the decreasing resistivity is probably the higher moisture content in the tidal and submerged zone. The lowest resistivity in all three exposure zones was measured in Beam B. The highest resistivity was measured in Beam E, indicating a refined pore structure and/or a lower pore liquid conductivity due to the pozzolanic reaction of fly ash. Unexpectedly, a similar effect of silica fume on the concrete resistivity was not observed (Beam F vs Beam B).

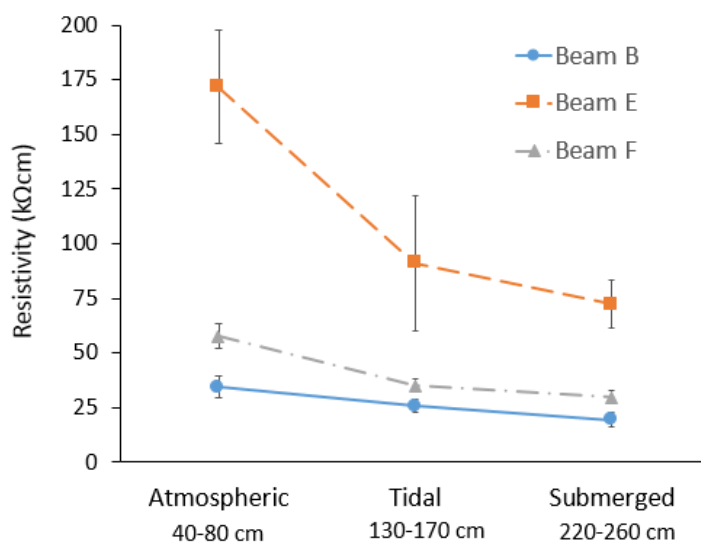


Figure 26: Average resistivity measured at room temperature (20°C) in the three exposure zones of Beam B, Beam E and Beam F. The error bars indicate the standard deviation of twenty measurements

6.3.2 Concrete cores

Concrete resistivity was measured on concrete cores from all three exposure zones taken from Beam B, Beam E and Beam F. At the time of the resistivity measurements, the reference cores without cracks were already cut into two halves. Therefore, resistivity measurements were performed on the available cracked cores (without reinforcement). Measurements were performed at 5°C. Results in tabular form are given in Appendix 5. A summary of the results

is given in Figure 27. Results obtained with lowest phase angle are marked with solid legends. Except for cores BAC and BTC, the lowest phase angle was measured at 100 Hz. For Core BAC and BTC the lowest phase angle was measured with 10 kHz.

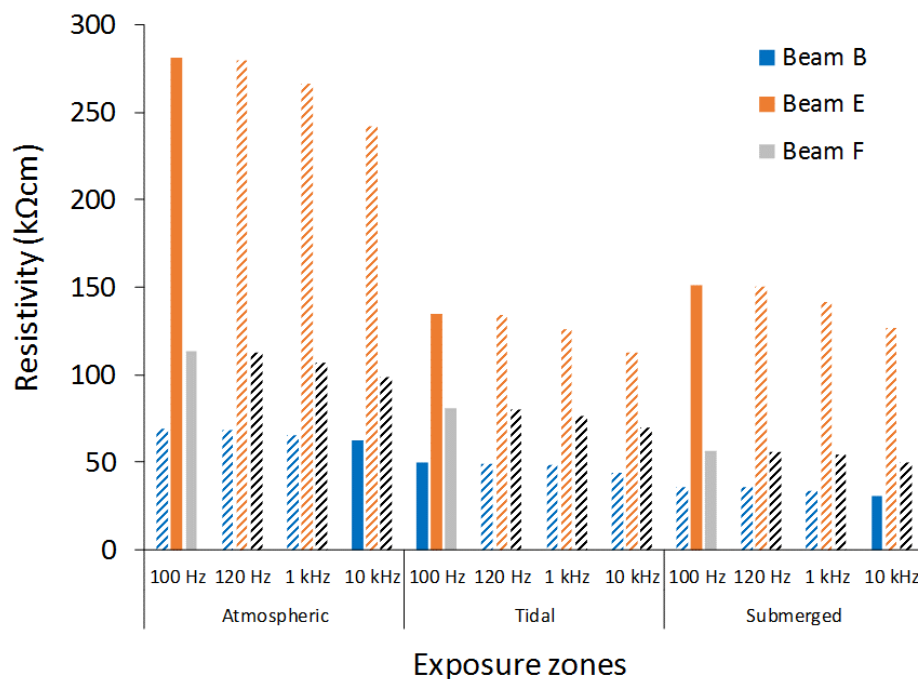


Figure 27: Resistivity measurements performed at 5°C on concrete cores BAC, EAC, FAC (atmospheric), BTC, ETC, FTC (tidal) and BSC, ESC, FSC (submerged). Measurements performed by Solveig Myklebust and Ragnhild Moastuen (Master thesis, 2018). The results obtained with lowest phase angle are solid

6.4 Carbonation depth

After opening the concrete beams to investigate the extent of corrosion (see Chapters 5.11 and 6.6), the freshly split concrete surfaces including the steel-concrete interface were sprayed with pH indicator to identify potential carbonation and/or leaching. Additionally, the outer cylindrical surfaces of selected concrete cores from all exposure zones were sprayed with pH indicator

Figure 28 shows a representative cut and split part from the tidal zone of concrete Beam E. It can be seen that the freshly split concrete surface and steel-concrete interface was neither carbonated nor leached, even close to the crack. However, when opening the crack a white precipitate was found on the crack surfaces (Figure 29) and at the steel-concrete interface (Figure 28) near cracks. Figure 29 shows a representative sample split along a crack. The crack width was 0.15 mm. Spraying the crack surfaces with pH indicator showed reduced pH on the outer 10-20 mm of the crack surface; but not in the full area where white precipitate was observed (Figure 29). An example of a crack with white precipitate before spraying with pH indicator is given in Figure 44.

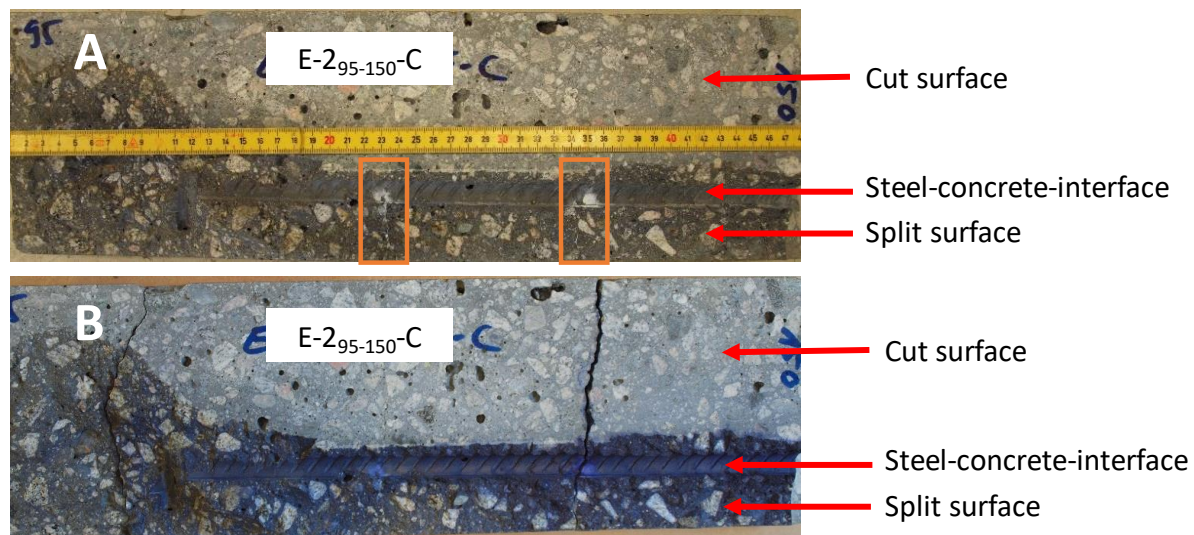


Figure 28: A: Beam E, position 95-150 cm along Line 2 shortly after cutting cover (light colour) and shortly after splitting the remaining part of the concrete (dark colour). Note the white precipitate at the steel-concrete interface and in the cracks (orange rectangles) B: same sample sprayed with thymolphthalein. The large crack in Figure B developed after cutting and splitting the concrete beam. Note: Top face down.

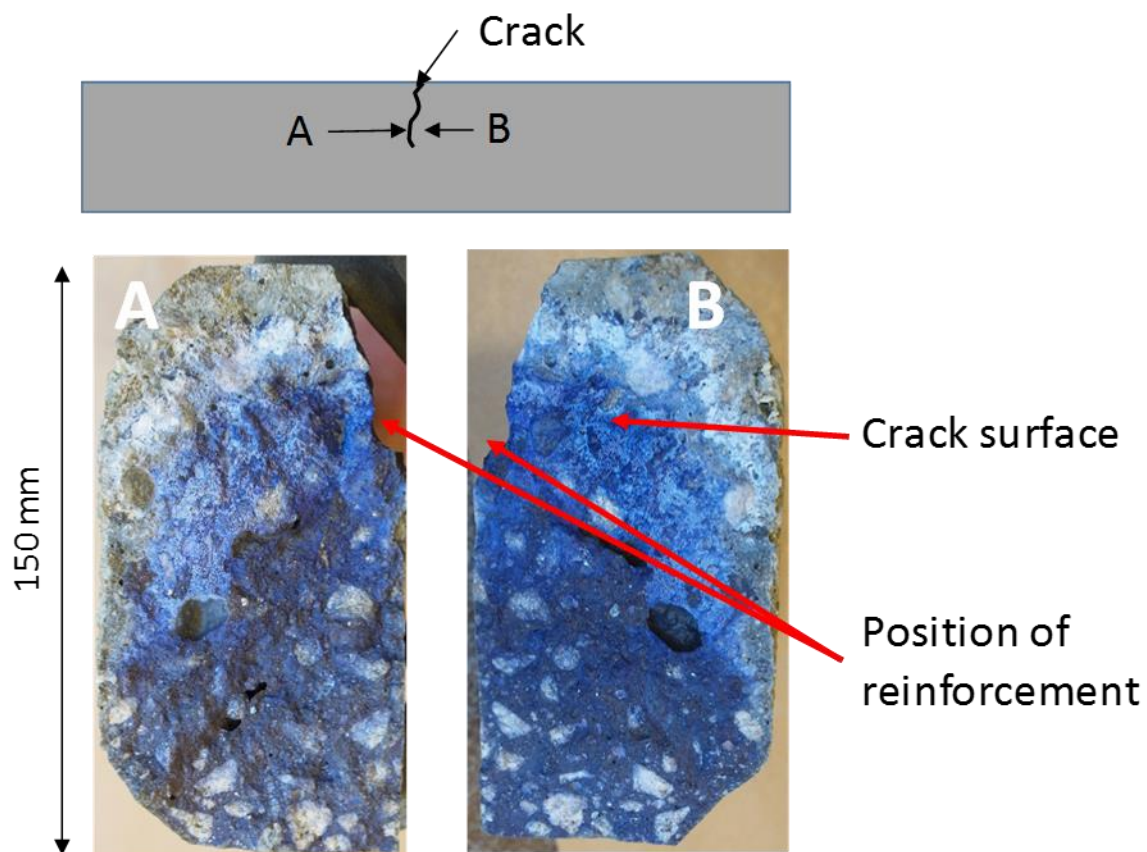


Figure 29: Sample split open at crack and crack surfaces sprayed with thymolphthalein (Beam E, position 180 cm, Line 2 (crack width 0.15 mm)). The white colour on the surface was present before spraying. A and B represent the two surfaces of the same crack. Note: Top face up

6.5 Moisture and porosity

The raw data of moisture measurements is given in Appendix 6.

Figure 31 shows the relative humidity (RH) of concrete cores from Beam B, Beam E and Beam F. The degree of capillary saturation (DCS), suction and macro porosity of cores taken from the different exposure zones of Beam B, Beam E and Beam F when saturated for 21 days and drying at 105°C is given in Figure 31, Figure 33 and Figure 34. In Figure 32, DCS results are plotted versus results of RH. Results are based on initial submersion in water for 21 days. A comparison of data obtained with initial submersion in water for 7 days and 21 days as well as results obtained with the standard NPRA method is given in Appendix 6. A comparison between saturating for 21 days and drying at 105°C and at 50°C is also shown in the appendix.

With some exceptions (e.g. RH for Beam B) there seemed to be little variation between the different layers of each concrete core (i.e. 0-50 mm, 50-100 mm and 100-150 mm). The values for DCS increased from the atmospheric via the tidal to the submerged zone in Beam B and Beam F. Beam E had similar DCS in the tidal and the submerged zone. In the submerged zone, cores from Beam E had the lowest DCS. Beam B and Beam F had high DCS in the submerged zone.

There was a trend of increasing RH from the atmospheric to the submerged zone in all concrete cores.

The macro porosity showed a trend of Beam B > Beam E > Beam F. The suction porosity, on the other hand, followed the opposite trend giving Beam F > Beam E > Beam B. Beam B had the highest macro porosity and the lowest suction porosity of all three Beams. Beam F had the lowest macro porosity, but highest suction porosity.

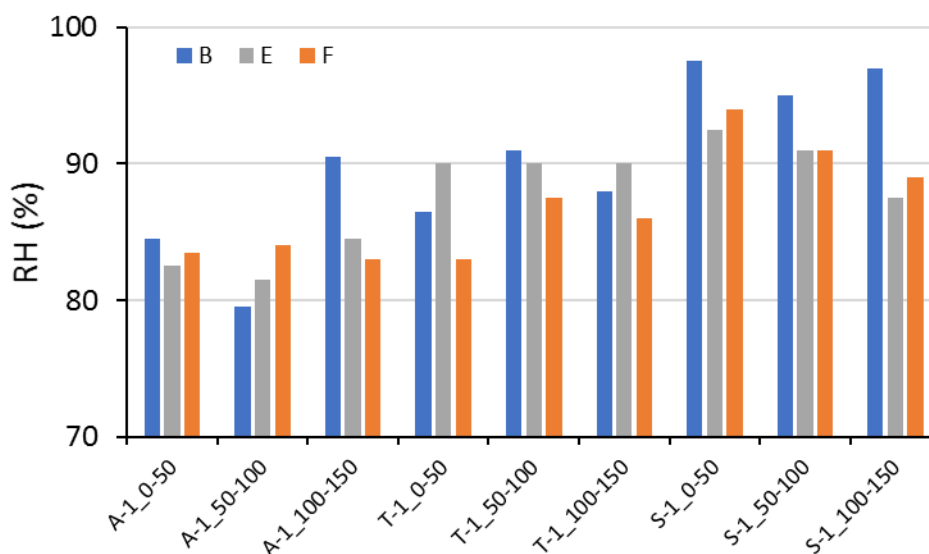


Figure 30: Relative humidity (RH) of concrete cores taken from beams B, E and F (A: Atmospheric, T: Tidal, S: Submerged)

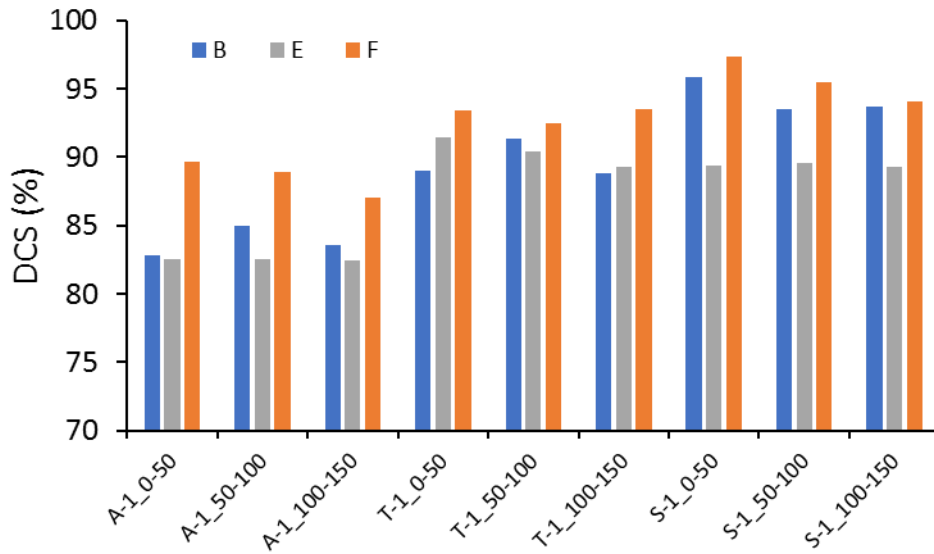


Figure 31: Degree of capillary suction (DCS) of concrete cores taken from Beam B, E and F (A: Atmospheric, T: Tidal, S: Submerged). Results based on 21 days submersion in water and 7 days drying at 105°C

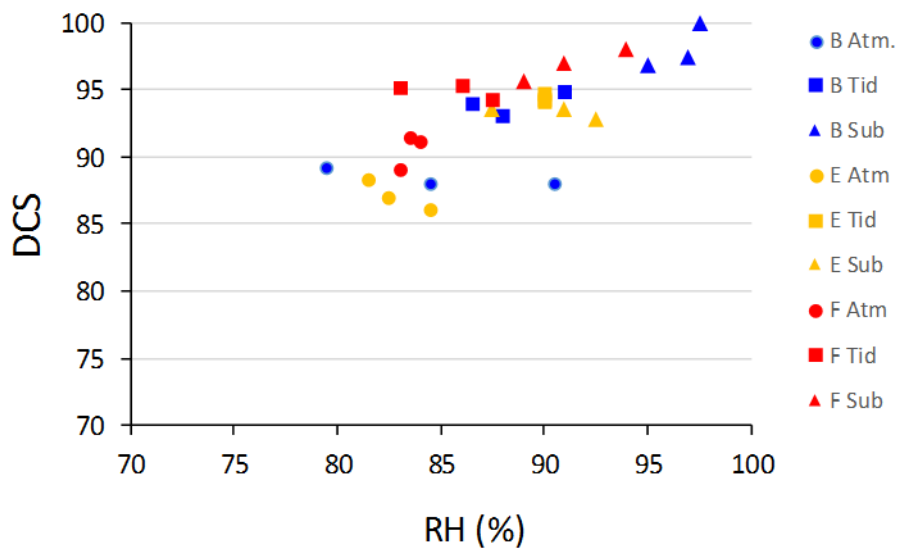


Figure 32: Degree of capillary suction (DCS) versus relative humidity (RH) of concrete cores taken from beams B, E and F taking in all three exposure zones (Atm: Atmospheric, Tid: Tidal, Sub: Submerged). DCS based on 21 days submersion in water and 7 days drying at 105°C

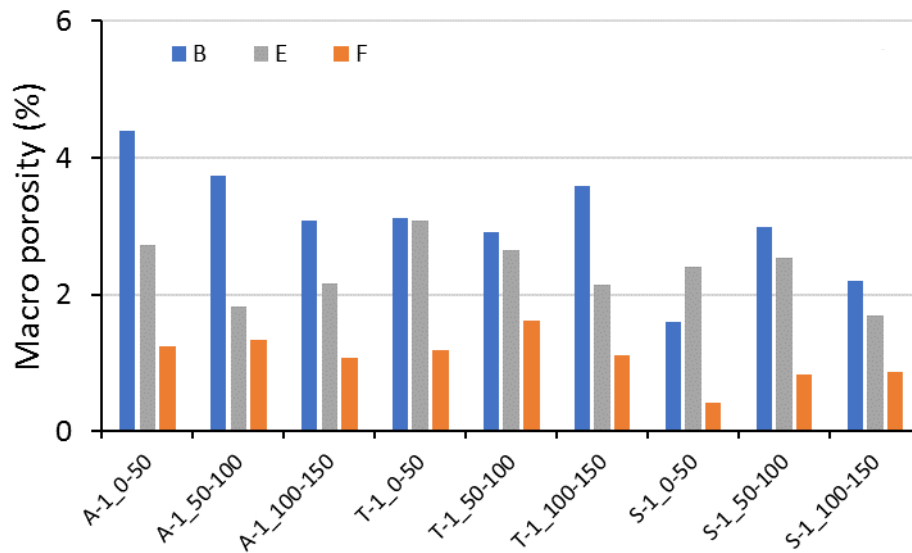


Figure 33: Macro porosity of concrete cores taken from beams B, E and F (A: Atmospheric, T: Tidal, S: Submerged). Results based on 21 days submersion in water, 7 days drying at 105°C and 2 days pressure saturation

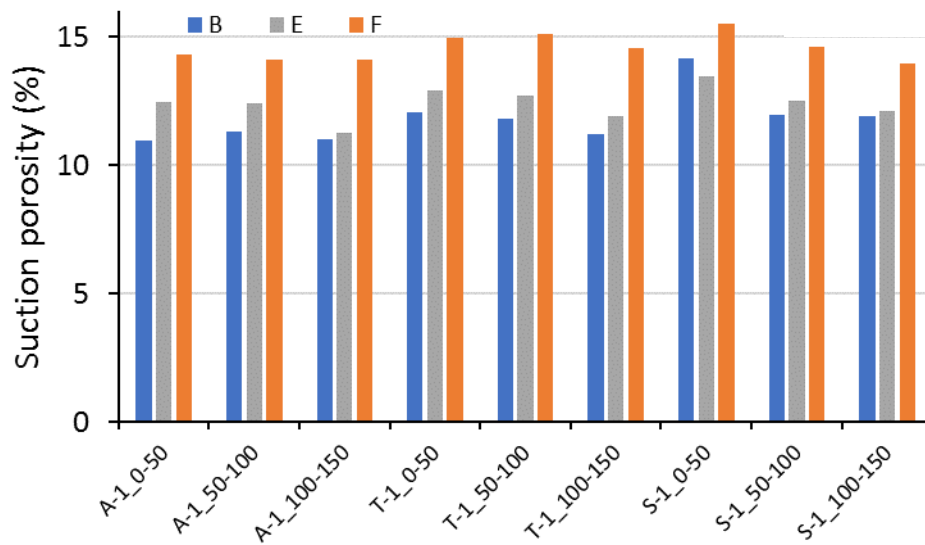


Figure 34: Suction porosity of concrete cores taken from beams B, E and F (A: Atmospheric, T: Tidal, S: Submerged). Results based on 21 days submersion in water and 7 days drying at 105°C

6.6 Chloride ingress

6.6.1 Chloride profiles

Figure 35, Figure 36 and Figure 37 show the chloride profiles of concrete cores taken without cracks from Beams B, E from the atmospheric (BAR, EAR, FAR), tidal (BTR, ETR, FTR) and submerged (BSR, ESR, FSR) zone. The raw data is given in Appendix 7. In all three concrete beams, the highest chloride ingress was measured in the submerged zone. However, for Beam E, little difference was observed between the three zones. In total, there was less chloride ingress measured in Beam E.

Large variations are observed in critical chloride content [24]; 0.07 % Cl⁻ by weight of concrete has been suggested for Norwegian structures [25].

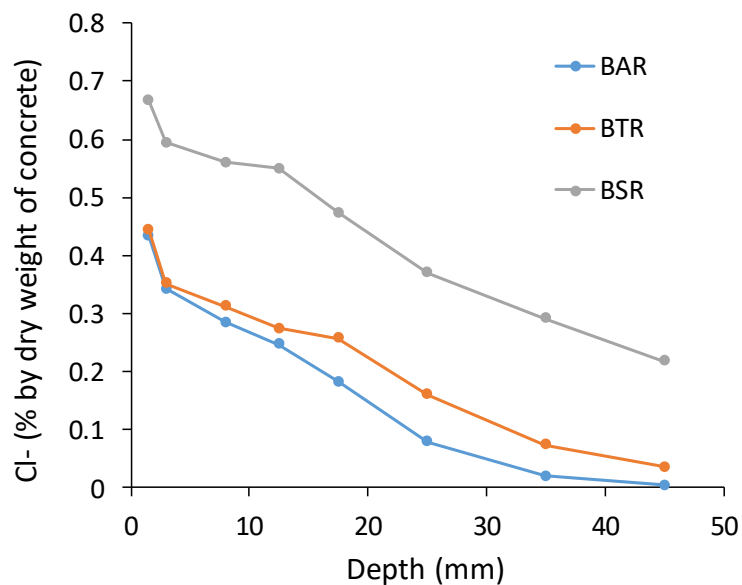


Figure 35: Chloride profiles of cores from Beam B determined by potentiometric titration; BAR (atmospheric), BTR (tidal) and BSR (submerged)

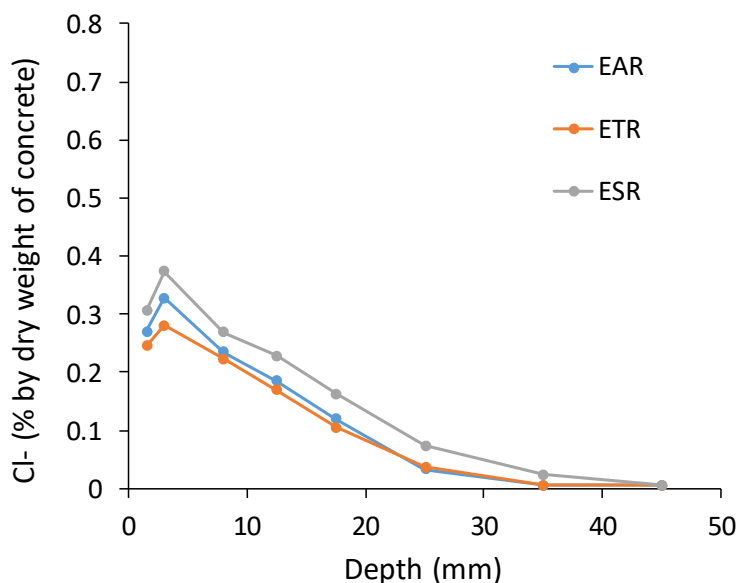


Figure 36: Chloride profiles of cores from Beam E determined by potentiometric titration; EAR (atmospheric), ETR (tidal) and ESR (submerged)

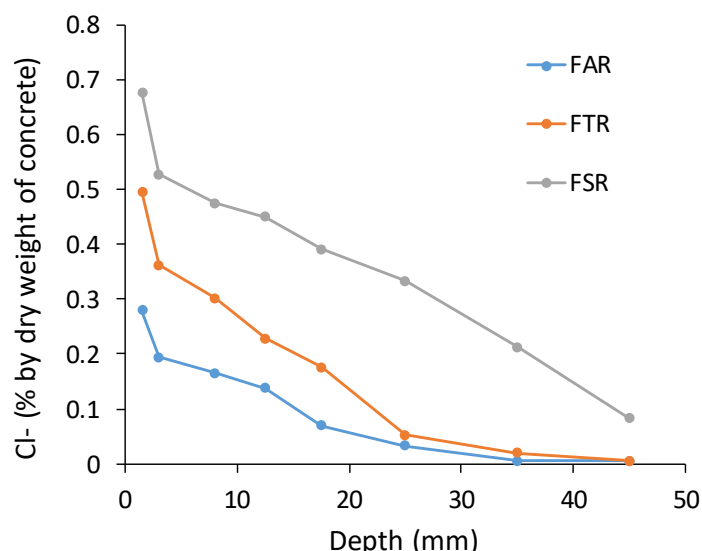


Figure 37: Chloride profiles of cores from Beam F determined by potentiometric titration; FAR (atmospheric), FTR (tidal) and FSR (submerged)

6.6.2 μ -XRF chloride maps

6.6.2.1 Unreinforced cracked and uncracked concrete cores

In Figure 38, Figure 39 and Figure 40 the chloride maps measured with μ -XRF on reference cores and cores with cracks from Beam B, Beam E and Beam F are shown. The chloride maps show gradients of intensities from the surfaces to the centre. Note that each picture is normalized to the highest intensity within the picture. Thus, different pictures should not be directly compared regarding intensities of chloride. Concrete cores were drilled through the whole beam. Therefore, chloride ingress is visible from both sides of the concrete cores. All concrete beams were mounted as pairs on the ferry quay in Sandnessjøen. The left side

represents the cracked “top side” of the beams. The right side represents the “bottom side” of the beams, oriented towards the other concrete beams of each pair (Figure 7).

No systematic difference in chloride ingress from top and bottom sides was observed.

For all concrete beams, it can be seen that the chloride ingress depth is increasing from the atmospheric to the submerged zone.

In some cases, a deeper ingress of chlorides is observed along cracks when compared to the chloride ingress of the reference cores without cracks. Especially, the cores from the tidal zone (BTC, ETC, FTC) with the largest cracks show an impact of the cracks on chloride ingress

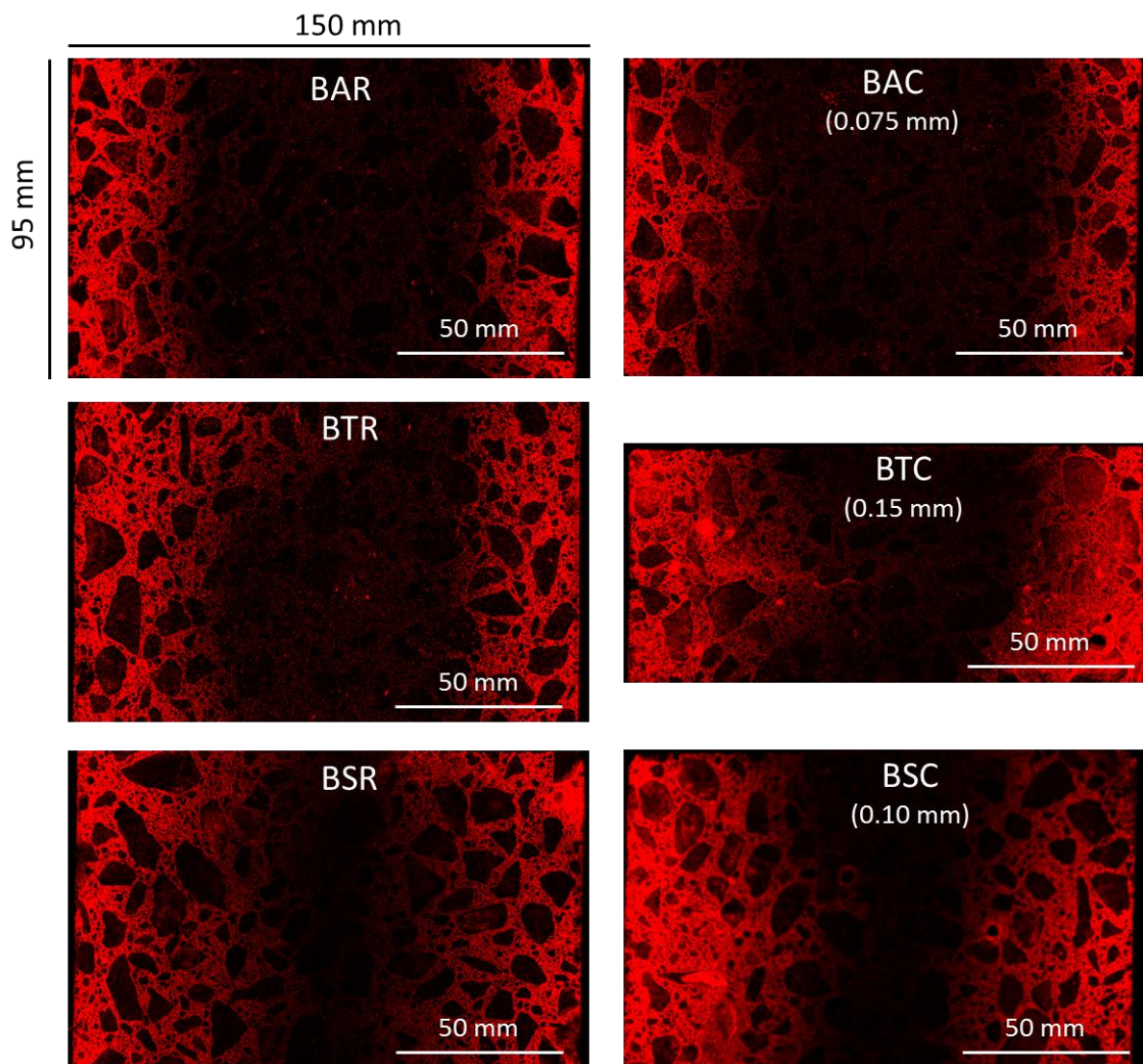


Figure 38: μ -XRF chloride maps of reference cores (BAR, BTR, BSR) and cores with cracks (BAC, BTC, BSC) from the three exposure zones of Beam B. Surface crack width indicated in brackets. Each picture is normalized to the highest measured intensity within the picture. The mapping area was slightly larger than the whole width of the core causing black stripes on the left and right side in some maps

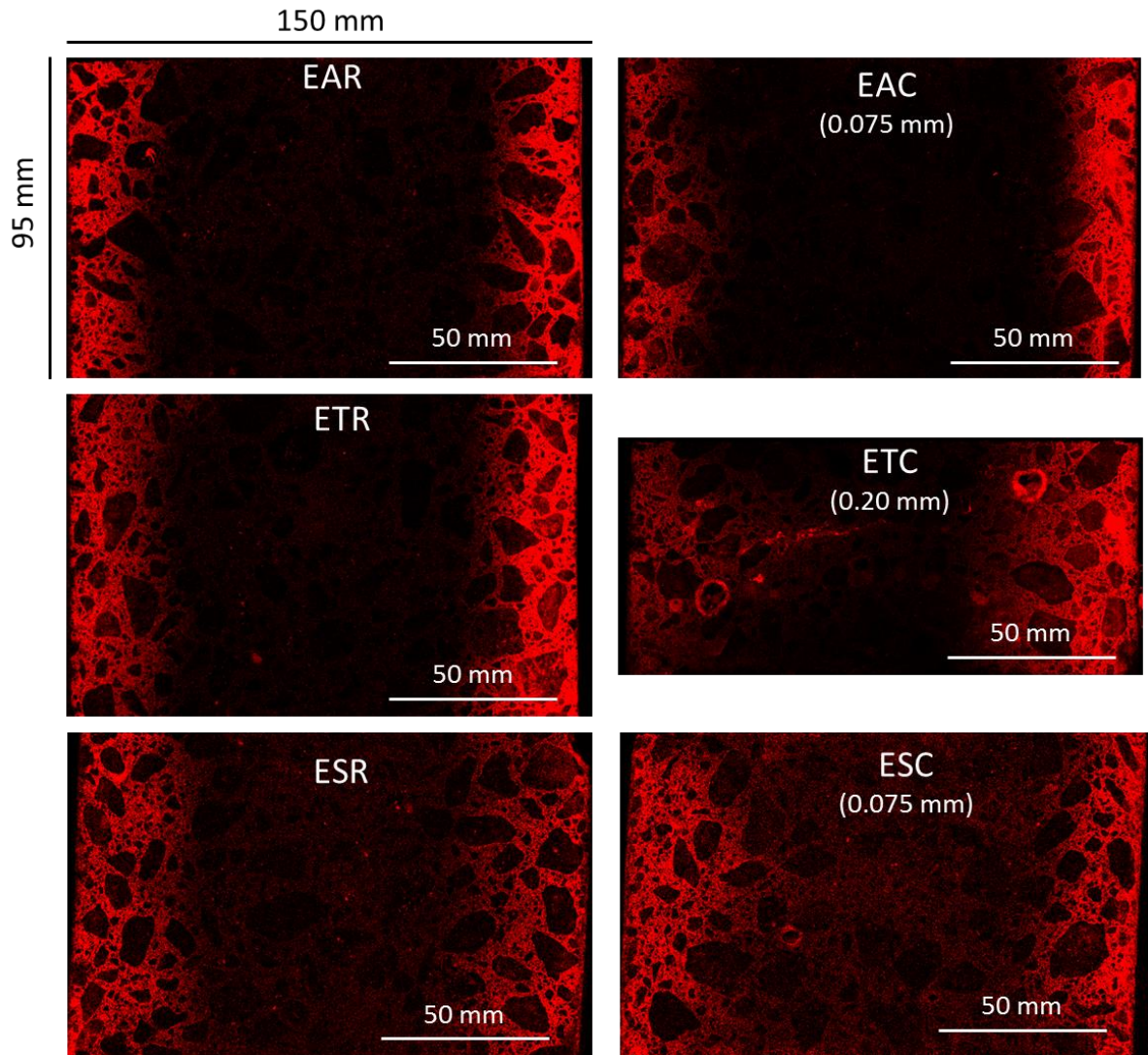


Figure 39: μ -XRF chloride maps of reference cores (EAR, ETR, ESR) and cores with cracks (EAC, ETC, ESC) from the three exposure zones of Beam E. Surface crack width indicated in brackets. Each picture is normalized to the highest measured intensity within the picture. The mapping area was slightly larger than the whole width of the core causing black stripes on the left and right side in some maps

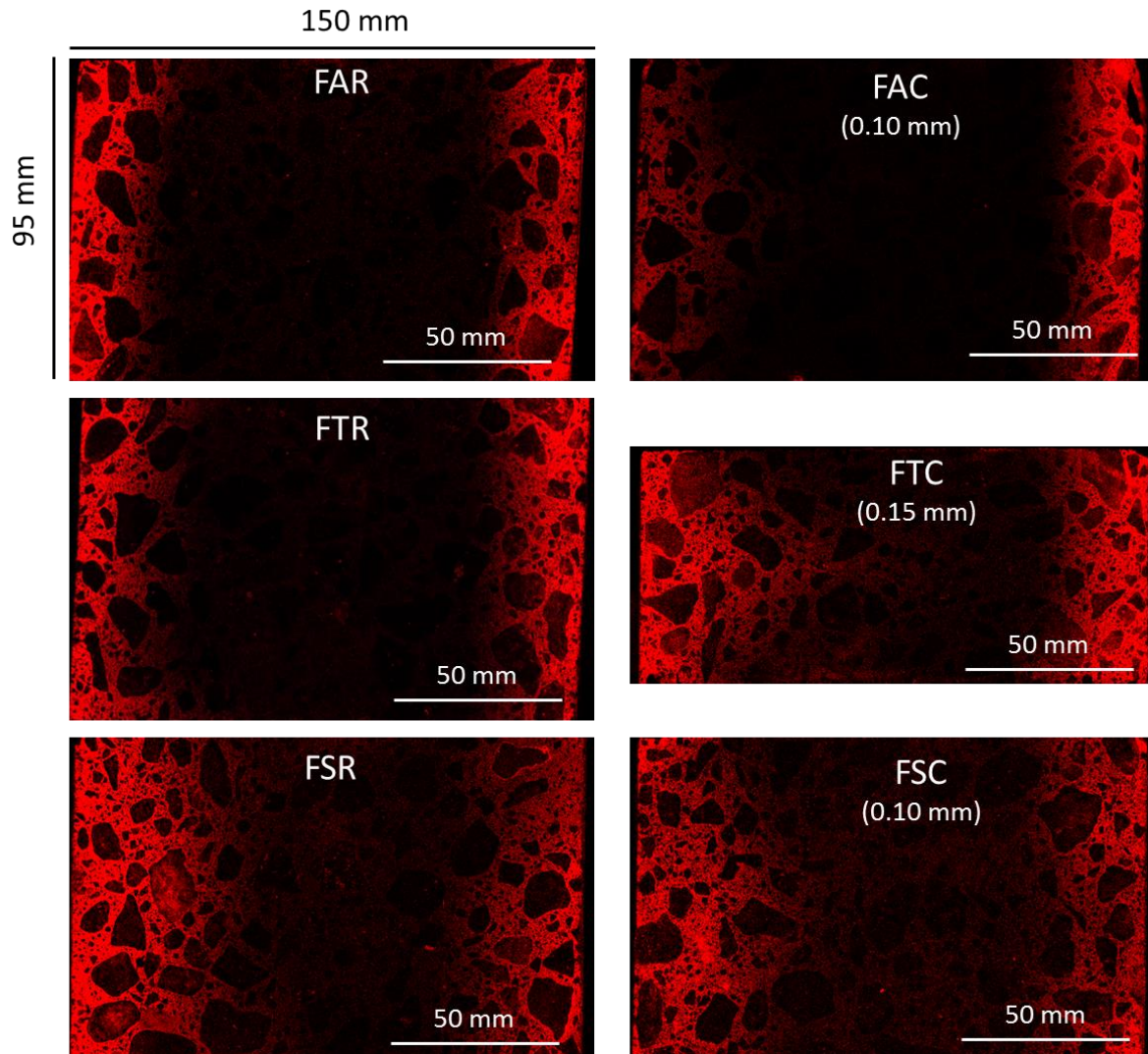


Figure 40: μ -XRF chloride maps of reference cores (FAR, FTR, FSR) and cores with cracks (FAC, FTC, FSC) from the three exposure zones of Beam F. Surface crack width indicated in brackets. Each picture is normalized to the highest measured intensity within the picture. The mapping area was slightly larger than the whole width of the core causing black stripes on the left and right side in some maps

6.6.2.2 Spacers

An illustration of a concrete slice taken from the cross section of concrete beams is given in Figure 41. Cut A and B represents two slices, A: 2-3 cm from the spacer and B: through the centre of the spacer.

Figure 42 shows the chloride ingress at a spacer of Beam B in the tidal zone. Chloride intensities are here shown in different colours to better illustrate variations in the intensities and visualize the ingress depth. Red colours show the highest intensities measured, while dark blue colours represent the lowest intensities measured. All intensities are normalized to the highest intensity within the same picture and should not be directly compared to other pictures.

In the reference slice (Figure 42 A), cut 2 cm outside the spacer relatively even chloride ingress depth was observed from all three exposed sides, except the bottom left corner. In the slice cut through the middle of the spacer deeper chloride ingress was observed from the top where the spacer was located. However, highest chloride ingress was observed in the lower left corner of the concrete slice and to a deeper depth than in the reference slice, which limits conclusions on the impact of the spacer on ingress. A possible cause of the damage in the lower corner might be freeze/thaw damage. This damage type was only observed in the tidal zone.

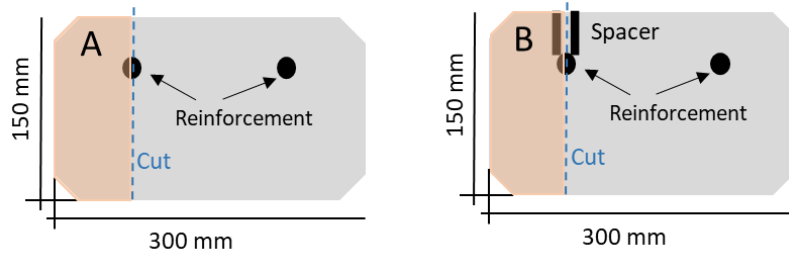


Figure 41: Illustration of the origin of the concrete slices with spacers cut from the concrete beams

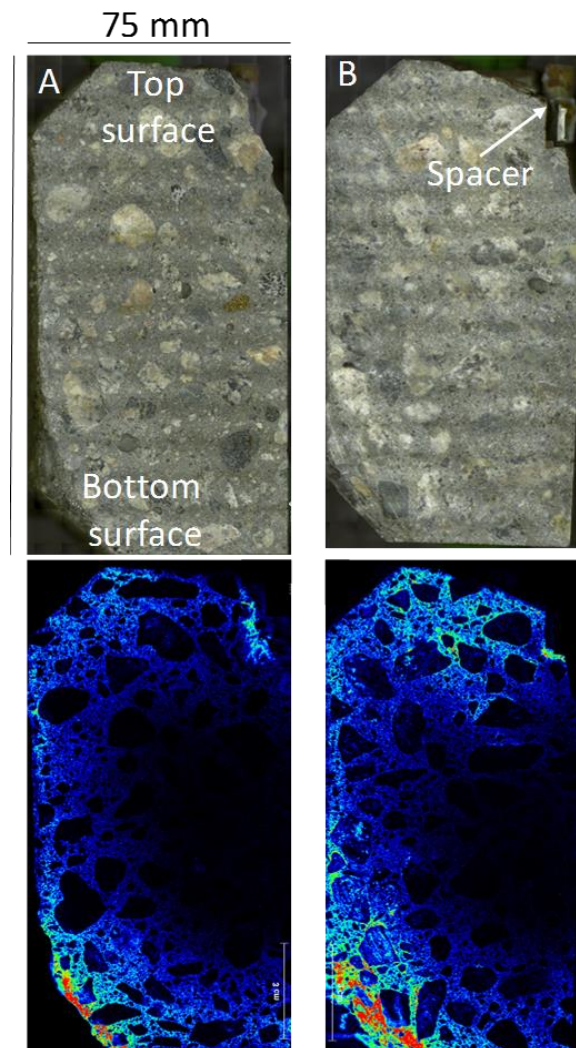


Figure 42: Chloride ingress in concrete Beam B at a spacer in the tidal zone (location 110 mm, Line 4). A: reference slice 2 cm from the spacer, B: slice cut through the centre of the spacer

In the submerged zone outside the spacer, similar ingress of chlorides was observed from the top and bottom sides. For unknown reasons, less ingress was seen from the side (Figure 43A). In the slice cut through the spacer, deeper ingress was observed from the top surface where the spacer was located, but also at the bottom surface (Figure 43B). Again, this limits conclusions on the impact of the spacer on ingress.

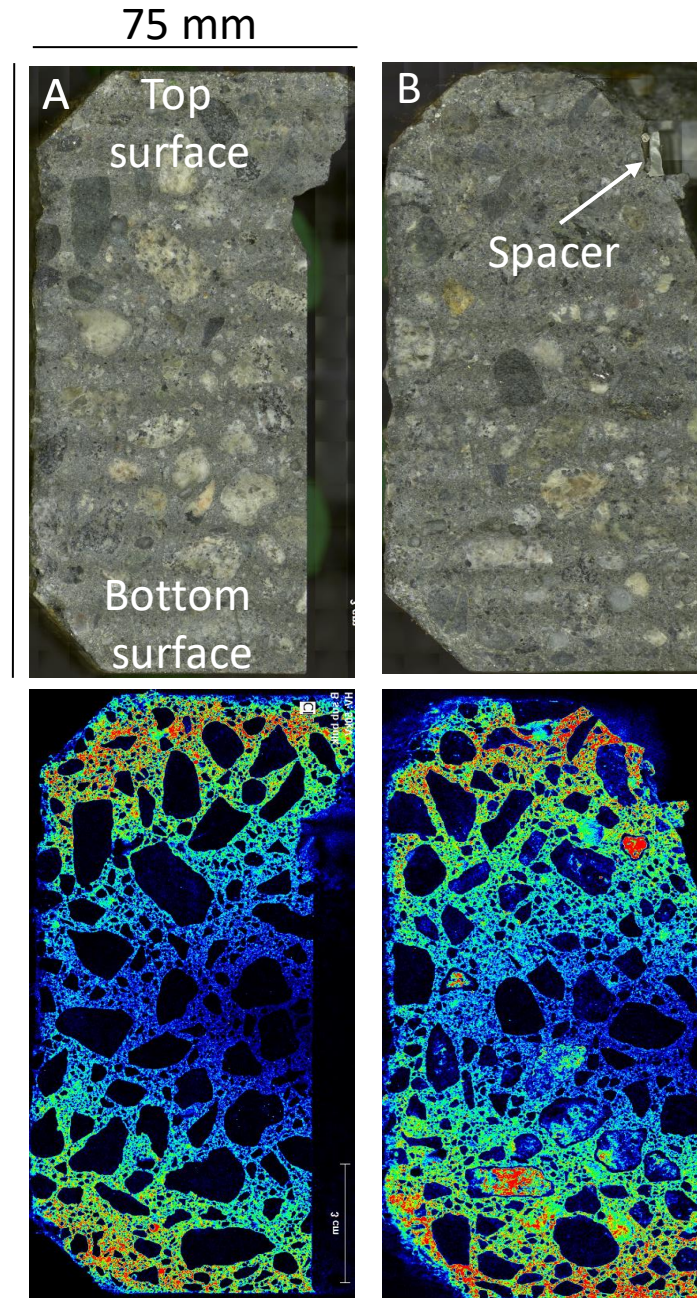


Figure 43: Chloride ingress in concrete Beam B at a spacer in the submerged zone (location 270 mm, Line 4). A: reference slice 3 cm from the spacer, B: slice cut through the middle of the spacer

6.7 Precipitation on crack surfaces and along reinforcement

When opening the concrete beams, white precipitate was found on crack surfaces, at the steel-concrete-interface and on the surface of the reinforcement near cracks (Figure 44). The dark coloured part of the concrete is the newly split surfaces. The white colouration was found systematically in all exposure zones. μ -XRF analysis of the white precipitate on the surface of the reinforcement showed that S, Cl, Ca, Si and small amounts of Al were present (Figure 45). In addition, Fe was detected due to the underlying steel. A white precipitate on crack surfaces was also found in earlier investigations by the present authors (Hafsrjord Bridge) and observations are also mentioned in the literature, e.g. [26].

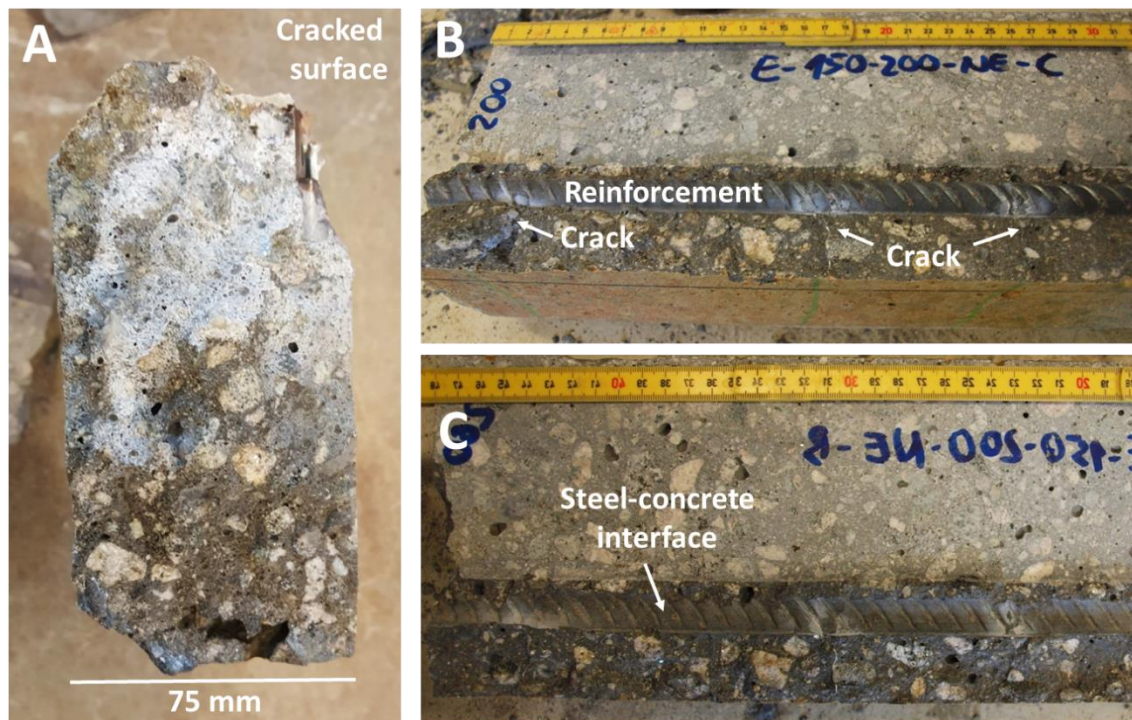


Figure 44: A: White precipitate on crack surface from Beam B, crack located at 100 cm (sample split along the crack); B and C: Beam E, white precipitate on the reinforcement and at the steel-concrete interface (after removing reinforcement) near cracks, section 150-200 cm

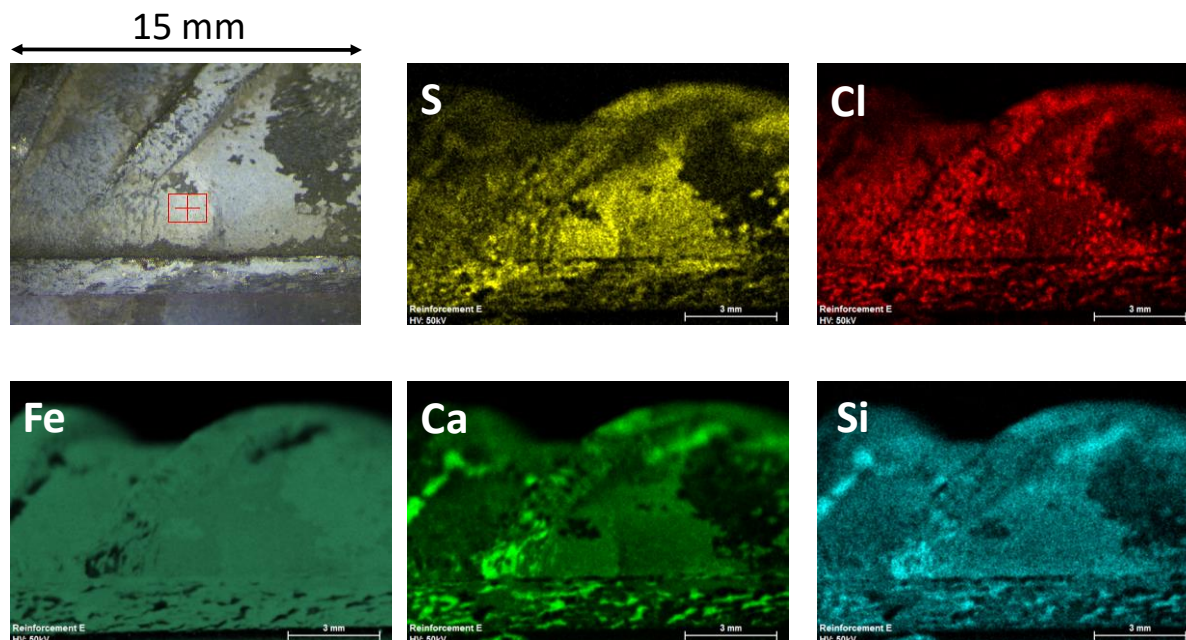


Figure 45: μ -XRF map of white precipitate found on the surface of the reinforcement near a crack of Beam E at around 180 cm. Red square in the upper left picture indicates the focus point of the X-ray beam

From each beam, two concrete cores were drilled through the reinforcement in the tidal zone. The cores were split in line with the reinforcement to study the ingress of ions from the seawater. Figure 46 shows an elemental mapping (S, Cl, Mg, Ca, Fe, Si, Al and K) of core ETCr2. The figure indicates that chloride and sulphate from seawater penetrated through the crack and along the reinforcement in the debonding zone. Bending cracks perpendicular to the reinforcement can lead to slip and separation between the concrete cover and the reinforcement in a certain distance from the crack. This effect is nicely documented in [27], where ingress of chlorides along the reinforcement was observed. As seen above the white precipitate at the steel-concrete-interface appears to be rich in sulphate. The elemental mapping of cores BTCr2, BTCr4, ETCr4, FTCr2 and FTCr4 is shown in Appendix 8. Calcium is present in high amounts in the whole concrete and might also be present in the white precipitate. Silicon and aluminium intensities originate mainly from the aggregates. Aluminium does not appear within the white precipitate in the μ -XRF map. Still, SEM-EDS point analysis indicate ettringite as main constituent of the white precipitate [28]. Low intensities of silicon and aluminium in the steel-concrete interface can be due to a "shadowing effect". The surface of steel-concrete interface is in larger distance to the detector than the rest of the concrete samples, i.e. less signal is reaching the detector. And intensities are overshadowed by the signal coming from the residual concrete. As no iron was detected it is unlikely that the white precipitate is a corrosion product.

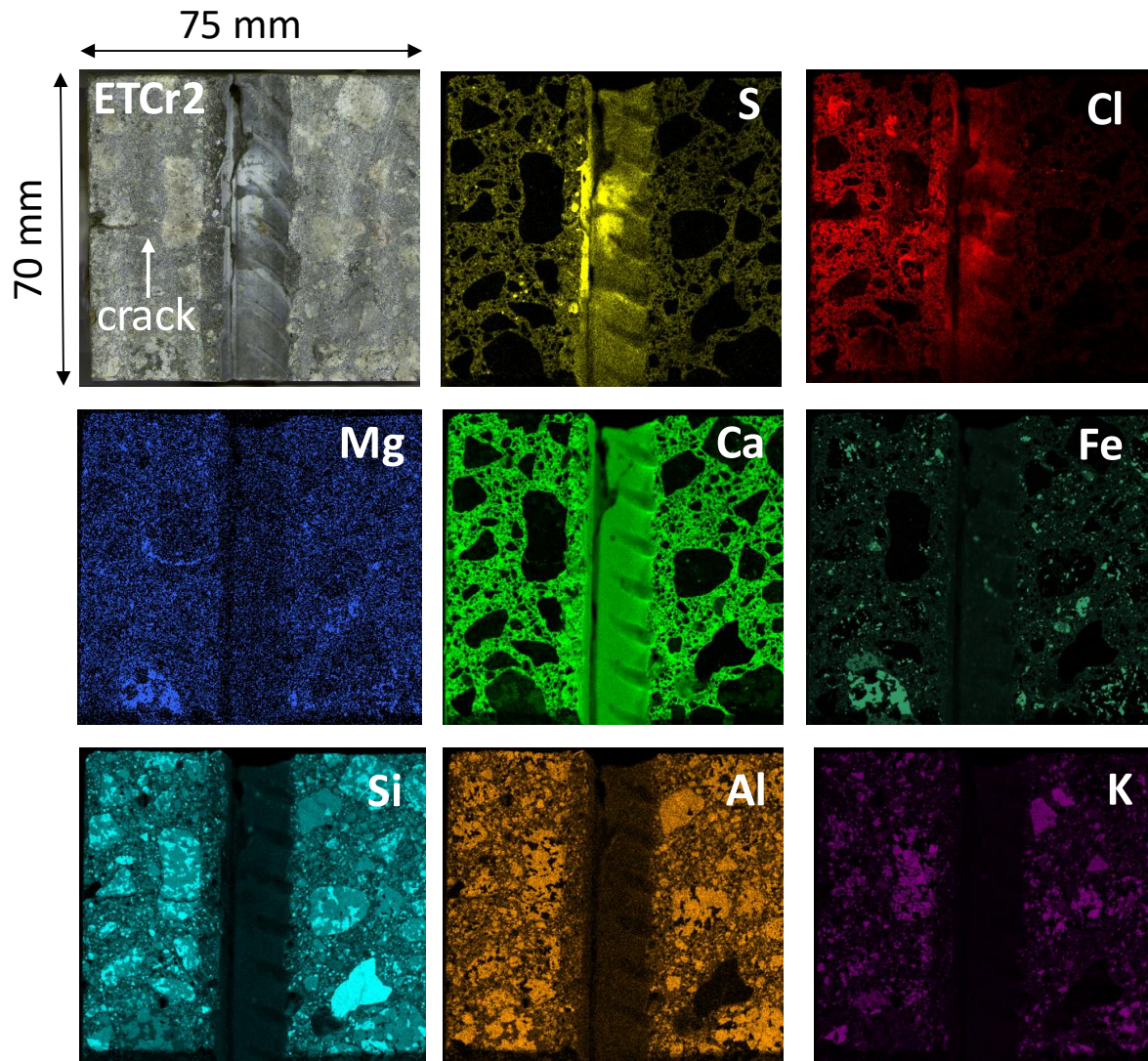


Figure 46: Overview picture of the mapped area of core ETCr2 containing both a crack and reinforcement, and elemental mapping of S, Cl, Mg, Ca, Fe, Si, Al and K

6.8 Self-healing of cracks

6.8.1 Degree of self-healing

Concrete cores taken with cracks from Beam B, Beam E and Beam F were investigated with μ -XRF. The crack width and the degree of self-healing were assessed on the cut surface of the cores used for elemental mapping. The crack width was measured from the surface in steps of 5 mm with the line scan tool of the μ -XRF software. Self-healing of cracks was visually analysed with a 100x magnification camera and categorized in three different degrees of self-healing 1) complete self-healing (■), 2) no self-healing (□), 3) partly self-healing (▲). The results are shown in Table 10, Table 11 and Table 12.

Table 10: Crack width (w) and degree of self-healing (S) of cracks in cores drilled from Beam B

Core	BAC		BTC		BSC		BTCr2		BTCr4	
	w (mm)	S	w (mm)	S	w (mm)	S	w (mm)	S	w (mm)	S
5	n.v.	-	0.33	▲	0.12	▲	0.04	■	0.13	■
10	n.v.	-	0.19	■	0.09	■	0.09	■	n.v.	-
15	n.v.	-	0.11	■	0.04	■	n.v.	-	0.12	▲
20	n.v.	-	0.03	■	0.10	▲	n.v.	-	0.16	▲
25	n.v.	-	n.v.	-	0.03	■	n.v.	-	n.v.	-
30	n.v.	-	n.v.	-	n.v.	-	n.v.	-	n.v.	-
35	n.v.	-	n.v.	-	n.v.	-	n.v.	-	n.v.	-
40	n.v.	-	n.v.	-	n.v.	-	n.v.	-	n.v.	-
45	n.v.	-	n.v.	-	n.v.	-	n.v.	-	n.v.	-
50	n.v.	-	n.v.	-	n.v.	-	n.v.	-	n.v.	-

■ complete self-healing, closed crack; □ no self-healing, open crack; ▲ partly self-healed crack
 n.v.: not visible

Table 11: Crack width (w) and degree of self-healing (S) of cracks in cores drilled from Beam E

Core	EAC		ETC		ESC		ETCr2		ETCr4	
	w (mm)	S	w (mm)	S	w (mm)	S	w (mm)	S	w (mm)	S
5	0.06	■	0.24	■	0.15	■	0.32	□	0.08	■
10	n.v.	-	0.23	■	0.16	▲	0.20	□	0.17	■
15	n.v.	-	0.15	■	0.04	■	0.13	■	0.12	■
20	n.v.	-	n.v.	-	n.v.	-	0.23	▲	0.13	□
25	n.v.	-	0.07	■	0.03	■	0.07	■	0.06	■
30	n.v.	-	n.v.	-	0.12	▲	n.v.	-	n.v.	-
35	n.v.	-	0.09	■	0.07	▲	n.v.	-	n.v.	-
40	n.v.	-	n.v.	-	n.v.	-	n.v.	-	n.v.	-
45	n.v.	-	n.v.	-	n.v.	-	n.v.	-	n.v.	-
50	n.v.	-	0.12	■	n.v.	-	n.v.	-	n.v.	-

■ complete self-healing, closed crack; □ no self-healing, open crack; ▲ partly self-healed crack
 n.v.: not visible

Table 12 Crack width (w) and degree of self-healing (S) of cracks in cores drilled from Beam F

Core	FAC		FTC		FSC		FTCr2		FTCr4	
	w (mm)	S	w (mm)	S	w (mm)	S	w (mm)	S	w (mm)	S
5	0.09	■	0.32	□	0.05	■	0.13	■	0.12	■
10	0.10	▲	0.15	■	0.02	■	0.12	▲	0.12	■
15	0.09	▲	0.21	■	0.06	■	0.04	□	0.08	■
20	0.07	■	0.10	■	0.10	■	n.v.	-	0.03	■
25	n.v.	-	0.13	■	0.07	■	n.v.	-	0.07	▲
30	n.v.	-	n.v.	-	0.02	■	n.v.	-	n.v.	-
35	n.v.	-	0.06	■	n.v.	-	n.v.	-	n.v.	-
40	n.v.	-	n.v.	-	n.v.	-	n.v.	-	n.v.	-
45	n.v.	-	n.v.	-	n.v.	-	n.v.	-	n.v.	-
50	n.v.	-	0.03	■	n.v.	-	n.v.	-	n.v.	-

■ complete self-healing, closed crack; □ no self-healing, open crack; ▲ partly self-healed crack
 n.v.: not visible

The largest crack width observed to be completely self-healed was 0.24 mm and in the tidal zone (ETC). In some cases, the outer 5 mm of the cracks are only partly self-healed or completely open. Particles were observed in these cases, indicating that the concrete and potentially the self-healing of the crack was disturbed by the drilling and cutting of the cores.

In Beam F, it was possible to compare the extent of self-healing in all three exposure zones. In the tidal zone, cracks up to 0.21 mm appeared completely healed. In the atmospheric zone, cracks of 0.10 mm crack width appeared only partly healed. Cracks with the same crack width appeared completely healed in the submerged zone. This indicates that there is a potentially higher ability of cracks to self-heal in the tidal and submerged zone. In Beams B and E, insufficient data could be obtained from the atmospheric zone due to too small crack width (<0.03 mm). It should be mentioned that the accuracy of the visual assessment is in this range.

To visualize the degree of self-healing, overview pictures of the cracks were taken with a 10x magnification camera of the μ -XRF. Additionally, where possible, pictures were taken with a 100x magnification camera at selected crack depth. Pictures of the cracks of the concrete cores BTC, ETC and FTC are given in Figure 47, Figure 48 and Figure 49. The pictures show extensive self-healing of the cracks with a white precipitate. Pictures of the cracks from the other cores are given in Appendix 9.

Due to the similar crack width in the tidal zone of the three beams, core BTC, ETC and FTC are suitable to study the impact of binder on the extent of corrosion. In all three beams, the cracks in the tidal zone appeared completely self-healed. The present results do not show any difference in the self-healing ability of the three investigated binders.

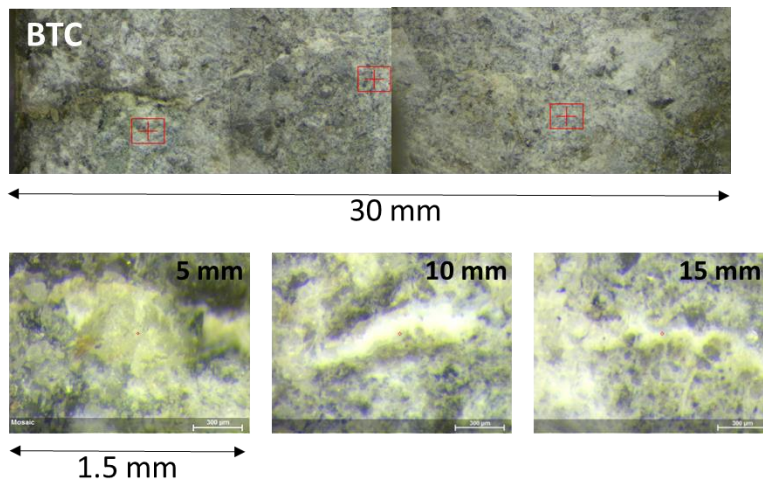


Figure 47: Crack in core BTC. Overview of crack (upper part; 10x magnification) and crack pictures at selected crack depths (lower part; 100x magnification). (The red squares indicate the potential position of the X-ray beam in case of point analysis and is not relevant here)

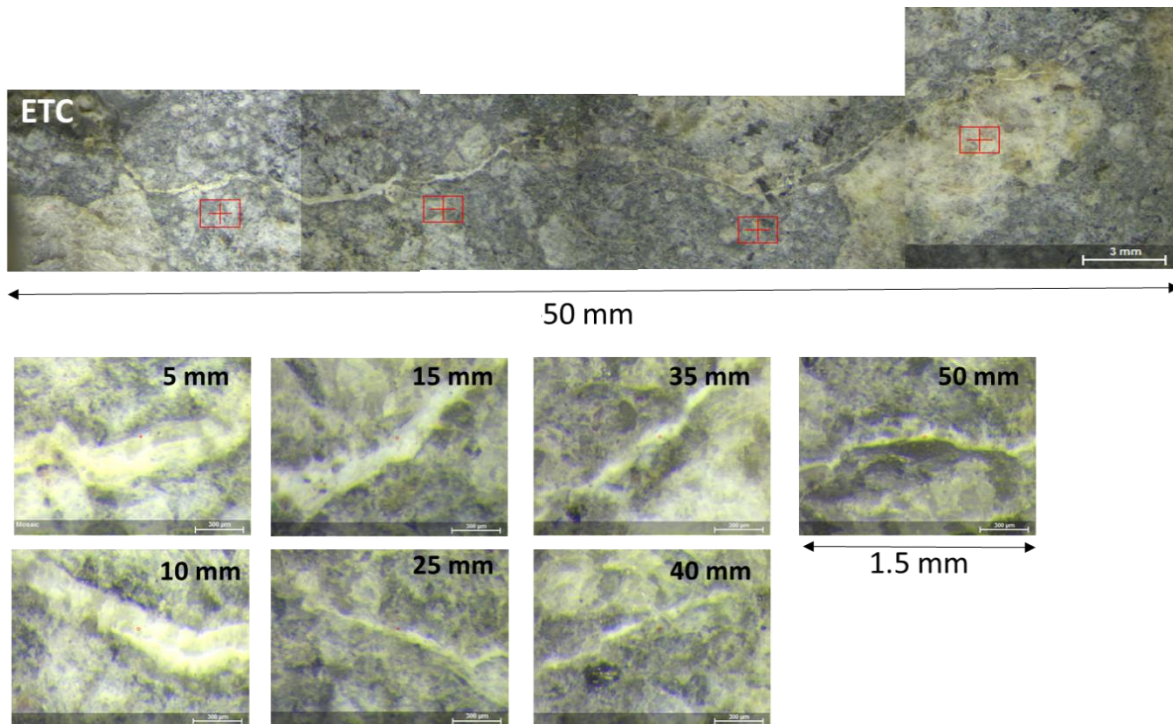


Figure 48: Crack in core ETC. Overview of crack (upper part; 10x magnification) and crack pictures at selected crack depths (lower part; 100x magnification). (The red squares indicate the potential position of the X-ray beam in case of point analysis and is not relevant here)

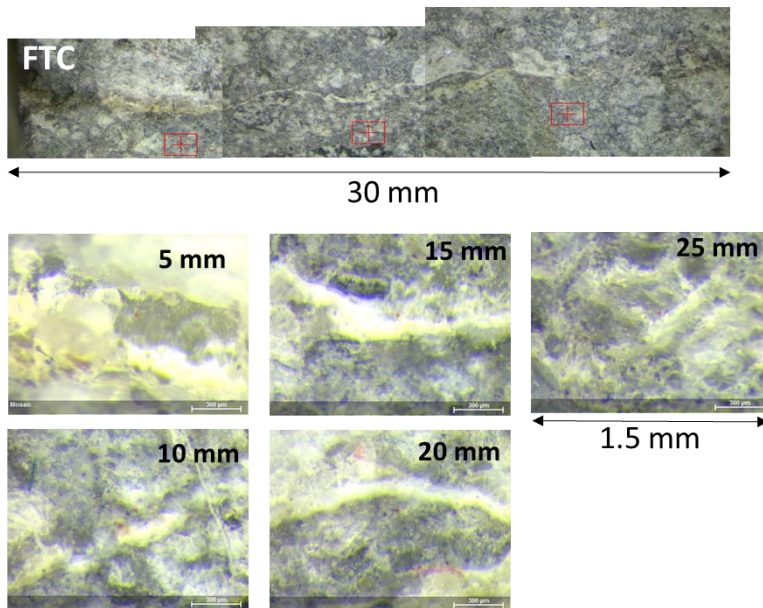


Figure 49: Crack in core FTC. Overview of crack (upper part; 10x magnification) and crack pictures at selected crack depths (lower part; 100x magnification). (The red squares indicate the potential position of the X-ray beam in case of point analysis and is not relevant here)

6.8.2. Composition of self-healing products

Table 13, Table 14 and Table 15 show the average composition of self-healing products measured using μ -XRF. There are challenges in the interpretation of the measured composition. First of all, focusing the X-ray beam on rough surfaces is difficult. In addition, some of the measured cracks were very narrow. Thus, besides the self-healing product in the crack, parts of the surrounding concrete may have been analysed. Secondly, μ -XRF does not detect elements lighter than Na. Hence, H, O and C are not detected. Hence, the interpretation of the composition e.g. presence of hydrates, carbonates or non-hydrated phases, is difficult. Finally, with the resolution (100x magnification, spot size of 20 μ m and larger information depth) it is likely that several different phases within the self-healing products are analysed in the same point. The measured compositions should therefore be evaluated together with the pictures of the cracks (Figure 47, Figure 48 and Figure 49 and Appendix 9). The results presented in Table 13 to Table 15 are normalized to 100%. Therefore, elemental ratios in atom% (e.g. Mg/Ca) should be considered rather than directly comparing the atom% of single elements in different measurements.

In Table 13, Table 14 and Table 15 areas where no measurement was possible, e.g. due to a too small crack width, are marked in grey. Points most likely representing aggregate/particles from concrete are marked in yellow. Points that were taken in narrow cracks and thus with the possibility of analysing parts of the surrounding concrete are marked in orange/brown.

In general, precipitation of Mg and Ca rich phases from seawater seems to be the dominating self-healing mechanism in all exposure zones.

Beam B

Due to too small crack width, no measurements were taken in cracks of cores BAC, BTCr2 and BTCr4.

Within the first 5 mm of the crack in core BTC, loose grains were observed, probably from the cutting/drilling of the concrete cores. The high amount of Na, Al and Si in core BTC at a crack depth of 5 mm represents most likely a feldspar grain from the concrete. At 10 and 15 mm the composition was rich in Mg, Ca and Si. The high Mg and Ca content are signs of self-healing due to precipitation from seawater.

In core BSC lower amounts of Mg were detected compared to BTC. Furthermore, some chloride and sulphate was measured. Due to the narrow crack width, it is likely that in addition to the self-healing products parts of the surrounding concrete were measured.

Beam E

The crack in core ETC was extensively self-healed and wide enough within the first 15 mm to give representative measurements of the self-healing products. It appears that the Mg content increases with increased crack depth. In addition, lower amounts of Ca were measured at a

crack depth of 15 mm compared to the surface (5 mm). The very high standard deviations in some points (e.g. ETC 5 mm and 10 mm, and ETCr4 15 mm) should be noted.

The crack of sample ETCr2 appeared open within the first 10 mm and the composition measured in points at 5 and 10 mm most likely represents aggregate particles e.g. feldspars (Al-silicates with Na or Ca and possible substitution with K). At a crack depth of 15 mm high amounts of Mg were found in the self-healing product. At a crack depth of 20 mm the crack was only partly closed, and the composition seems to represent a combination of self-healing products (Mg, Ca) and K-feldspar minerals from the concrete.

In the submerged zone (ESC), high amounts of Mg, Ca and Si were observed already at a depth of 5 mm. At a crack depth of 10 mm the crack was difficult to locate with the μ -XRF and the composition shows that most likely an aggregate particle from the concrete was measured.

Beam F

In Beam F, the trend of increasing amounts of Mg with increasing crack depth was not observed. Relative high amounts of Mg and Ca were measured inside the crack of sample FAC, already at a depth of 5 mm. As the crack was narrow, the surrounding concrete was also analysed in parts as indicated by the relatively high amounts of Si, Al and alkalis.

The composition at a crack depth of 5 mm in sample FTC represents quartz and feldspar from aggregates. At a crack depth of 15 mm the self-healing product has a similar composition as in sample FAC. At a crack depth of 20 mm, relatively high amounts of Na and Cl were measured besides high amounts of Mg. This is the only point where such high amounts of Na and Cl were observed. A possible explanation might simply be precipitation of NaCl salt from seawater in addition to brucite ($\text{Mg}(\text{OH})_2$). Precipitation of Mg and Ca rich products was also found inside the crack of sample FTCr2 at a crack depth of 5 and 10 mm. A similar composition was found at a crack depth of 15 mm in sample FTCr4. However, in core FTCr4 high amounts of Ca and almost no Mg were detected at a crack depth of 5 mm.

The crack in sample FSC was very narrow and the measured composition at a crack depth of 15 and 20 mm seems mainly to represent aggregates and cement paste.

Table 13: Composition of self-healing products (atom%) measured in Beam B using μ -XRF

Crack depth (mm)	Element	BAC	BTC	BTCr2	BTCr4	BSC
5	Na		9.5 ± 1.8			-
	Mg		1.3 ± 1.5			5.4 ± 0.3
	Al		18.4 ± 0.8			3.0 ± 0.3
	Si		55.5 ± 4.5			13.0 ± 0.5
	S		-			-
	Cl		-			2.2 ± 0.2
	K		4.1 ± 2.6			-
	Ca		8.4 ± 5.4			71.9 ± 0.2
	Fe		2.2 ± 0.9			3.6 ± 0.1
10	Na		-			-
	Mg		25.6 ± 1.0			9.7 ± 4.1
	Al		1.4 ± 0.3			2.8 ± 0.7
	Si		6.1 ± 1.5			13.0 ± 3.7
	S		-			-
	Cl		-			1.8 ± 0.4
	K		-			-
	Ca		66.1 ± 0.9			69.0 ± 3.1
	Fe		-			2.2 ± 1.2
15	Na		-			-
	Mg		50.7 ± 6.6			-
	Al		2.4 ± 0.8			6.1 ± 0.6
	Si		12.2 ± 3.9			21.2 ± 1.1
	S		-			3.7 ± 1.1
	Cl		-			2.8 ± 0.5
	K		-			2.1 ± 0.3
	Ca		32.3 ± 0.4			59.0 ± 1.3
	Fe		1.2 ± 0.8			3.6 ± 0.4

- below 1 atom%

Not possible to measure due to too small crack width

Aggregate/Concrete

Narrow crack, potential impact of surrounding concrete

Table 14: Composition of self-healing products (atom%) measured in Beam E using μ -XRF

Crack depth (mm)	Element	EAC	ETC	ETCr2	ETCr4	ESC
5	Na		2.4 ± 2.5	8.5 ± 3.1	-	-
	Mg		1.5 ± 0.5	-	2.6 ± 0.6	50.3 ± 3.0
	Al		4.2 ± 2.7	13.5 ± 3.3	7.4 ± 0.7	-
	Si		27.9 ± 24.8	50.8 ± 5.5	33.4 ± 9.6	9.3 ± 3.1
	S		-	-	1.8 ± 0.2	-
	Cl		-	-	-	-
	K		-	5.4 ± 1.6	-	-
	Ca		62.4 ± 27.3	19.7 ± 11.1	49.2 ± 7.9	36.7 ± 1.9
	Fe		-	1.0 ± 0.5	3.1 ± 0.7	2.1 ± 0.1
	10	Na		-	9.2 ± 5.4	2.1 ± 1.8
Mg			14.9 ± 11.9	-	17.3 ± 7.5	-
Al			2.3 ± 1.0	13.7 ± 6.9	9.8 ± 0.9	14.8 ± 0.9
Si			7.9 ± 4.4	64.1 ± 11.6	42.6 ± 7.6	44.8 ± 11.8
S			-	-	-	-
Cl			-	-	-	-
K			-	4.1 ± 1.7	4.3 ± 2.5	12.1 ± 7.6
Ca			73.5 ± 10.1	8.4 ± 0.9	22.6 ± 2.3	22.9 ± 18.1
Fe			-	-	-	2.0 ± 1.5
15		Na		-	-	-
	Mg		40.4 ± 3.0	48.0 ± 5.9	30.0 ± 8.8	
	Al		8.1 ± 2.6	2.2 ± 1.2	4.7 ± 0.8	
	Si		21.7 ± 3.4	8.5 ± 6.2	39.3 ± 17.2	
	S		-	-	-	
	Cl		-	-	-	
	K		-	-	-	
	Ca		26.7 ± 7.2	39.5 ± 6.0	23.5 ± 10.9	
	Fe		-	-	-	
	20	Na			-	
Mg				16.3 ± 6.1		
Al				11.8 ± 1.2		
Si				37.7 ± 6.3		
S				-		
Cl				-		
K				9.6 ± 2.9		
Ca				23.8 ± 9.7		
Fe				-		

- below 1 atom%

Not possible to measure due to too small crack width

Aggregate/Concrete

Narrow crack, potential impact of surrounding concrete

Table 15: Composition of self-healing products (atom%) measured in Beam F using μ -XRF

Crack depth (mm)	Element	FAC	FTC	FTCr2	FTCr4	FSC
5	Na	2.0 ± 2.1	-	-	-	
	Mg	30.4 ± 11.5	-	43.9 ± 7.5	2.4 ± 0.6	
	Al	9.3 ± 2.4	4.9 ± 4.5	1.0 ± 0.2	4.5 ± 3.0	
	Si	30.1 ± 3.6	82.9 ± 12.1	5.7 ± 0.6	11.1 ± 2.8	
	S	-	-	-	-	
	Cl	-	-	-	-	
	K	3.2 ± 1.5	7.0 ± 6.9	-	-	
	Ca	24.5 ± 2.3	3.5 ± 1.6	47.9 ± 8.1	78.2 ± 7.1	
	Fe	-	-	0.8 ± 0.5	1.5 ± 0.3	
10	Na	2.2 ± 1.8		1.1 ± 1.3		
	Mg	18.3 ± 5.6		43.2 ± 11.2		
	Al	12.1 ± 1.5		6.8 ± 2.5		
	Si	37.7 ± 3.4		22.2 ± 7.4		
	S	-		-		
	Cl	-		-		
	K	6.9 ± 5.1		1.4 ± 0.06		
	Ca	21.9 ± 2.7		23.6 ± 1.5		
	Fe	-		-		
15	Na	-	-		-	6.8 ± 0.9
	Mg	33.5 ± 5.6	39.7 ± 3.1		46.2 ± 0.3	6.8 ± 1.3
	Al	4.2 ± 0.6	1.3 ± 0.3		4.5 ± 0.3	9.0 ± 0.6
	Si	22.5 ± 0.7	27.5 ± 22.3		21.0 ± 1.1	33.7 ± 2.5
	S	1.0 ± 0.1	-		-	-
	Cl	-	1.5 ± 0.6		-	-
	K	-	-		-	1.7 ± 0.3
	Ca	34.3 ± 5.4	54.0 ± 24.1		25.2 ± 1.3	39.3 ± 3.3
	Fe	2.3 ± 0.2	-		-	1.4 ± 0.2
20	Na		12.2 ± 2.2			5.0 ± 1.2
	Mg		39.7 ± 3.1			1.8 ± 0.2
	Al		1.3 ± 0.3			8.9 ± 1.3
	Si		1.1 ± 4.4			25.7 ± 3.3
	S		-			4.8 ± 0.3
	Cl		19.4 ± 3.6			-
	K		3.7 ± 0.5			1.4 ± 0.2
	Ca		1.4 ± 0.6			50.8 ± 5.8
	Fe		-			1.3 ± 0.2

- below 1 atomic%

Not possible to measure due to too small crack width

Aggregate/Concrete

Narrow crack, potential impact of surrounding concrete

A more detailed investigation on the impact of the three binders on the extent and composition of self-healing, including SEM and polarization microscopy analysis, is presented in [29]. It was concluded that the binder had no effect on the extent of self-healing and neither on the composition of self-healing products observed at different crack depth. A typical mineralogical

sequence of self-healing products was observed and the following mechanism is proposed (Figure 50).

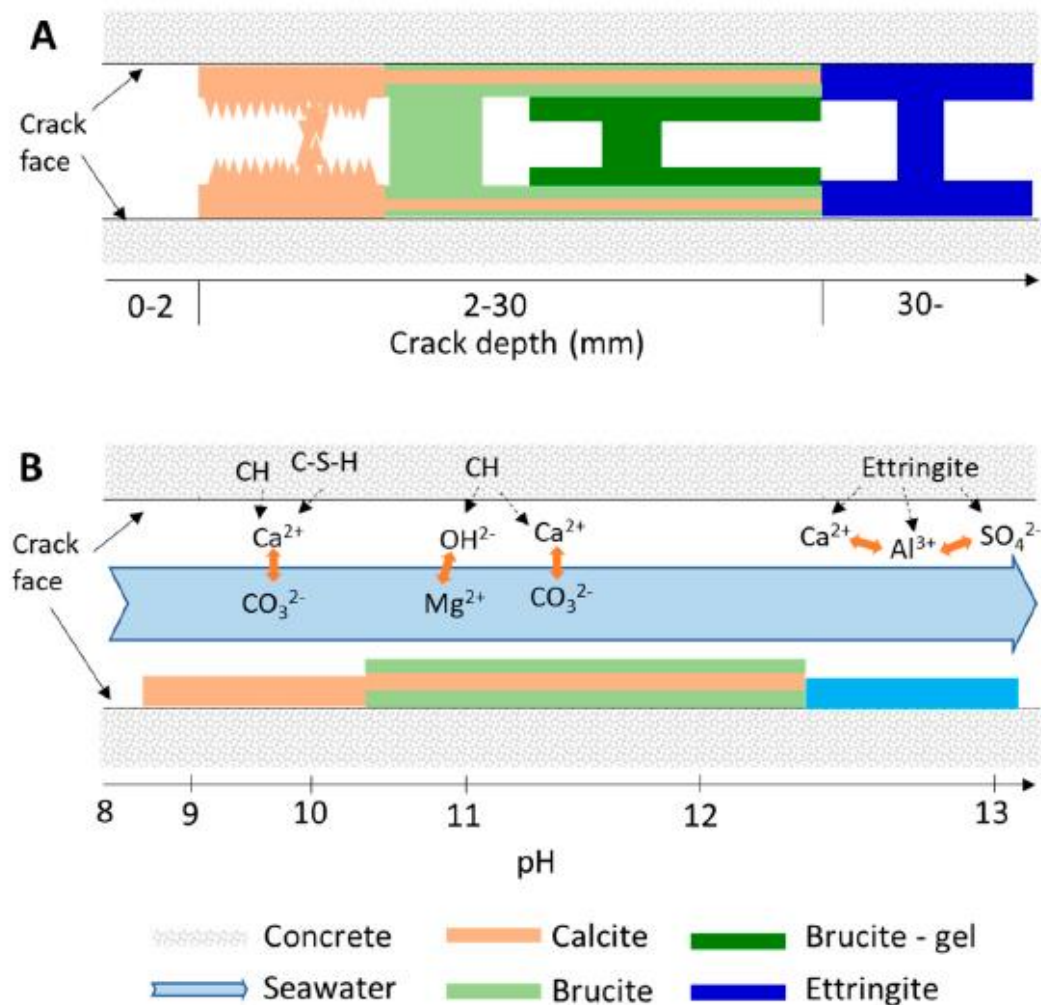


Figure 50: A: Mineralogical sequence of self-healing products with increased crack depth; B: proposed self-healing mechanism [29]

In the outer faces of the crack (0-5 mm) only calcium carbonate was precipitated followed by brucite layers from 5-30 mm. The brucite was occasionally intermixed with calcite. At crack depths >30 mm only ettringite was observed. In the outer part of the crack precipitation of ions from seawater partly in reaction with ions from the cement paste appeared to be the dominating mechanism. At larger crack depth, ettringite formation occurred due to the dissolution and reprecipitation of hydrate phases. The results indicated that the mineralogical sequence observed with increasing crack depth occurs due to an increasing pH of the solution inside the crack with increased crack depth. [29]

6.9 Extent of reinforcement corrosion

When opening the beams and inspecting the reinforcement, the steel was generally in a very good state. Severe pitting corrosion was found at the location of some of the spacers (4 out of 24). Small distributed pitting was found at 6 out of the remaining 20 spacers, at two cracks and one location neither coinciding with cracks nor spacers. Traces of superficial rust were observed over the entire reinforcement, independently of cracks and spacers.

Corrosion maps of all three concrete beams are shown in Figure 51. Corrosion at spacers was mainly found in the tidal zone. Table 16 gives an overview of all corrosion pits observed after removing the concrete cover and cleaning the reinforcement. The table includes estimates of corrosion rates. The calculated corrosion rates are based on several assumption (see Chapter 5.11), the assumptions on geometry lead to overestimation, whereas the assumption on duration leads to underestimation. Figure 52 and Figure 53 show examples of severe pitting corrosion and distributed pitting at spacers, respectively. Pictures of rust products were taken right after opening the beams. In Figure 52, it can be seen that the rust products had a dark, black and green colour, typical for lack of oxygen and presence of chloride. Dark corrosion products were observed as well at the other places where severe pitting was observed.

Pictures of the split and cut concrete surfaces including the steel-concrete interface are given in Appendix 11. In some pictures from Appendix 11, traces of superficial rust are visible at the reinforcement. The rust was mainly located at the sides of the reinforcement not oriented towards the smallest cover. After cleaning the reinforcement no corrosion damage could be observed at these places. It is assumed that the observed traces of rust originate from the casting of the concrete.

Visually, all beams were well compacted. A higher amount voids was observed in Beam E compared to B and F; also at the steel-concrete interface. The voids were spread randomly and there was no apparent impact of the casting direction. Full imprints of the reinforcement were observed indicating absence of bleeding. The only corrosion spot not coinciding with a spacer or a crack was neither related to a void.

Despite the high chloride concentrations observed in the submerged parts of Beam B and Beam F (see Figures 31 and 33), no corrosion was observed in the submerged part of Beam F and only limited corrosion was observed in Beam B (at spacer in Line 4, 280 cm and slightly below).

In general, correlation is found between potential drops (Figure 20-22) and observed corrosion at spacers (Figure 52). Corrosion is observed at most of the spacers in the tidal zone (Beam B: 2 of 4, Beam E: 3 of 4, Beam F: 4 of 4). In contrast, limited corrosion is observed at cracks. The limited corrosion at cracks might be explained by corrosion at spacers inhibiting corrosion at cracks or by early self-healing of the cracks. Corrosion at spacers protecting the steel in other areas was recently supported by numerical simulations [30].

At the initial visual inspection of the beams, concrete spalling and corrosion products were observed on the concrete surface at locations of spacers in Beam B and Beam F. The cause of spalling is not clear. The spacers used in the concrete beams were made of plastic with four

legs towards both formwork and reinforcement (Figure 54). The spacers appear to have been fixed to the formwork with a metal nail positioned in the centre of the spacer (Figure 54) or through one of the legs (Appendix 4). An apparent imprint of the head of such a nail was observed on one rebar indicating galvanic corrosion of the rebar (Figure 53). It is hypothesized that more severe corrosion at other spacers was initiated by galvanic corrosion. Sustained corrosion development might have been supported by more rapid ingress of aggressive substances in the vicinity of the plastic spacer [31] and later by spalling of the concrete cover. Visual inspection of the concrete confined in a spacer showed a paste rich, but well compacted concrete (see Appendix 10).

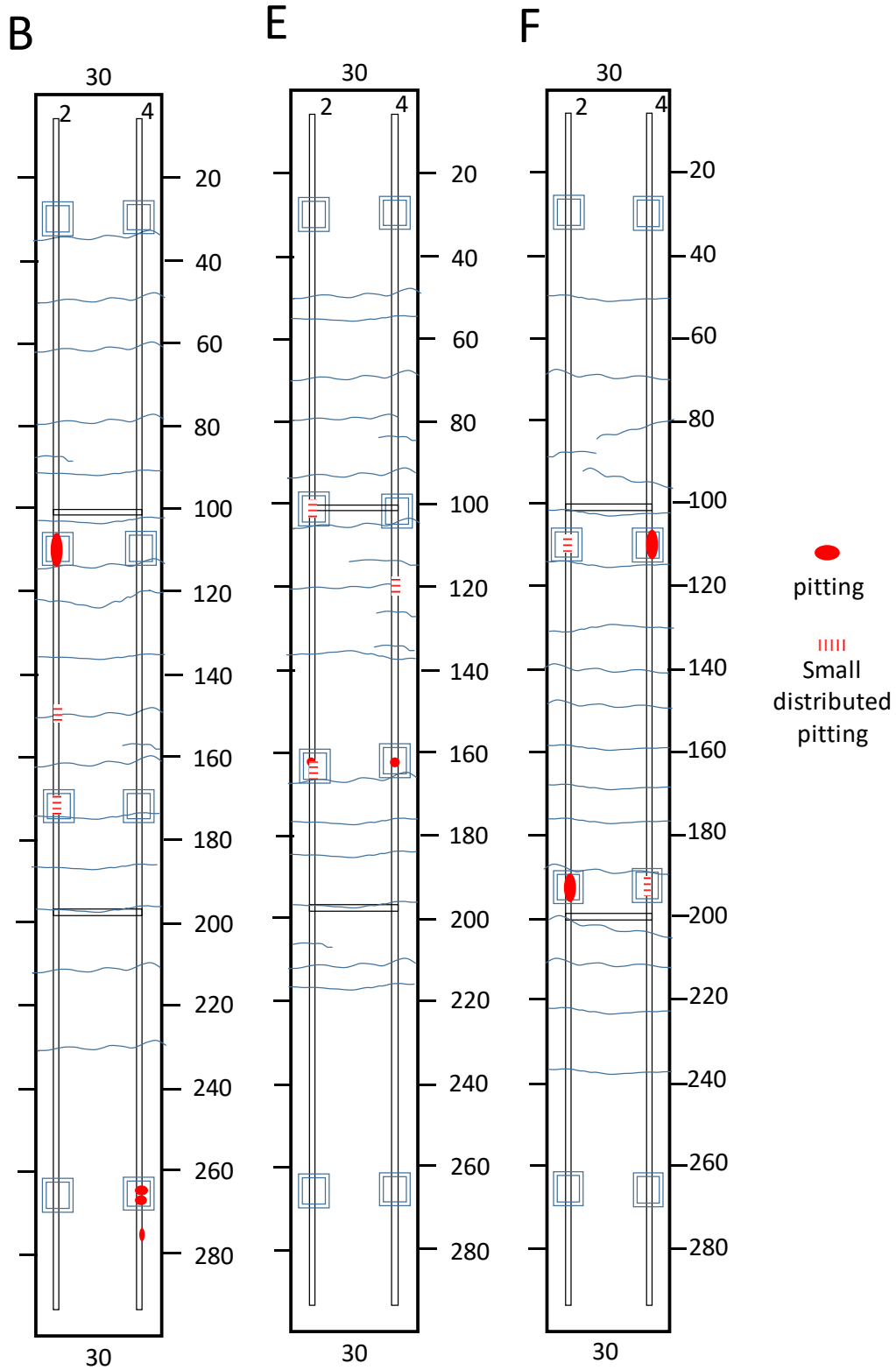


Figure 51: Corrosion maps of Beam B, Beam E and Beam F with scale in cm. (Note: different orientation of Beam F on the ferry quay; Line 2 directed towards ferry quay, see Figure 7)

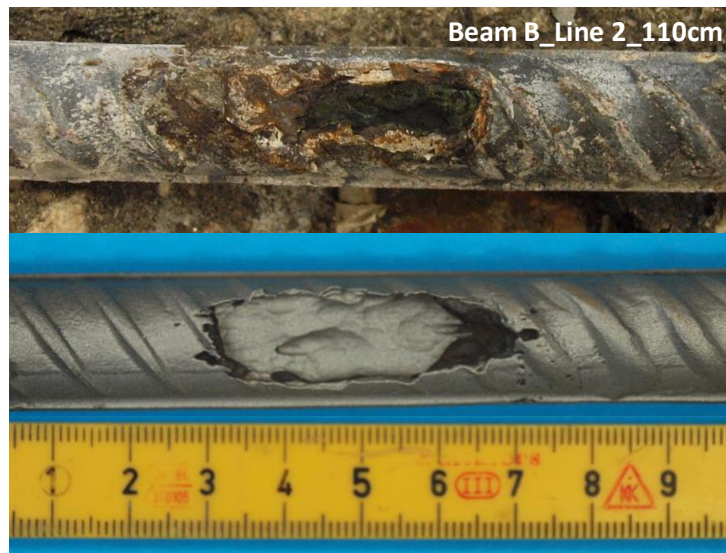


Figure 52: Severe pitting corrosion at a spacer in the tidal zone of Beam B. Location at around 110 cm at Line 2

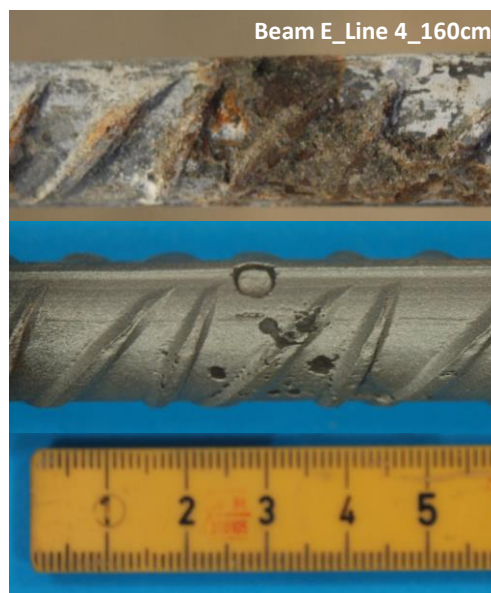
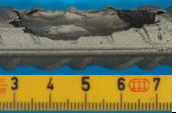









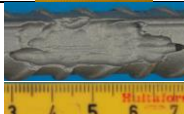




Figure 53: Distributed pitting at a spacer in the tidal zone of Beam E. Location at around 160 cm at Line 2



Figure 54: Representative plastic spacer removed from Beam B showing a nail in the middle with potential contact to the reinforcement steel

Table 16: Description of the corroding areas including beam, location, geometry of pits (measured using a caliper (accuracy 0.01 mm)), pictures of pits (after sandblasting) and estimated average corrosion rate

Beam	Location	Geometry (mm) (Length \pm 1 / Depth \pm 0.5)	Picture	Estimated average corrosion rate ($\mu\text{m}/\text{year}$)
B	Line 2, 110 cm (spacer)	44 / 6		60 ± 10
B	Line 2, 150 cm (crack)	Small distributed pitting*		<1
B	Line 2, 170 cm (spacer)	Small distributed pitting*		<1
B	Line 4, 265 cm (spacer)	27 / 3		20 ± 5
B	Line 4, 275 cm (bulk)	2 / 0.7 3 / 0.9		2 ± 1
E	Line 2, 100 cm (spacer)	Small distributed pitting*		<1
E	Line 2, 160 cm (spacer)	5 / 1		2 ± 1
E	Line 4, 120 cm (crack)	Small distributed pitting		<1
E	Line 4, 160 cm (spacer)	14 / 0.9		2 ± 1
F	Line 2, 110 cm (spacer)	Small distributed pitting*		<1
F	Line 2, 190 cm (spacer)	48 / 5		45 ± 5
F	Line 4, 110 cm (spacer)	34 / 4.5		40 ± 5
F	Line 4, 190 cm (spacer)	Small distributed pitting*		<1

* Small distributed pitting is defined as corrosion spots with a depth lower than 0.5 mm, which approximately corresponds to a corrosion rate lower than 1 $\mu\text{m}/\text{year}$

References

1. Boschmann Käthler, A.C., et al., *No. 454 - Effect of cracks on chloride induced corrosion of steel in concrete - a review*, in *NPRA reports*, N.P.R. Administration, Editor. 2017.
2. Pease, B., *Influence of concrete cracking on ingress and reinforcement corrosion*, in *Department of civil engineering*. 2010, Technical University of Denmark.
3. Society, T.C., *Relevance of cracking in concrete to reinforcement corrosion - Technical report 44*, T.C. Society, Editor. 2015.
4. Hornbostel, K. and M.R. Geiker. *Influence of cracking on reinforcement corrosion*. in *Nordic mini-seminar: Crack width Calculation methods for large concrete structures 2017*. Oslo, Norway.
5. De Rooij, M., et al., *Self healing phenomena in cement-based materials, State of the art report from RILEM Technical Committee 221-SHC*, ed. M. De Rooij. 2013.
6. Maes, M., D. Snoeck, and N. De Belie, *Chloride penetration in cracked mortar and the influence of autogenous crack healing*. *Construction and Building Materials*, 2016. **115**: p. 114-124.
7. Na, S.H., et al., *Experimental Investigation on Reaction Rate and Self-healing Ability in Fly Ash Blended Cement Mixtures*. *Journal of Advanced Concrete Technology*, 2012. **10**(7): p. 240-253.
8. Şahmaran, M., et al., *Self-healing of mechanically-loaded self consolidating concretes with high volumes of fly ash*. *Cement and Concrete Composites*, 2008. **30**(10): p. 872-879.
9. Termkhajornkit, P., et al., *Self-healing ability of fly ash–cement systems*. *Cement and Concrete Composites*, 2009. **31**(3): p. 195-203.
10. Jacobsen, S., J. Marchand, and H. Hornain, *Sem observations of the microstructure of frost deteriorated and self-healed concretes*. *Cement and Concrete Research*, 1995. **25**(8): p. 1781-1790.
11. Jacobsen, S. and E.J. Sellevold, *Self healing of high strength concrete after deterioration by freeze/thaw*. *Cement and Concrete Research*, 1996. **26**(1): p. 55-62.
12. Holtmon, J.P. and H.R. Iskasen, *Utvikling av kloridbestandig betong - Rapport fra produksjon av prøveelementer*. 1994, Vegdirektoratet: Oslo, Norway.
13. <https://www.tide-forecast.com/locations/Sandnessjoen/tides/latest>. 2017.
14. Østnor, T., M. Haugen, and K. De Weerd, *Kloridbestandig Betong Fase I - Avrop 23*, S. Byggforsk, Editor. 2015.
15. De Weerd, K., et al., *Towards the understanding of chloride profiles in marine exposed concrete, impact of leaching and moisture content*. *Construction and Building Materials*, 2016. **120**: p. 418-431.
16. Vegdirektoratet, *Retningslinje, Håndbok R211 Feltundersøkelser 2014*: Oslo, Norway.
17. Vegdirektoratet, *Retningslinje, Håndbok R210, Laboratorieundersøkelser*. 2016: Oslo, Norway.
18. Polder, R.B., *Test methods for on site measurement of resistivity of concrete — a RILEM TC-154 technical recommendation*. *Construction and Building Materials*, 2001. **15**(2): p. 125-131.
19. Belda Revert, A., et al., *Carbonation-induced corrosion: Investigation of the corrosion onset*. *Construction and Building Materials*, 2018. **162**: p. 847-856.
20. Lindgård, J., et al., *Alkali–silica reaction (ASR)—performance testing: Influence of specimen pre-treatment, exposure conditions and prism size on concrete porosity*,

- moisture state and transport properties*. Cement and Concrete Research, 2013. **53**: p. 145-167.
21. Vaisala. *HM44 Datasheet B211768 EN-A - Vaisala*. 2018.
 22. Danner, T., K. De Weerd, and M.R. Geiker. μ -XRF – CHARACTERISATION OF CHLORIDE INGRESS AND SELF-HEALING IN CRACKED CONCRETE. in *XXIIIth Symposium on Nordic Concrete Research & Development*. 2017. Aalborg, Denmark.
 23. Myklebust, S. and R. Moastuen, *Selvreparasjon og påvirkningen av riss på armeringens tilstand i opprisset betong*, in *Department of Structural Engineering*. 2018, Norwegian University of Science and Technology: Trondheim.
 24. Angst, U., et al., *Critical chloride content in reinforced concrete — A review*. Cement and Concrete Research, 2009. **39**(12): p. 1122-1138.
 25. Fluge, F., *Marine chlorides – a probabilistic approach to drive provisions for EN 206-1*, in *Duranet 3rd Workshop – Service Life Design of Concrete Structures – from Theory to Standardisation*. 2001: Tromsø, Norway.
 26. Melchers, R.E., et al., *Long-term durability of reinforced concrete piles from the Hornibrook Highway Bridge*. Australian Journal of Structural Engineering, 2017. **18**(1): p. 41-57.
 27. Michel, A., et al., *Experimental investigation of the relation between damage at the concrete-steel interface and initiation of reinforcement corrosion in plain and fibre reinforced concrete*. Cement and Concrete Research, 2013. **77**: p. 308-321.
 28. Jakobsen, U.H., *Report No.: 829235, Microscopy of phases formed in cracks of 25 years old seawater exposed concrete*. 2018, Danish Technological Institute (DTI): Taastrup, Denmark.
 29. Danner, T., U.H. Jakobsen, and M.R. Geiker, *Mineralogical sequence of self-healing products in cracked marine concrete*. Minerals, 2019. **9**(5): p. 284.
 30. Geiker, M., et al., *25 years field exposure of pre-cracked concrete beams; combined impact of spacers and cracks on reinforcement corrosion*. submitted to Cement and Concrete Research, 2020.
 31. Alzyoud, S., H.S. Wong, and N.R. Buenfeld, *Influence of reinforcement spacers on mass transport properties and durability of concrete structures*. Cement and Concrete Research, 2016. **87**: p. 31-44.

Appendix

Field station Sandnessjøen – Effect of cracks in concrete after 25 years, Data report

List of appendices

Appendix 1: Drawings of the concrete beams	61
Appendix 2: Location of concrete cores	62
Appendix 3: Pictures of top surface of concrete beams.....	65
Appendix 4: Half-cell potential measurements.....	68
Appendix 5: Resistivity.....	74
Appendix 6: Moisture – Raw data and comparison of different methods	77
Appendix 7: Chloride profile results.....	93
Appendix 8: Ingress of chloride and sulfate in cracks and along reinforcement measured with μ -XRF	94
Appendix 9: Overview and detailed pictures of self-healing in cracks	99
Appendix 10: Pictures of the splitted concrete beams	105

Appendix 1: Drawings of the concrete beams

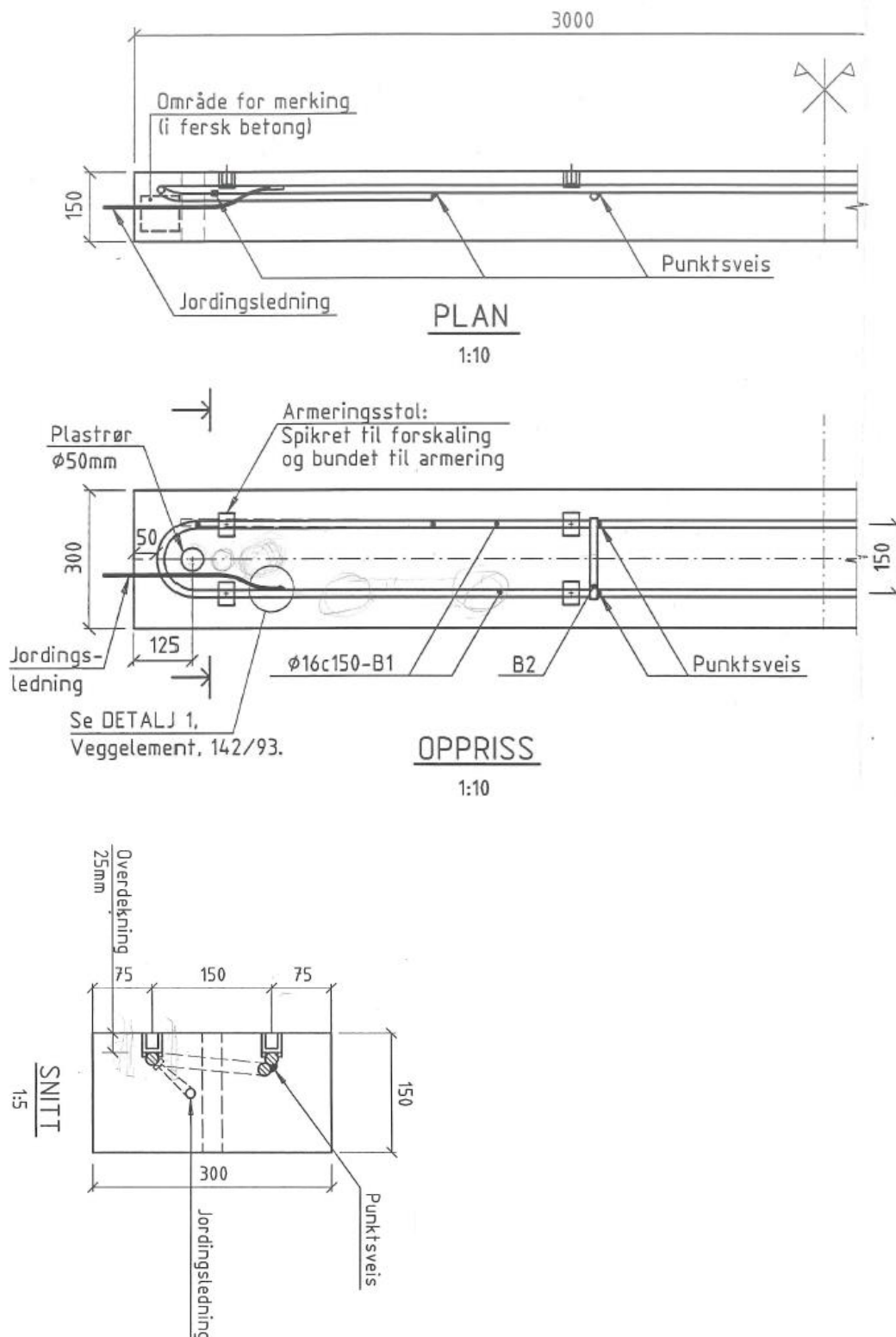


Figure 1: Constructional drawing of the concrete beams. From Holtmon J.P. & Isaksen H.R., "Utvikling av kloridbestandig betong - Rapport fra produksjon av prøveelementer", Vegdirektoratet, Bruavdeling, 1994

Appendix 2: Location of concrete cores



Figure 2: Location of concrete cores taken from Beam B, distance in meters (Photos: Eva Rodum)



Figure 3: Location of concrete cores taken from Beam E, distance in meters (Photos: Eva Rodum)

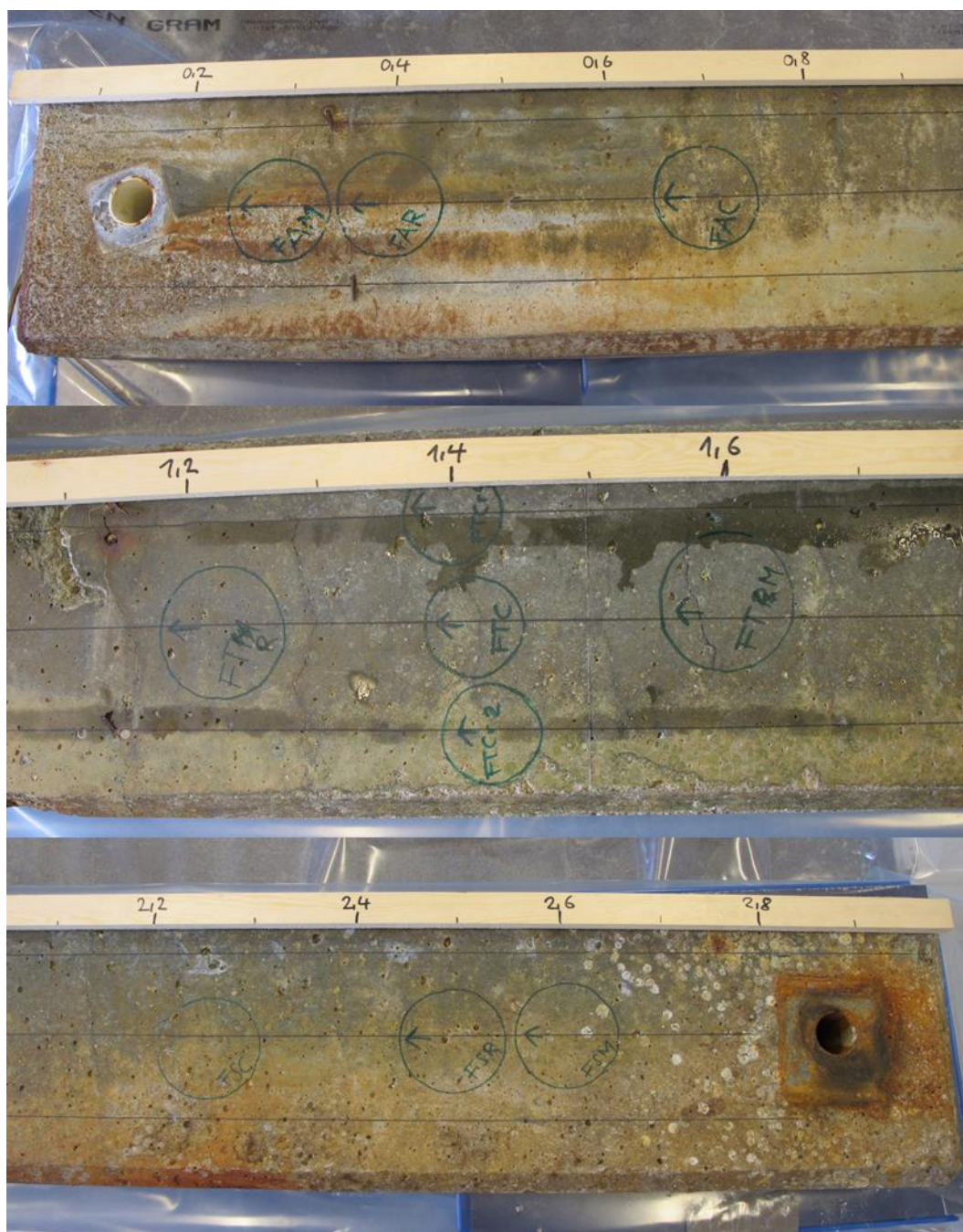


Figure 4: Location of concrete cores taken from Beam F, distance in meters (Photos: Eva Rodum)

Appendix 3: Pictures of top surface of concrete beams

Pictures taken by Ragnhild Moastuen and Solveig Myklebust. Figures prepared by Tobias Danner

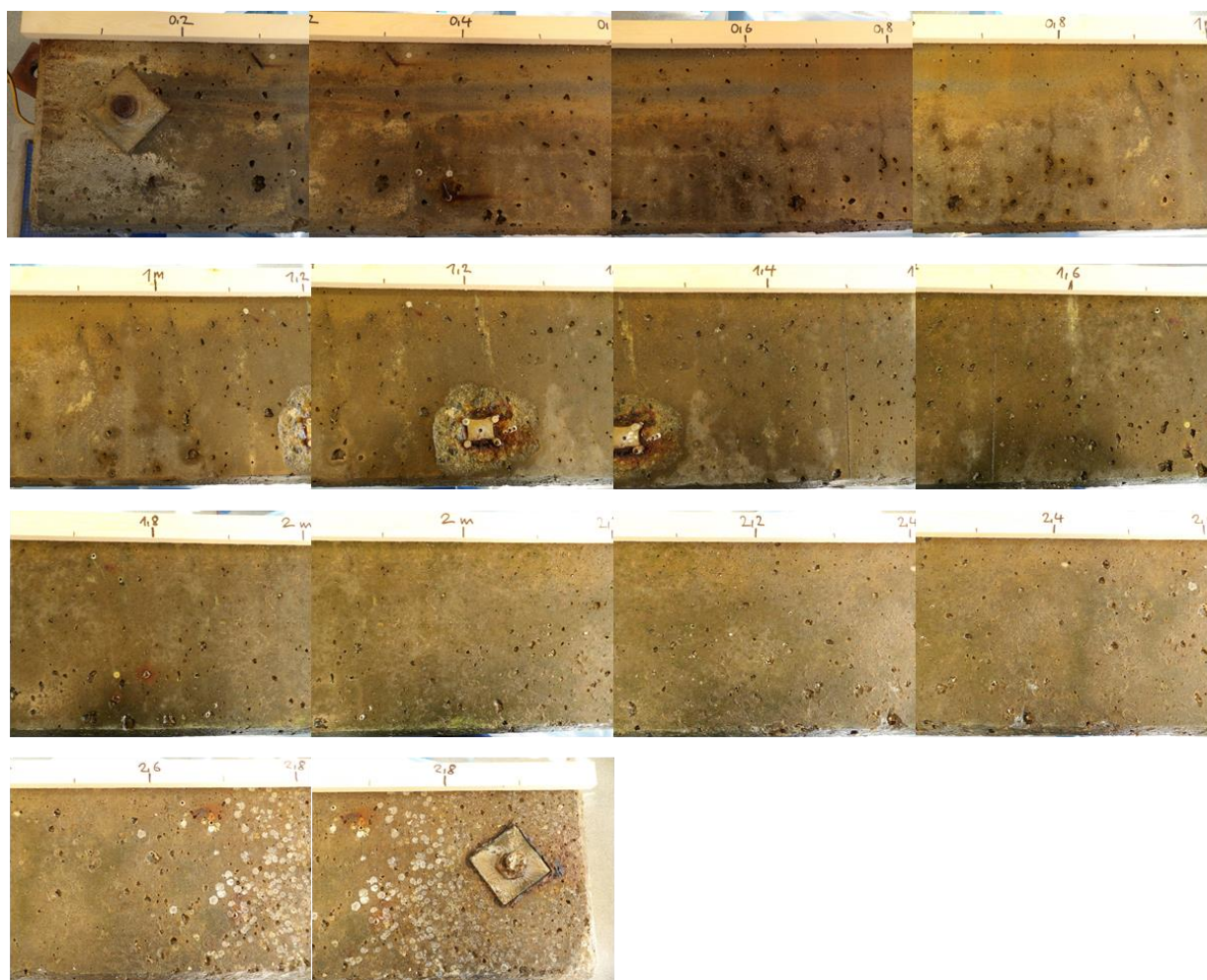


Figure 5: Pictures of the top concrete surface of concrete Beam B taken after arrival in the laboratory at NTNU, distance in meters (Photos: Ragnhild Moastuen og Solveig Myklebust)

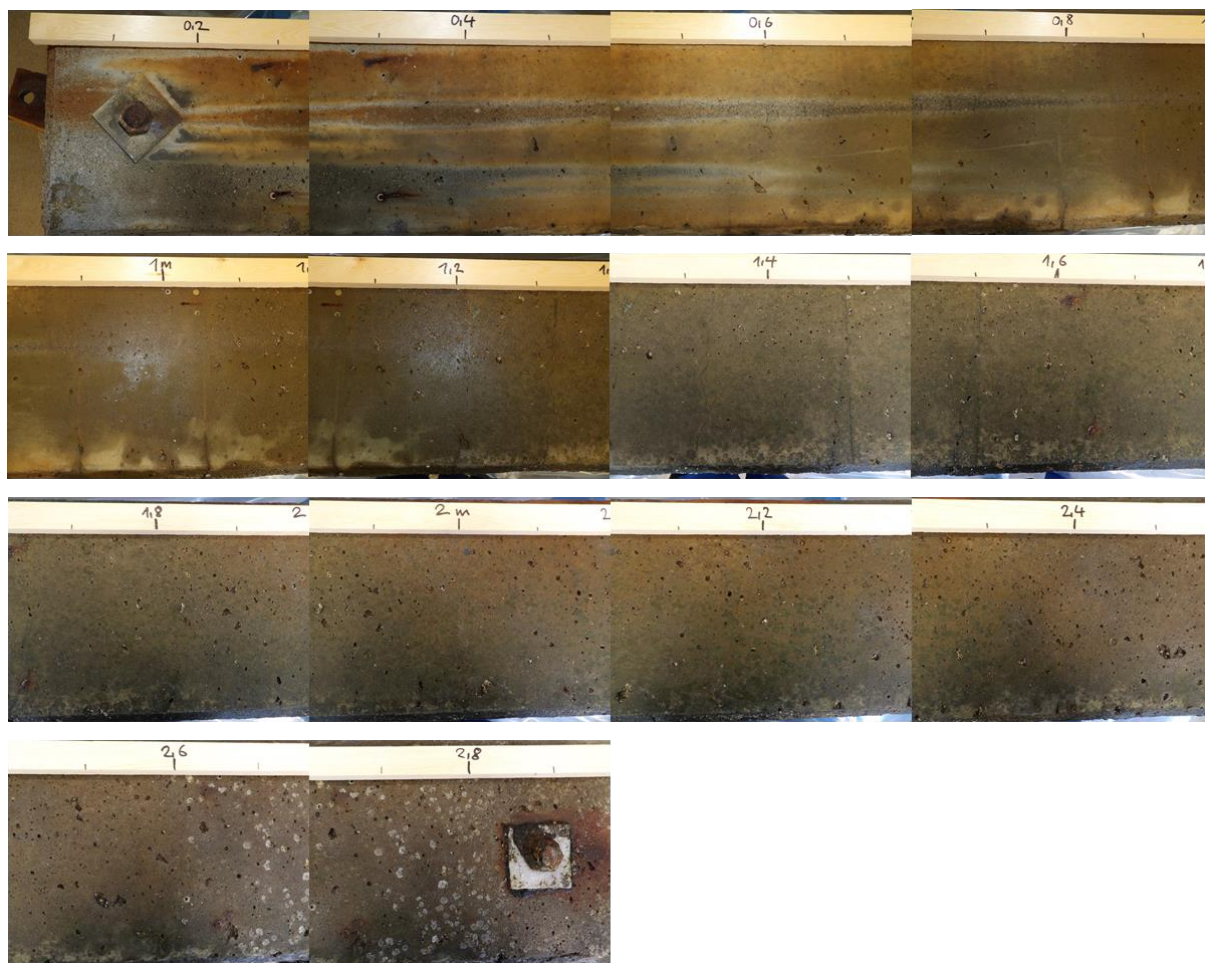


Figure 6: Pictures of the top concrete surface of concrete Beam E taken after arrival in the laboratory at NTNU, distance in meters (Photos: Ragnhild Moastuen and Solveig Myklebust)

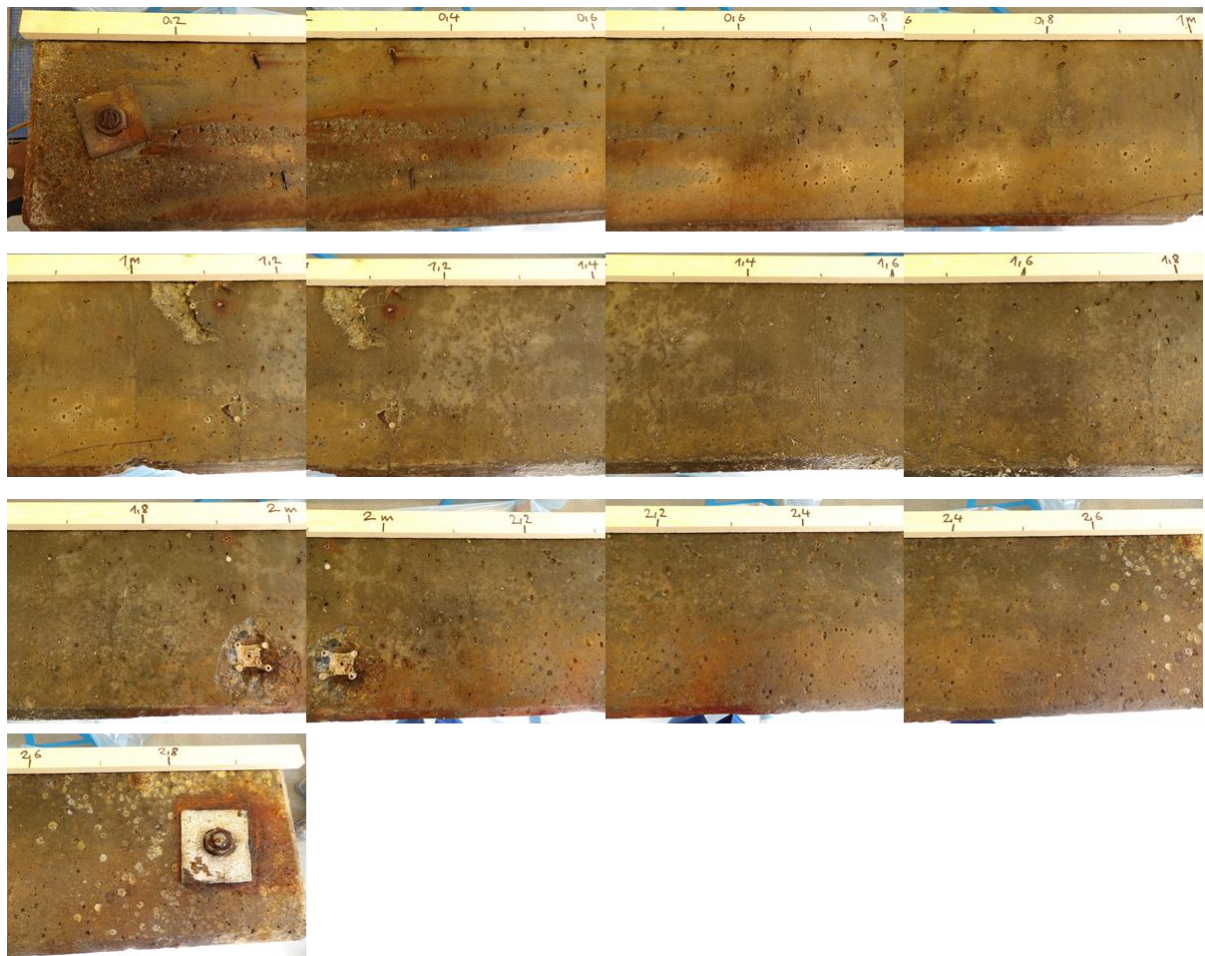


Figure 7: Pictures of the top concrete surface of concrete Beam F taken after arrival in the laboratory at NTNU, distance in meters (Photos: Ragnhild Moastuen and Solveig Myklebust)

Appendix 4: Half-cell potential

Measurements performed by Solveig Myklebust and Ragnhild Moastuen. Figures prepared by Tobias Danner.

Beam B		Date:	16. Mars						
		Temperature	Laboratory						
		Cover	25 mm						
		Equipment	Wheel				Rod		
Position (m)	Line 1 (Left side)	Line 2	Line 4	Line 5 (Right side)	Line 2	Line 4			
Atmospheric zone	0	-192	-229	-204	-195	-195	-197		
	5	-180	-217	-210	-195	-195	-232		
	10	-176	-214	-189	-203	-203	-202		
	15	-185	-191	-185	-193	-193	-197		
	20	-187	-171	-190	-177	-177	-190		
	25	-210	-215	-205	-172	-172	-169		
	30	-235	-267	-220	-177	-177	-192		
	35	-243	-269	-228	-189	-189	-199		
	40	-247	-222	-251	-205	-205	-234		
Tidal zone	45	-266	-246	-258	-217	-217	-244		
	50	-277	-249	-271	-238	-238	-253		
	55	-287	-290	-283	-252	-252	-260		
	60	-298	-301	-303	-254	-254	-267		
	65	-311	-298	-300	-262	-262	-273		
	70	-319	-306	-309	-270	-270	-278		
	75	-321	-292	-320	-288	-288	-298		
	80	-331	-300	-320	-311	-311	-300		
	85	-338	-331	-321	-316	-316	-308		
	90	-342	-346	-340	-325	-325	-308		
	95	-352	-349	-343	-331	-331	-322		
	100	-326	-350	-352	-342	-342	-326		
	105	-332	-370	-352	-348	-348	-334		
	110	-334	-404	-344	-345	-345	-341		
	115	-346	-507	-342	-347	-347	-337		
	120	-346	-465	-344	-336	-336	-331		
	125	-345	-344	-347	-332	-332	-331		
	130	-340	-336	-346	-340	-340	-352		
	135	-343	-352	-339	-339	-339	-346		
	140	-348	-352	-341	-342	-342	-336		
	145	-350	-329	-345	-341	-341	-329		
	150	-349	-336	-356	-345	-345	-327		
	155	-358	-336	-360	-345	-345	-327		
	160	-364	-336	-359	-355	-355	-336		
	165	-380	-351	-375	-359	-359	-333		
	170	-379	-355	-376	-364	-364	-358		
	175	-387	-347	-375	-377	-377	-341		
	180	-399	-342	-375	-376	-376	-371		
	185	-407	-338	-380	-377	-377	-377		
	190	-422	-355	-385	-393	-393	-380		
195	-429	-358	-389	-394	-394	-374			
200	-435	-360	-388	-394	-394	-368			
205	-445	-373	-397	-395	-395	-387			
210	-443	-382	-397	-399	-399	-390			
215	-438	-406	-399	-412	-412	-393			
220	-437	-415	-419	-406	-406	-408			
225	-441	-424	-434	-436	-436	-398			
230	-456	-427	-433	-431	-431	-387			
235	-460	-423	-452	-444	-444	-424			
240	-457	-438	-478	-451	-451	-433			
245	-442	-440	-486	-454	-454	-422			
250	-442	-442	-474	-463	-463	-420			
Submerged zone	255	-430	-457	-464	-463	-463	-478		
	260	-431	-459	-467	-454	-454	-500		
	265	-440	-468	-462	-459	-459	-480		
	270	-455	-459	-450	-458	-458	-472		
	275	-456	-454	-460	-442	-442	-478		
	280		-453	-464	-440	-440	-484		
285		-469	-387	-452	-452	-465			
290		-472		-452	-452	-440			

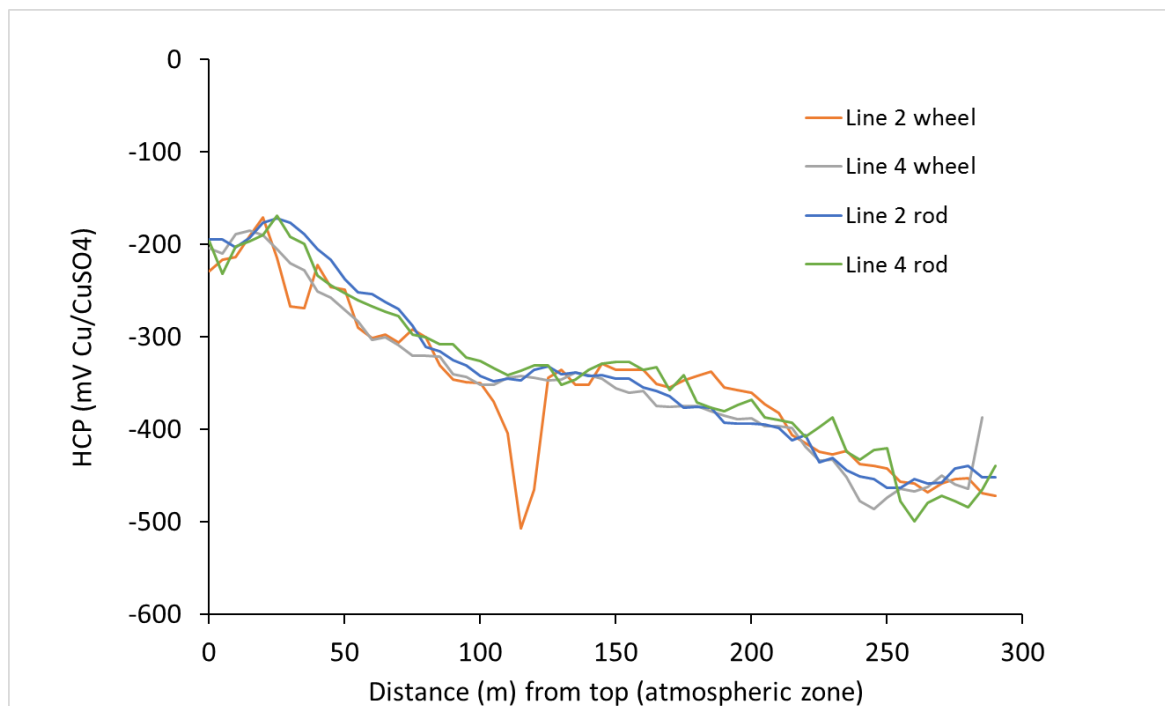


Figure 8: Comparison of half-cell potential (HCP) measured with the wheel and rod electrode along Line 2 and Line 4 on Beam B

Field station Sandnessjøen. Effect of cracks in concrete after 25 years - Data report
 March 2020, Trondheim, Norway

Beam E		Date:	16. Mars					
		Temperature	Laboratory					
		Cover	25 mm					
		Equipment	Wheel			Rod		
	Position (m)	Line 1 (Left side)	Line 2	Line 4	Line 5 (Right side)	Line 2	Line 4	
Atmospheric zone	0	-57	-126	-117	-55	-141	-55	
	5	-56	-141	-157	-64	-159	-64	
	10	-60	-147	-176	-68	-160	-68	
	15	-69	-146	-147	-68	-151	-68	
	20	-81	-147	-138	-75	-153	-75	
	25	-94	-148	-141	-89	-152	-89	
	30	-100	-133	-145	-105	-132	-105	
	35	-125	-128	-156	-120	-135	-120	
40	-143	-140	-165	-136	-139	-136		
45	-150	-156	-175	-152	-157	-152		
Tidal zone	50	-156	-163	-188	-171	-172	-171	
	55	-174	-173	-199	-192	-173	-192	
	60	-186	-192	-206	-208	-195	-208	
	65	-201	-207	-228	-219	-205	-219	
	70	-211	-220	-236	-222	-217	-222	
	75	-213	-228	-229	-231	-228	-231	
	80	-221	-232	-237	-247	-237	-247	
	85	-233	-242	-267	-246	-248	-246	
	90	-243	-251	-276	-256	-252	-256	
	95	-249	-268	-295	-264	-264	-264	
	100	-262	-275	-297	-282	-281	-282	
	105	-274	-294	-307	-288	-290	-288	
	110	-279	-314	-319	-290	-309	-290	
	115	-307	-314	-331	-294	-309	-294	
	120	-317	-321	-342	-307	-316	-307	
	125	-337	-325	-357	-330	-324	-330	
	130	-347	-346	-358	-339	-346	-339	
	135	-358	-353	-366	-351	-355	-351	
	140	-366	-353	-386	-363	-361	-363	
	145	-366	-366	-391	-387	-370	-387	
	150	-364	-370	-415	-394	-379	-394	
	155	-373	-380	-418	-397	-386	-397	
	160	-371	-372	-422	-430	-381	-430	
	165	-360	-365	-407	-429	-367	-429	
	170	-359	-362	-386	-405	-360	-405	
	175	-353	-367	-371	-409	-374	-409	
	180	-346	-364	-373	-396	-364	-396	
	185	-349	-350	-370	-388	-359	-388	
190	-350	-347	-364	-382	-358	-382		
195	-357	-351	-370	-378	-361	-378		
200	-359	-352	-374	-378	-355	-378		
205	-356	-353	-376	-365	-352	-365		
210	-366	-349	-374	-363	-345	-363		
215	-366	-350	-370	-361	-355	-361		
220	-366	-359	-373	-355	-360	-355		
225	-368	-355	-372	-367	-363	-367		
230	-368	-357	-370	-368	-374	-368		
235	-367	-356	-370	-364	-347	-364		
240	-368	-345	-367	-371	-355	-371		
245	-365	-349	-374	-383	-364	-383		
Submerged zone	250	-368	-349	-378	-380	-352	-380	
	255	-370	-348	-378	-381	-353	-381	
	260	-373	-351	-382	-385	-367	-385	
	265	-371	-350	-382	-387	-357	-387	
	270	-367	-349	-376	-387	-355	-387	
	275	-368	-349	-370	-376	-336	-376	
	280	-368	-329	-364	-376	-295	-376	
	285	-361	-312	-356	-370	-330	-370	
	290	-362	-327	-324	-363	-342	-363	
	295	-362	-342	-326	-352		-352	
300	-355	-348						
305		-354						

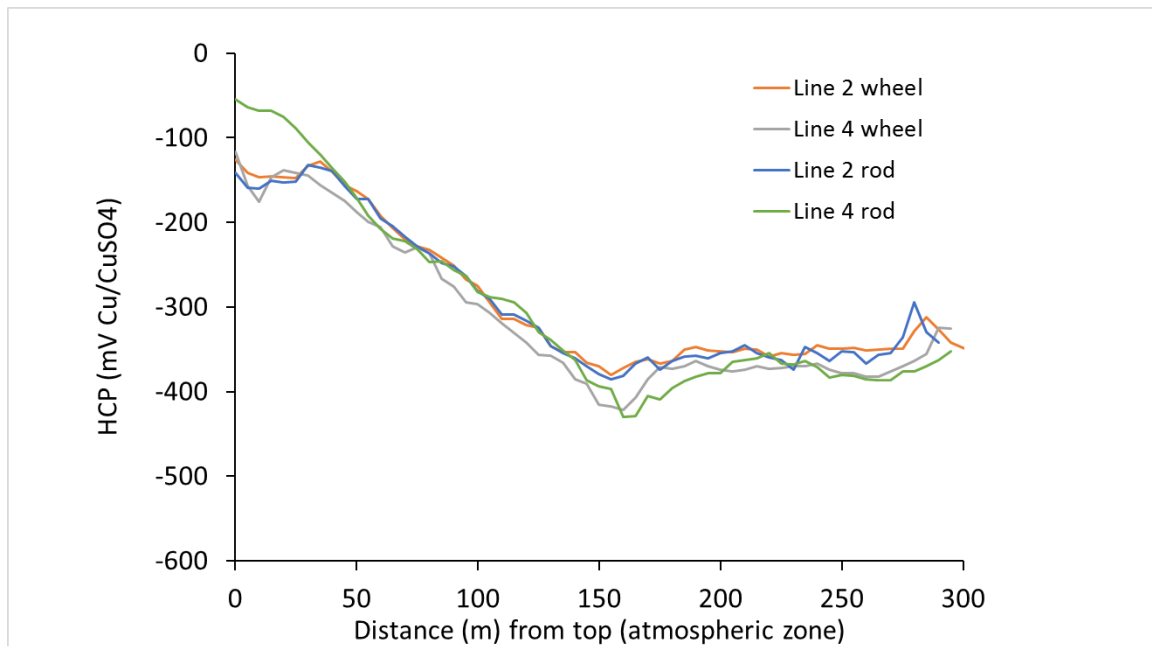


Figure 9: Comparison of half-cell potential (HCP) measured with the wheel and rod electrode along Line 2 and Line 4 on Beam E

Field station Sandnessjøen. Effect of cracks in concrete after 25 years - Data report
 March 2020, Trondheim, Norway

Beam F		Date:	16. Mars					
		Temperature	Laboratory					
		Cover	25 mm					
		Equipment	Wheel			Rod		
	Position (cm)	Line 1 (Left side)	Line 2	Line 4	Line 5 (Right side)	Line 2	Line 4	
Atmospheric zone	0		-199	-210	-179	-179	-220	
	5	-171	-223	-221	-192	-192	-229	
	10	-193	-241	-229	-185	-185	-242	
	15	-215	-248	-248	-185	-185	-264	
	20	-224	-249	-252	-200	-200	-245	
	25	-237	-251	-321	-202	-202	-263	
	30	-251	-250	-332	-217	-217	-268	
	35	-260	-254	-268	-237	-237	-248	
Tidal zone	40	-274	-237	-270	-238	-238	-260	
	45	-278	-241	-282	-252	-252	-262	
	50	-283	-242	-289	-253	-253	-283	
	55	-295	-250	-290	-259	-259	-279	
	60	-301	-261	-297	-266	-266	-298	
	65	-303	-269	-295	-271	-271	-301	
	70	-303	-288	-293	-275	-275	-290	
	75	-323	-303	-304	-290	-290	-311	
	80	-330	-316	-305	-295	-295	-305	
	85	-332	-326	-310	-293	-293	-329	
	90	-337	-335	-333	-306	-306	-346	
	95	-334	-340	-346	-318	-318	-347	
	100	-345	-352	-363	-331	-331	-321	
	105	-352	-353	-357	-341	-341	-369	
	110	-372	-360	-383	-345	-345	-387	
	115	-374	-365	-398	-351	-351	-368	
	120	-381	-361	-371	-358	-358	-358	
	125	-386	-364	-362	-374	-374	-347	
	130	-399	-382	-355	-373	-373	-347	
	135	-391	-395	-355	-391	-391	-346	
	140	-396	-402	-368	-392	-392	-361	
	145	-400	-402	-369	-396	-396	-359	
	150	-395	-390	-361	-399	-399	-347	
	155	-407	-398	-370	-400	-400	-358	
	160	-412	-401	-383	-400	-400	-365	
	165	-430	-417	-378	-409	-409	-369	
	170	-457	-436	-399	-418	-418	-389	
	175	-456	-440	-403	-421	-421	-384	
	180	-478	-457	-406	-431	-431	-387	
	185	-488	-465	-440	-433	-433	-411	
	190	-485	-472	-457	-440	-440	-393	
	195	-472	-472	-406	-445	-445	-383	
200	-465	-472	-409	-446	-446	-411		
205	-462	-449	-409	-444	-444	-376		
210	-458	-449	-397	-448	-448	-379		
215	-458	-448	-387	-444	-444	-393		
220	-441	-455	-411	-444	-444	-418		
225	-447	-458	-409	-436	-436	-377		
230	-446	-451	-405	-432	-432	-400		
235	-442	-441	-422	-432	-432	-403		
240	-432	-434	-421	-433	-433	-410		
245	-434	-431	-400	-433	-433	-421		
Submerged zone	250	-439	-433	-409	-431	-431	-403	
	255	-439	-431	-412	-430	-430	-405	
	260	-430	-435	-415	-432	-432	-420	
	265	-428	-436	-436	-428	-428	-421	
	270	-428	-433	-430	-422	-422	-413	
	275	-420	-417	-410	-421	-421	-405	
	280	-415	-398	-408	-421	-421	-422	
	285	-408	-391	-407	-419	-419	-399	
	290	-403	-376	-397	-420	-420	-430	
	295		-392	-410	-420	-420	-409	
300		-393		-426	-426	-408		
305		-393		-423	-423	-418		

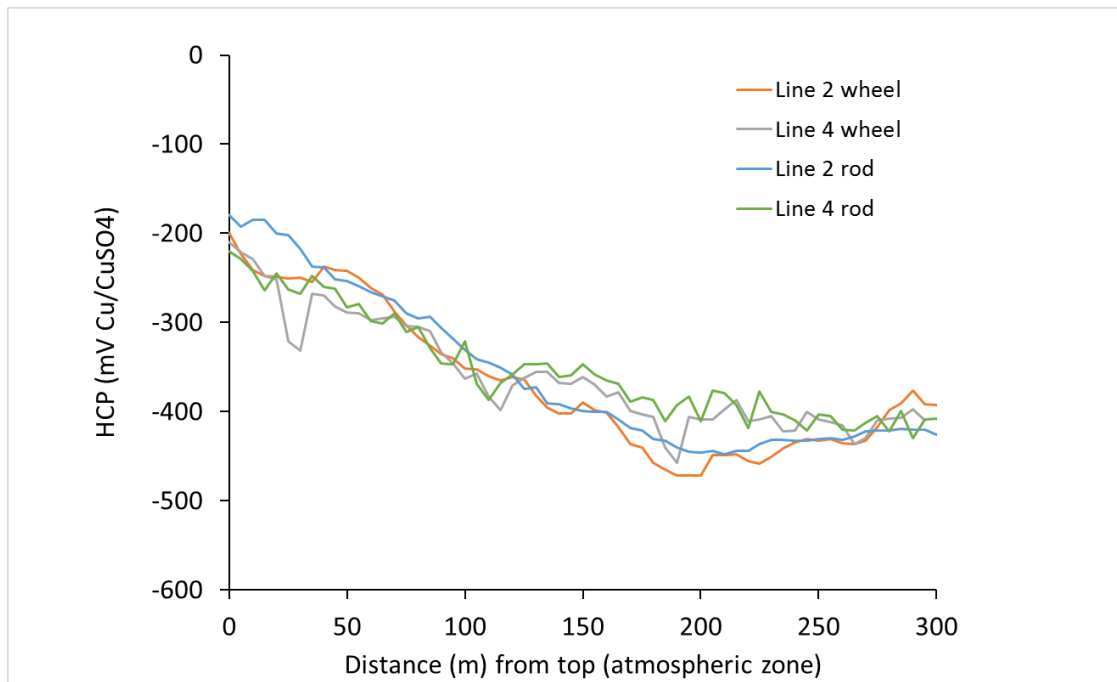


Figure 10: Comparison of half-cell potential (HCP) measured with the wheel and rod electrode along Line 2 and Line 4 on Beam F

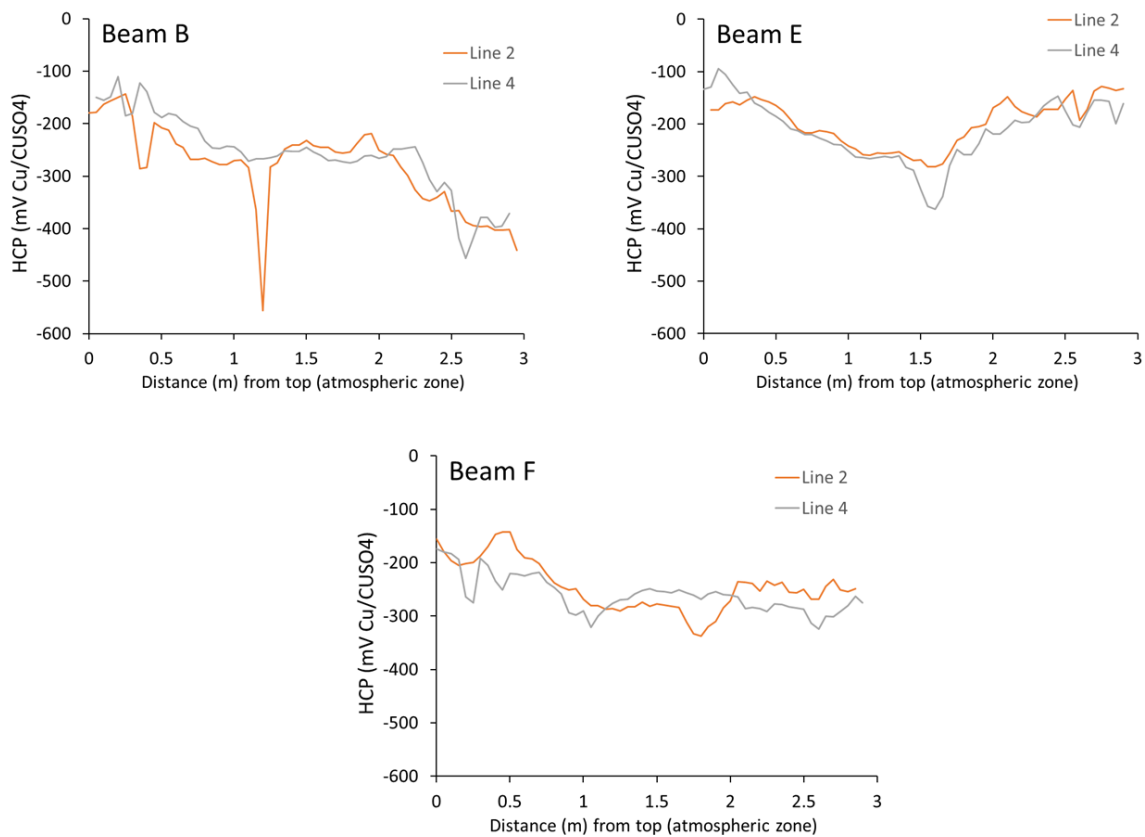


Figure 11: Half-cell potential (HCP) after 12 days storage at 5°C. Measurements performed at room temperature with a wheel electrode along Line 2 and Line 4 above the reinforcement on the top surface of the concrete beams

Appendix 5: Resistivity

Measurements performed by Solveig Myklebust, Ragnhild Moastuen and Tobias Danner

Table 1: Resistivity measurements performed with Wenner probe on Beam B

Date	16th March 2018		
Temperature	Laboratory (20 degrees)		
Equipment	Wenner probe		
Cover	25 mm		
Comments			
Beam B			
Position	0.4-0.8 m	1.3-1.7 m	2.2-2.6 m
Measurement	Atmospheric	Tidal	Submerged
1	34	28	19
2	32	23	20
3	43	22	14
4	24	21	18
5	34	23	22
6	31	20	17
7	30	25	20
8	36	28	20
9	26	25	17
10	33	28	14
11	37	27	22
12	36	25	23
13	35	25	17
14	35	27	17
15	34	23	26
16	39	25	24
17	41	26	21
18	43	31	23
19	30	31	17
20	35	29	18
Average	34.4	25.6	19.5
STDV	4.9	3.1	3.2

Table 2: Electrical resistivity measured at 5°C with two plate electrodes on concrete cores from Beam B

Core	Frequency	Phase angle(° Θ)	R (k Ω)	Electrical resistivity ρ (k Ω cm)
BAC	100 Hz	-1.4	14.6	69.0
	120 Hz	-1.5	14.5	68.6
	1 kHz	-2.2	13.8	65.5
	10 kHz	-0.4	13.8	62.7
BTC	100 Hz	-1.8	19.4	49.8
	120 Hz	-1.9	19.3	49.5
	1 kHz	-2.6	18.8	48.2
	10 kHz	-0.4	17.1	44.0
BSC	100 Hz	-2.3	7.6	35.9
	120 Hz	-2.4	7.5	35.6
	1 kHz	-3.1	7.1	33.5
	10 kHz	-4.4	6.5	30.7

Table 3: Resistivity measurements performed with Wenner probe on Beam E

Date	16th March 2018		
Temperature	Laboratory (20 degrees)		
Equipment	Wenner probe		
Cover	25 mm		
Comments			
Beam E			
Position	0.4-0.8 m	1.3-1.7 m	2.2-2.6 m
Measurement	Atmospheric	Tidal	Submerged
1	162	81	70
2	151	112	81
3	104	66	61
4	166	45	85
5	167	47	72
6	170	72	70
7	173	80	73
8	159	82	72
9	196	74	95
10	179	103	64
11	179	140	84
12	152	144	62
13	167	117	52
14	162	62	65
15	209	49	70
16	151	121	68
17	192	98	89
18	175	92	75
19	234	138	56
20	182	98	80
Average	171.5	91.1	72.2
STDV	25.9	30.7	11.0

Table 4: Electrical resistivity measured with two plate electrodes on concrete cores from Beam E

Core	Frequency	Phase angle($^{\circ}\Theta$)	R (k Ω)	Electrical resistivity ρ (k Ω cm)
EAC	100 Hz	-1.7	59.5	281.0
	120 Hz	-1.8	59.3	279.8
	1 kHz	-2.9	56.5	266.8
	10 kHz	-8.2	51.3	242.3
ETC	100 Hz	-2.3	52.7	135.1
	120 Hz	-2.4	52.4	134.4
	1 kHz	-3.5	49.3	126.4
	10 kHz	-7.6	44.1	113.0
ESC	100 Hz	1.9	32.0	151.0
	120 Hz	-2	31.9	150.5
	1 kHz	-3.3	29.9	141.4
	10 kHz	-7.1	26.9	127.0

Table 5: Resistivity measurements performed with Wenner probe on Beam F

Date	16th March 2018		
Temperature	Laboratory (20 degrees)		
Equipment	Wenner probe		
Cover	25 mm		
Comments			
Beam F			
Position	0.4-0.8 m	1.3-1.7 m	2.2-2.6 m
Measurement	Atmospheric	Tidal	Submerged
1	70	39	33
2	65	35	31
3	58	34	23
4	57	32	31
5	58	38	33
6	53	36	29
7	52	34	33
8	52	29	29
9	56	36	32
10	51	36	28
11	65	33	28
12	66	33	31
13	64	35	30
14	59	32	24
15	55	39	32
16	58	36	25
17	52	33	29
18	52	35	32
19	54	32	32
20	53	42	29
Average	57.5	35.0	29.7
STDV	5.7	3.0	3.0

Table 6: Electrical resistivity measured with two plate electrodes on concrete cores from Beam F

Core	Frequency	Phase angle($^{\circ}\Theta$)	R (k Ω)	Electrical resistivity ρ (k Ω cm)
FAC	100 Hz	-1.9	24.0	113.2
	120 Hz	-1.9	23.8	112.6
	1 kHz	-2.7	22.7	107.0
	10 kHz	-5.3	21.0	99.0
FTC	100 Hz	-2	31.6	81.0
	120 Hz	-2.1	31.4	80.1
	1 kHz	-2.8	29.8	76.5
	10 kHz	-5.4	27.4	70.1
FSC	100 Hz	-1.5	11.9	56.4
	120 Hz	-1.6	11.9	56.2
	1 kHz	-2.4	11.5	54.2
	10 kHz	-4.5	10.6	49.9

Appendix 6: Moisture – Raw data and comparison of different methods

Measurements performed by SINTEF Community. Calculation and presentation of results prepared by Mette Geiker and Tobias Danner.

A 6.1

Comparison of results on degree of capillary suction (DCS), suction porosity and macro porosity, based on initial submersion in water for 7 days and 21 days and subsequent with drying at 105°C.

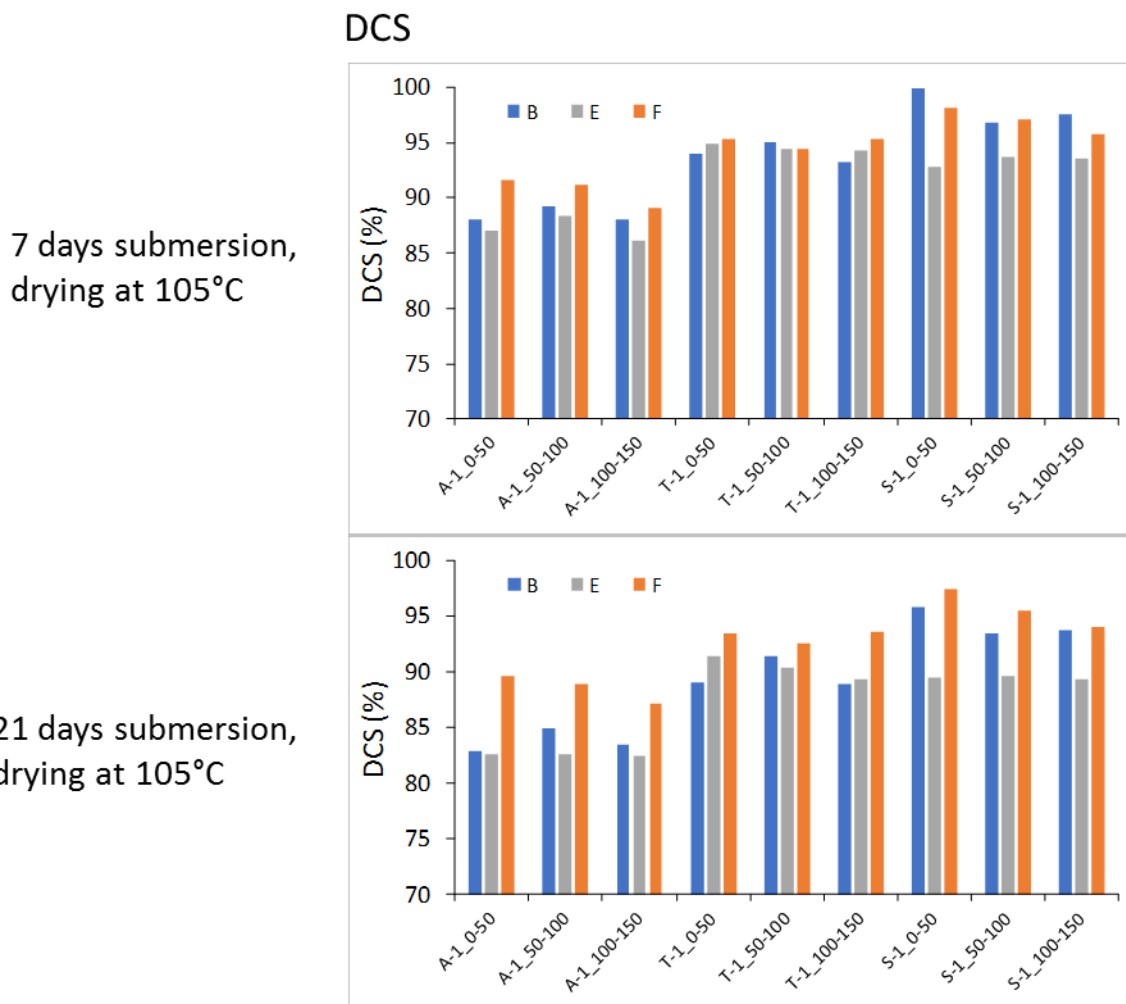
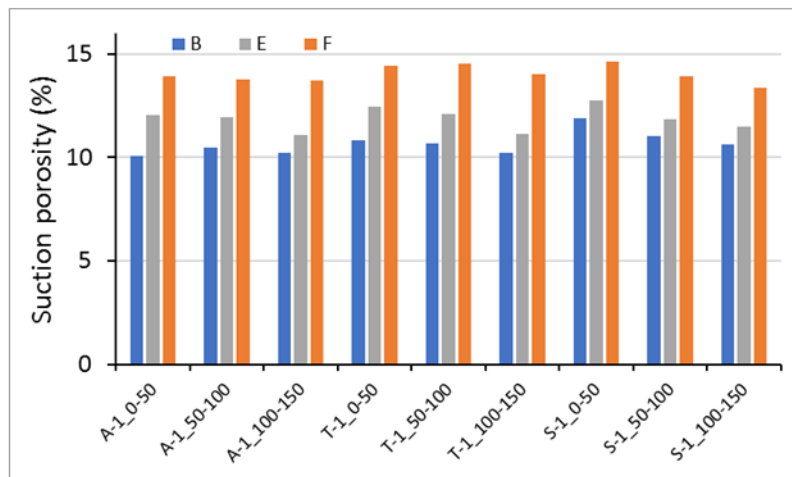


Figure 12: Comparison of DCS based on initial submersion in water for 7 and 21 days and drying at 105°C

Suction porosity

7 days submersion,
 drying at 105°C



21 days submersion,
 drying at 105°C

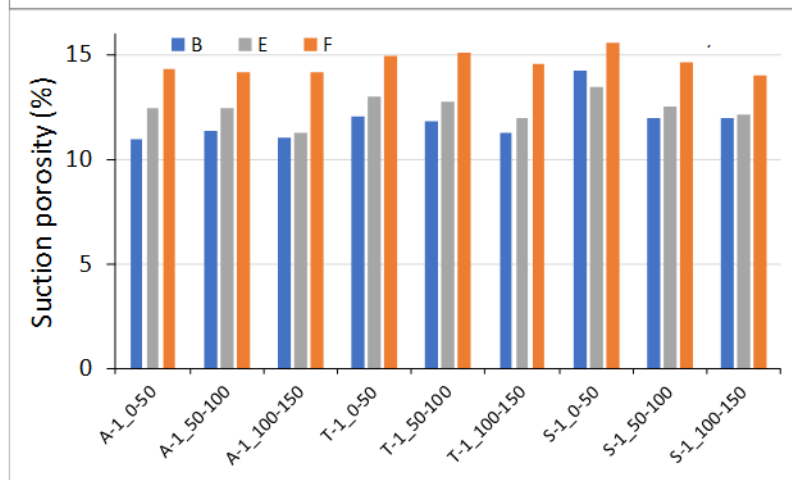
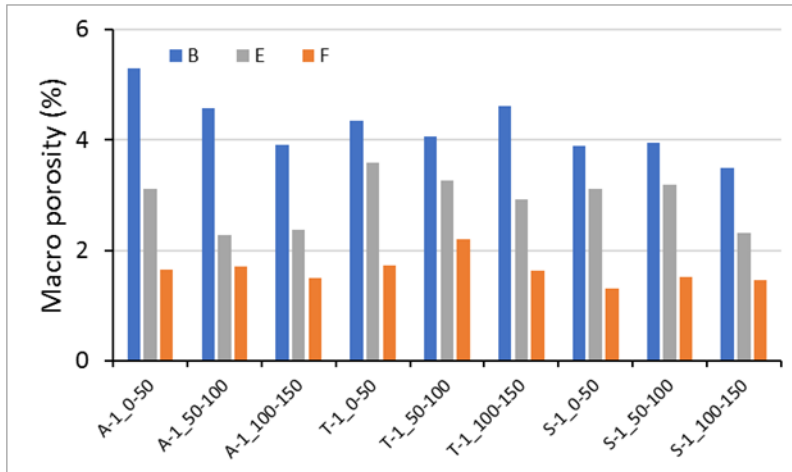


Figure 13: Comparison of suction porosity based on initial submersion in water for 7 and 21 days and drying at 105°C

Macro porosity

7 days submersion,
drying at 105°C



21 days submersion,
drying at 105°C

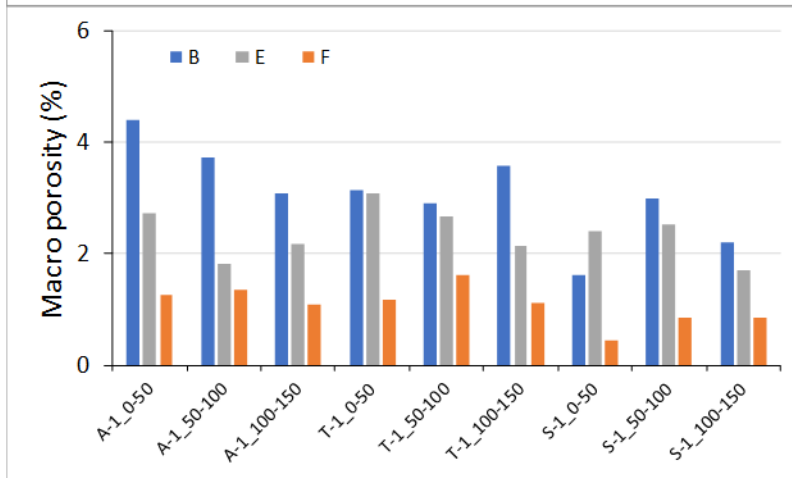


Figure 14: Comparison of macro porosity based on initial submersion in water for 7 and 21 days and drying at 105°C

A 6.2

Comparison of results on degree of capillary suction (DCS), suction porosity and macro porosity, based on drying at 50 and 105°C with initial submersion in water for 21 days

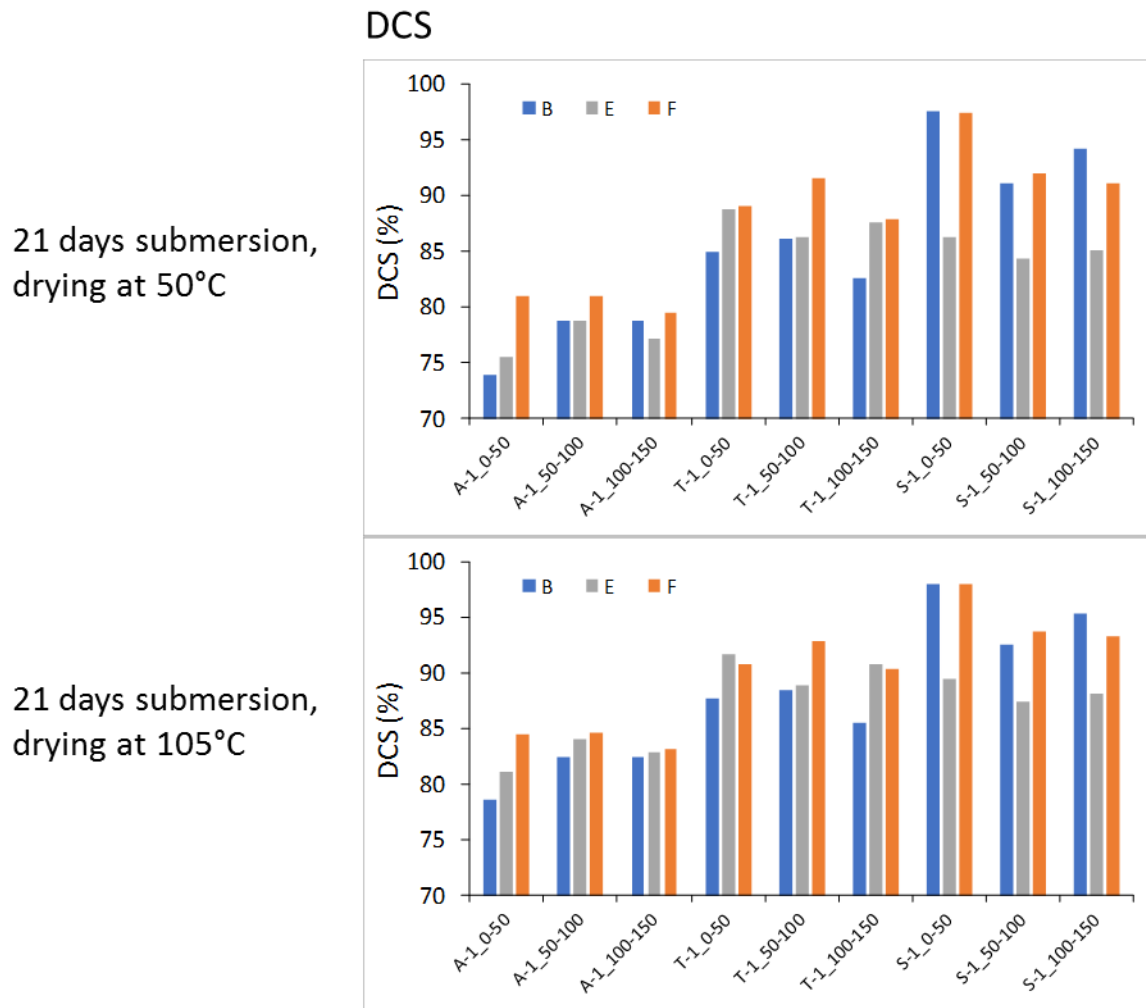
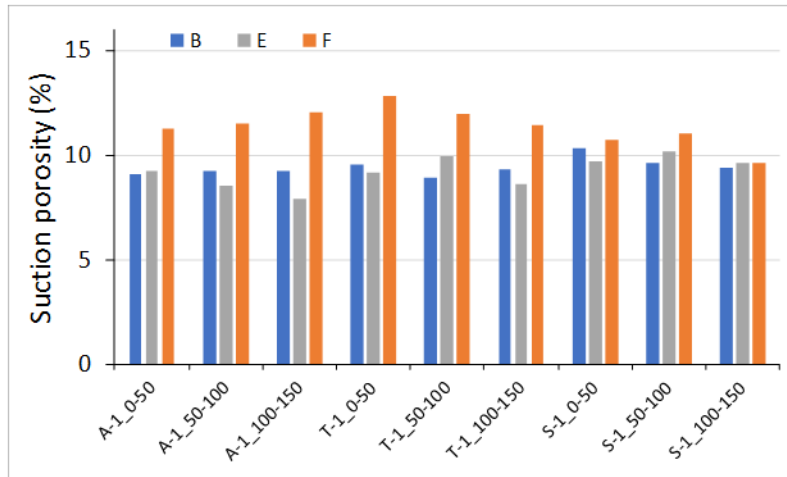


Figure 15: Comparison of DCS for samples dried at 50 and 105°C after submersion in water for 21 days

Suction porosity

21 days submersion,
drying at 50°C



21 days submersion,
drying at 105°C

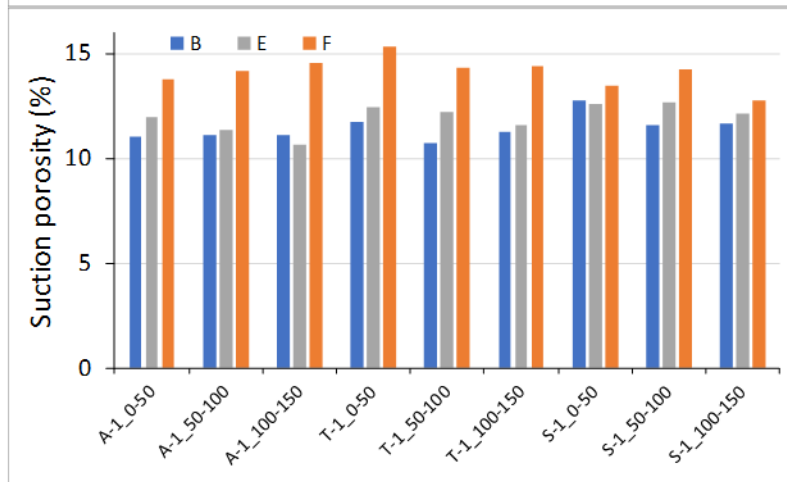


Figure 16: Comparison of suction porosity for samples dried at 50 and 105°C after submersion in water for 21 days

A 6.3

Raw data and results for samples initially submerged for 7 and 21 days in water and dried at 105°C

Raw data:

		BAM-1_0-50	BAM-1_50-100	BAM-1_100-150	BTM-1_0-50	BTM-1_50-100	BTM-1_100-150	BSM-1_0-50	BSM-1_50-100	BSM-1_100-150
Utpakking/Splitting	g0	430.26	516.86	364.75	540.51	263.21	470.1	506.36	468.1	513.28
1 uke vannsug	g6	432.52	519.39	366.66	542.07	263.84	471.54	506.37	468.81	513.88
3 uker vannsug	g6a	433.7	520.57	367.51	543.53	264.34	472.58	507.62	469.63	514.87
1 uke tørking (105 °C)	g1	413.63	495.88	350.74	516.09	251.33	450.37	477.52	446.13	489.46
1 uke vannsug (luft)	g2	432.05	518.72	366.27	540.77	263.07	470.55	502.76	467.74	512.11
(vann)	g3	249.08	300.29	214.24	313.16	153	272.67	290.75	271.4	298.99
3 uker vannsug	g5	433.32	519.88	367.05	542.55	263.84	471.83	503.89	468.92	513.23
Trykkmetting i 2 døgn (luft)	g4	441.73	528.72	372.2	550.64	267.54	479.67	511.02	475.49	519.55
1 uke tørking (105 °C)	g7	412.48	494.37	349.67	514.25	250.5	449.01	475.5	444.74	487.83
		EAM-1_0-60	EAM-1_60-100	EAM-1_100-150	ETM-1_0-50	ETM-1_50-100	ETM-1_100-150	ESM-1_0-50	ESM-1_50-100	ESM-1_100-150
Utpakking/Splitting	g0	577.66	221.97	558.19	463.94	433.85	481.72	370.71	491.75	380.96
1 uke vannsug	g6	581.38	223.21	561.61	465.20	435.09	483.02	372.15	493.29	382.13
3 uker vannsug	g6a	582.93	223.95	562.71	466.10	436.06	484.27	372.91	494.41	383.00
1 uke tørking (105 °C)	g1	552.74	212.58	536.93	440.94	413.03	460.49	352.11	468.91	363.99
1 uke vannsug (luft)	g2	581.98	223.53	562.25	465.12	434.94	482.72	371.80	493.07	382.03
(vann)	g3	339.67	131.95	333.59	270.75	253.67	283.37	217.27	289.17	224.95
3 uker vannsug	g5	583.19	223.97	563.24	466.26	435.81	483.75	372.78	494.12	382.82
Trykkmetting i 2 døgn (luft)	g4	589.54	225.62	567.65	472.09	440.87	488.56	376.62	499.58	385.66
1 uke tørking (105 °C)	g7	552.77	212.59	536.87	440.82	412.92	460.20	351.98	468.73	363.83
		FAM-1_0-50	FAM-1_50-110	FAM-1_110-150	FTM-1_0-50	FTM-1_50-100	FTM-1_100-150	FSM-1_0-40	FSM-1_40-100	FSM-1_100-150
Utpakking/Splitting	g0	542.28	553.85	445.41	286.44	398.61	518.64	277.35	367.94	479.63
1 uke vannsug	g6	544.93	556.63	448.18	287.26	400.00	520.07	277.68	368.59	480.79
3 uker vannsug	g6a	545.62	557.47	448.77	287.61	400.50	520.66	277.81	368.94	481.26
1 uke tørking (105 °C)	g1	513.36	524.91	422.77	269.89	375.20	489.30	260.10	346.73	453.78
1 uke vannsug (luft)	g2	544.72	556.64	448.01	286.97	399.51	519.52	276.80	367.91	480.09
(vann)	g3	319.70	326.35	263.90	168.57	232.18	304.09	162.80	215.89	283.16
3 uker vannsug	g5	545.85	557.81	448.98	287.65	400.61	520.49	277.32	368.74	480.46
Trykkmetting i 2 døgn (luft)	g4	548.43	560.56	450.76	289.01	403.20	523.05	278.30	370.22	482.96
1 uke tørking (105 °C)	g7	513.27	524.86	422.66	269.72	375.06	489.12	259.84	346.50	453.62

The following equations were used for calculation of the results based on 7 day submersion and drying at 105°C:

$$Volume (V) = \frac{g2 - g3}{1}$$

$$Suction porosity = \frac{g6 - g1}{V}$$

$$Macro porosity = \frac{g4 - g6}{V}$$

$$DCS = \frac{g0 - g1}{g6 - g1}$$

The following equations were used for calculation of the results based on 21 day initial submersion and drying at 105°C. In the equations g_6 was replaced by g_{6a}

$$\text{Volume } (V) = \frac{g_2 - g_3}{1}$$

$$\text{Suction porosity} = \frac{g_{6a} - g_1}{V}$$

$$\text{Macro porosity} = \frac{g_4 - g_{6a}}{V}$$

$$\text{DCS} = \frac{g_0 - g_1}{g_{6a} - g_1}$$

Results based on submersion for 21 days:

	BAM-1_0-50	BAM-1_50-100	BAM-1_100-150	BTM-1_0-50	BTM-1_50-100	BTM-1_100-150	BSM-1_0-50	BSM-1_50-100	BSM-1_100-150
Prøvestykkets volum - V (cm ³)	183.0	218.4	152.0	227.6	110.1	197.9	212.0	196.3	213.1
Tørrdensitet - ρ_t (kg/m ³)	2260.6	2270.2	2307.0	2267.4	2283.4	2276.0	2252.3	2272.2	2296.6
Densitet faststoff - ρ_s (kg/m ³)	2671	2672	2686	2673	2678	2672	2675	2672	2674
Sugmettet densitet ρ_s (kg/m ³)	2370.3	2383.2	2417.4	2388.0	2401.6	2388.2	2394.3	2391.9	2415.9
Sugporøsitet - p_s (%)	10.97%	11.30%	11.03%	12.06%	11.82%	11.22%	14.20%	11.97%	11.92%
Makroporøsitet - p_m (%)	4.4 %	3.7 %	3.1 %	3.1 %	2.9 %	3.6 %	1.6 %	3.0 %	2.2 %
Totalporøsitet - p_t (%)	15.4 %	15.0 %	14.1 %	15.2 %	14.7 %	14.8 %	15.8 %	15.0 %	14.1 %
PF-verdi	28.6 %	24.8 %	21.9 %	20.6 %	19.7 %	24.2 %	10.1 %	20.0 %	15.6 %
PF-verdi	28.6 %	24.8 %	21.9 %	20.6 %	19.7 %	24.2 %	10.1 %	20.0 %	15.6 %
Kapillær vannmetningsgrad - DCS	82.9 %	85.0 %	83.5 %	89.0 %	91.3 %	88.8 %	95.8 %	93.5 %	93.7 %
Total vannmetningsgrad - DS	59.2 %	63.9 %	65.3 %	70.7 %	73.3 %	67.3 %	86.1 %	74.8 %	79.2 %

	EAM-1_0-60	EAM-1_60-100	EAM-1_100-150	ETM-1_0-50	ETM-1_50-100	ETM-1_100-150	ESM-1_0-50	ESM-1_50-100	ESM-1_100-150
Prøvestykkets volum - V (cm ³)	242.3	91.6	228.7	194.4	181.3	199.4	154.5	203.9	157.1
Tørrdensitet - ρ_t (kg/m ³)	2281.1	2321.2	2348.2	2268.6	2278.5	2310.0	2278.6	2299.7	2317.2
Densitet faststoff - ρ_s (kg/m ³)	2690	2707	2713	2702	2692	2689	2708	2707	2688
Sugmettet densitet ρ_s (kg/m ³)	2405.7	2445.4	2460.9	2398.0	2405.6	2429.2	2413.2	2424.8	2438.2
Sugporøsitet - p_s (%)	12.46%	12.42%	11.27%	12.94%	12.70%	11.93%	13.46%	12.51%	12.10%
Makroporøsitet - p_m (%)	2.7 %	1.8 %	2.2 %	3.1 %	2.7 %	2.2 %	2.4 %	2.5 %	1.7 %
Totalporøsitet - p_t (%)	15.2 %	14.2 %	13.4 %	16.0 %	15.4 %	14.1 %	15.9 %	15.0 %	13.8 %
PF-verdi	18.0 %	12.8 %	16.1 %	19.2 %	17.3 %	15.3 %	15.1 %	16.9 %	12.3 %
PF-verdi	18.0 %	12.8 %	16.1 %	19.2 %	17.3 %	15.3 %	15.1 %	16.9 %	12.3 %
Kapillær vannmetningsgrad - DCS	82.5 %	82.6 %	82.5 %	91.4 %	90.4 %	89.3 %	89.4 %	89.6 %	89.3 %
Total vannmetningsgrad - DS	67.7 %	72.0 %	69.2 %	73.8 %	74.8 %	75.6 %	75.9 %	74.5 %	78.3 %

	FAM-1_0-50	FAM-1_50-110	FAM-1_110-150	FTM-1_0-50	FTM-1_50-100	FTM-1_100-150	FSM-1_0-40	FSM-1_40-100	FSM-1_100-150
Prøvestykkets volum - V (cm ³)	225.0	230.3	184.1	118.4	167.3	215.4	114.0	152.0	196.9
Tørrdensitet - ρ_t (kg/m ³)	2281.4	2279.3	2296.3	2279.5	2242.3	2271.3	2281.6	2280.8	2304.3
Densitet faststoff - ρ_s (kg/m ³)	2703	2697	2708	2718	2693	2693	2715	2698	2705
Sugmettet densitet ρ_s (kg/m ³)	2424.8	2420.7	2437.5	2429.1	2393.5	2416.8	2436.9	2426.9	2443.8
Sugporøsitet - p_s (%)	14.34%	14.14%	14.12%	14.97%	15.12%	14.56%	15.54%	14.61%	13.95%
Makroporøsitet - p_m (%)	1.2 %	1.3 %	1.1 %	1.2 %	1.6 %	1.1 %	0.4 %	0.8 %	0.9 %
Totalporøsitet - p_t (%)	15.6 %	15.5 %	15.2 %	16.1 %	16.7 %	15.7 %	16.0 %	15.5 %	14.8 %
PF-verdi	8.0 %	8.7 %	7.1 %	7.3 %	9.6 %	7.1 %	2.7 %	5.4 %	5.8 %
PF-verdi	8.0 %	8.7 %	7.1 %	7.3 %	9.6 %	7.1 %	2.7 %	5.4 %	5.8 %
Kapillær vannmetningsgrad - DCS	89.6 %	88.9 %	87.1 %	93.4 %	92.5 %	93.6 %	97.4 %	95.5 %	94.1 %
Total vannmetningsgrad - DS	82.5 %	81.2 %	80.9 %	86.6 %	83.6 %	86.9 %	94.8 %	90.3 %	88.6 %

Results based on submersion for 7 days:

	BAM-1_0-50	BAM-1_50-100	BAM-1_100-150	BTM-1_0-50	BTM-1_50-100	BTM-1_100-150	BSM-1_0-50	BSM-1_50-100	BSM-1_100-150
Prøvestykkets volum - V (cm ³)	183.0	218.4	152.0	227.6	110.1	197.9	212.0	196.3	213.1
Tørrdensitet - pt (kg/m ³)	2260.6	2270.2	2307.0	2267.4	2283.4	2276.0	2252.3	2272.2	2296.6
Densitet faststoff - rfs (kg/m ³)	2671	2672	2686	2673	2678	2672	2675	2672	2674
Sugmettet densitet ps (kg/m ³)	2361.3	2374.8	2409.2	2375.9	2390.0	2378.0	2371.4	2382.3	2402.9
Sugporøsitet - ps (%)	10.32%	10.76%	10.47%	11.41%	11.37%	10.70%	13.61%	11.55%	11.46%
Makroporøsitet - pm (%)	5.0 %	4.3 %	3.6 %	3.8 %	3.4 %	4.1 %	2.2 %	3.4 %	2.7 %
Totalporøsitet - pt (%)	15.4 %	15.0 %	14.1 %	15.2 %	14.7 %	14.8 %	15.8 %	15.0 %	14.1 %
PF-verdi	32.8 %	28.4 %	25.8 %	24.8 %	22.8 %	27.7 %	13.9 %	22.8 %	18.8 %
Kapillær vannmetningsgrad - DCS	88.0 %	89.2 %	88.0 %	94.0 %	95.0 %	93.2 %	100.0 %	96.9 %	97.5 %
Total vannmetningsgrad - DS	59.2 %	63.9 %	65.3 %	70.7 %	73.3 %	67.3 %	86.1 %	74.8 %	79.2 %

	EAM-1_0-60	EAM-1_60-100	EAM-1_100-150	ETM-1_0-50	ETM-1_50-100	ETM-1_100-150	ESM-1_0-50	ESM-1_50-100	ESM-1_100-150
Prøvestykkets volum - V (cm ³)	242.3	91.6	228.7	194.4	181.3	199.4	154.5	203.9	157.1
Tørrdensitet - pt (kg/m ³)	2281.1	2321.2	2348.2	2268.6	2278.5	2310.0	2278.6	2299.7	2317.2
Densitet faststoff - rfs (kg/m ³)	2690	2707	2713	2702	2692	2689	2708	2707	2688
Sugmettet densitet ps (kg/m ³)	2401.8	2440.8	2458.9	2393.0	2399.4	2421.5	2406.0	2418.2	2432.1
Sugporøsitet - ps (%)	11.82%	11.61%	10.79%	12.48%	12.17%	11.30%	12.97%	11.96%	11.55%
Makroporøsitet - pm (%)	3.4 %	2.6 %	2.6 %	3.5 %	3.2 %	2.8 %	2.9 %	3.1 %	2.2 %
Totalporøsitet - pt (%)	15.2 %	14.2 %	13.4 %	16.0 %	15.4 %	14.1 %	15.9 %	15.0 %	13.8 %
PF-verdi	22.2 %	18.5 %	19.7 %	22.1 %	20.8 %	19.7 %	18.2 %	20.5 %	16.3 %
Kapillær vannmetningsgrad - DCS	87.0 %	88.3 %	86.1 %	94.8 %	94.4 %	94.2 %	92.8 %	93.7 %	93.6 %
Total vannmetningsgrad - DS	67.7 %	72.0 %	69.2 %	73.8 %	74.8 %	75.6 %	75.9 %	74.5 %	78.3 %

	FAM-1_0-50	FAM-1_50-110	FAM-1_110-150	FTM-1_0-50	FTM-1_50-100	FTM-1_100-150	FSM-1_0-40	FSM-1_40-100	FSM-1_100-150
Prøvestykkets volum - V (cm ³)	225.0	230.3	184.1	118.4	167.3	215.4	114.0	152.0	196.9
Tørrdensitet - pt (kg/m ³)	2281.4	2279.3	2296.3	2279.5	2242.3	2271.3	2281.6	2280.8	2304.3
Densitet faststoff - rfs (kg/m ³)	2703	2697	2708	2718	2693	2693	2715	2698	2705
Sugmettet densitet ps (kg/m ³)	2420.8	2417.1	2433.4	2423.7	2387.6	2411.5	2428.1	2420.1	2437.9
Sugporøsitet - ps (%)	14.03%	13.77%	13.80%	14.67%	14.82%	14.28%	15.42%	14.38%	13.72%
Makroporøsitet - pm (%)	1.6 %	1.7 %	1.4 %	1.5 %	1.9 %	1.4 %	0.5 %	1.1 %	1.1 %
Totalporøsitet - pt (%)	15.6 %	15.5 %	15.2 %	16.1 %	16.7 %	15.7 %	16.0 %	15.5 %	14.8 %
PF-verdi	10.0 %	11.0 %	9.2 %	9.2 %	11.4 %	8.8 %	3.4 %	6.9 %	7.4 %
Kapillær vannmetningsgrad - DCS	91.6 %	91.2 %	89.1 %	95.3 %	94.4 %	95.4 %	98.1 %	97.0 %	95.7 %
Total vannmetningsgrad - DS	82.5 %	81.2 %	80.9 %	86.6 %	83.6 %	86.9 %	94.8 %	90.3 %	88.6 %

A 6.4

Raw data for samples dried at 50 and 105°C after initial submersion for 7 and 21 days in water

Raw data:

		BAM-2_0-50	BAM-2_50-100	BAM-2_100-150	BTM-2_0-50	BTM-2_50-100	BTM-2_100-150	BSM-2_0-50	BSM-2_50-100	BSM-2_100-150
Utpakking/Splitting	g0	178.27	180.23	180.23	192.08	169.35	250.32	243.58	188.55	177.69
3 uker vannsug (luft)	g1	180.06	181.71	181.71	193.25	170.24	252.06	243.83	189.23	178.09
(vann)	g2	103.97	105.94	105.94	112.00	98.62	144.97	143.83	110.04	104.74
3 uker tørking (50°C)	g3	173.19	174.73	174.73	185.47	163.85	242.10	233.54	181.61	171.18
3 uker tørking (100°C)	g4	171.69	173.30	173.30	183.74	162.57	239.99	231.06	180.07	169.53
		EAM-2_0-60	EAM-2_60-100	EAM-2_100-150	ETM-2_0-50	ETM-2_50-100	ETM-2_100-150	ESM-2_0-50	ESM-2_50-100	ESM-2_100-150
Utpakking/Splitting	g0	232.76	215.78	215.78	183.37	187.91	250.96	294.14	126.99	216.32
3 uker vannsug (luft)	g1	234.94	217.40	217.40	184.15	188.99	252.08	295.79	127.83	217.59
(vann)	g2	138.27	127.88	127.88	108.62	109.75	147.67	171.04	74.93	128.98
3 uker tørking (50°C)	g3	226.03	209.77	210.32	177.27	181.15	243.09	283.73	122.46	209.06
3 uker tørking (105°C)	g4	223.38	207.23	207.92	174.78	179.32	240.01	280.10	121.15	206.85
		FAM-2_0-50	FAM-2_50-110	FAM-2_110-150	FTM-2_0-50	FTM-2_50-100	FTM-2_100-150	FSM-2_0-40	FSM-2_40-100	FSM-2_100-150
Utpakking/Splitting	g0	169.85	213.07	142.83	167.7	154.43	247.97	195.09	422.08	223.26
3 uker vannsug (luft)	g1	171.36	215	144.29	168.69	155.08	249.41	195.31	423.63	224.05
(vann)	g2	100.79	126.19	84.69	98.62	91.18	146.04	116.14	248.65	132.37
3 uker tørking (50°C)	g3	163.437	204.825	137.138	159.712	147.433	237.58	186.848	404.312	215.211
3 uker tørking (105°C)	g4	161.641	202.466	135.616	157.962	145.955	234.549	184.641	398.709	212.399

The following equations were applied:

$$Volume (V) = \frac{g1 - g2}{1}$$

$$Suction porosity (50oC) = \frac{g1 - g3}{V}$$

$$Suction porosity (105oC) = \frac{g1 - g4}{V}$$

$$DCS (50oC) = \frac{g0 - g3}{g1 - g3}$$

$$DCS (105oC) = \frac{g0 - g4}{g1 - g4}$$

Field station Sandnessjøen. Effect of cracks in concrete after 25 years - Data report
March 2020, Trondheim, Norway

Results:

	BAM-1_0-50	BAM-1_50-100	BAM-1_100-150	BTM-1_0-50	BTM-1_50-100	BTM-1_100-150	BSM-1_0-50	BSM-1_50-100	BSM-1_100-150
Prøvestykkets volum - V (cm ³)	76.1	75.8	75.8	81.3	71.6	107.1	100.0	79.2	73.4
Tørrdensitet - ρt (kg/m ³)	2256.4	2287.2	2287.2	2261.5	2269.9	2241.0	2310.6	2273.9	2311.3
Sugmettet densitet ps (kg/m ³)	2366.4	2398.2	2398.2	2378.5	2377.0	2353.7	2438.3	2389.6	2427.9
Sugporøsitet - ps (%) 50oC	9.03%	9.21%	9.21%	9.57%	8.92%	9.30%	10.29%	9.63%	9.42%
Sugporøsitet - ps (%) 105oC	11.00%	11.10%	11.10%	11.70%	10.71%	11.27%	12.77%	11.56%	11.66%
Kapillær vannmetningsgrad - DCS, 50oC	74.0 %	78.8 %	78.8 %	85.0 %	86.1 %	82.5 %	97.6 %	91.1 %	94.2 %

	EAM-1_0-60	EAM-1_60-100	EAM-1_100-150	ETM-1_0-50	ETM-1_50-100	ETM-1_100-150	ESM-1_0-50	ESM-1_50-100	ESM-1_100-150
Prøvestykkets volum - V (cm ³)	96.7	89.5	89.5	75.5	79.2	104.4	124.8	52.9	88.6
Tørrdensitet - ρt (kg/m ³)	2310.7	2314.9	2322.6	2314.0	2262.9	2298.7	2245.3	2290.1	2334.4
Sugmettet densitet ps (kg/m ³)	2430.3	2428.5	2428.5	2438.1	2324.0	1810.1	2020.7	2416.4	2455.6
Sugporøsitet - ps (%) 50oC	9.22%	8.53%	7.90%	9.12%	9.89%	8.61%	9.67%	10.15%	9.62%
Sugporøsitet - ps (%) 105oC	11.96%	11.36%	10.60%	12.41%	12.21%	11.56%	12.57%	12.63%	12.12%
Kapillær vannmetningsgrad - DCS, 50oC	75.5 %	78.8 %	77.1 %	88.7 %	86.2 %	87.5 %	86.3 %	84.3 %	85.1 %
Kapillær vannmetningsgrad - DCS, 105oC	81.1 %	84.1 %	82.9 %	91.7 %	88.8 %	90.7 %	89.5 %	87.4 %	88.2 %

	FAM-1_0-50	FAM-1_50-110	FAM-1_110-150	FTM-1_0-50	FTM-1_50-100	FTM-1_100-150	FSM-1_0-40	FSM-1_40-100	FSM-1_100-150
Prøvestykkets volum - V (cm ³)	70.6	88.8	59.6	70.1	63.9	103.4	79.2	175.0	91.7
Tørrdensitet - ρt (kg/m ³)	2290.5	2279.8	2275.4	2254.3	2284.1	2269.0	2332.2	2278.6	2316.7
Sugmettet densitet ps (kg/m ³)	2428.2	2420.9	2421.0	2407.4	2426.9	2412.8	2467.0	2421.0	2443.8
Sugporøsitet - ps (%) 50oC	11.23%	11.46%	12.00%	12.81%	11.97%	11.44%	10.69%	11.04%	9.64%
Sugporøsitet - ps (%) 105oC	13.77%	14.11%	14.55%	15.31%	14.28%	14.38%	13.48%	14.24%	12.71%
Kapillær vannmetningsgrad - DCS, 50oC	80.9 %	81.0 %	79.6 %	89.0 %	91.5 %	87.8 %	97.4 %	92.0 %	91.1 %
Kapillær vannmetningsgrad - DCS, 105oC	84.5 %	84.6 %	83.2 %	90.8 %	92.9 %	90.3 %	97.9 %	93.8 %	93.2 %

A 6.5

Relative humidity

Results:


Samples, Beam B	RH (%)	Samples, Beam E	RH (%)	Samples, Beam F	RH (%)
BAM-1_0-50	≤ 84,5	EAM-1_0-60	82,5	FAM-1_0-50	≤ 83,5
BAM-1_50-100	≤ 79,5	EAM-1_60-100	81,5	FAM-1_50-110	≤ 84
BAM-1_100-150	90,5	EAM-1_100-150	84,5	FAM-1_110-150	≤ 83
BTM-1_0-50	≤ 86,5	ETM-1_0-50	90	FTM-1_0-50	83
BTM-1_50-100	≤ 91	ETM-1_50-100	90	FTM-1_50-100	≤ 87,5
BTM-1_100-150	≤ 88	ETM-1_100-150	90	FTM-1_100-150	≤ 86
BSM-1_0-50	97,5	ESM-1_0-50	92,5	FSM-1_0-40	94
BSM-1_50-100	95	ESM-1_50-100	91	FSM-1_40-100	91
BSM-1_100-150	97	ESM-1_100-150	87,5	FSM-1_100-150	89

"≤": RH was decreasing from first measurements (see method description for further information)

A 6.6

Moisture results based on the standard NPRA calculation procedure

Core BAM:




Statens vegvesen

Region Øst
Sentrallaboratoriet / Regionlaboratoriet
 Arbeidsskjema for laboratorieanalyser

210.426-3/4 Kapillær vannmetningsgrad og porøsitet, PF-metoden							Side 1 av 2
Oppdragsnr.	Utført dato				Signatur		
Prosjekt: E39	Prøve er merket: BAM				25 år		
	Prøvens alder:						
Start forsøk:	dato:	tid (ttmm):					
Dato	Kl.	Vekt (g) etter:	Prøvestykket merket				
			BAM-1_0-50	BAM-1_50-100	BAM-1_100-150		
09.04.2018	09:00	Utpakking/Splitting - g_0	430,26	516,86	364,75		
		1 uke vannsug - g_6	432,52	519,39	366,66		
07.05.2018		1 uke tørking (105 °C) - g_1	413,63	495,88	350,74		
14.05.2018		1 uke vannsug	432,05	518,72	366,27		
14.05.2018							
14.05.2018		i vann - g_3	249,08	300,29	214,24		
30.05.2018		Trykkmetting i 2 døgn (luft) - g_4	441,73	528,72	372,2		
06.06.2018		1 uke tørking (105 °C) - g_7	412,48	494,37	349,67		
Målt		sidekant a / diameter d (mm)					
		sidekant b (mm)					
		høyde (mm)					
For utregninger, se formler på side 2							
Prøvestykkets volum - V (cm ³)			183,0	218,4	152,0		
Tørredensitet - ρ_t (kg/m ³)			2260,6	2270,2	2307,0		
Densitet faststoff - ρ_s (kg/m ³)			2671	2672	2686		
Sugmettet densitet ρ_s (kg/m ³)			2361,3	2374,8	2409,2		
Sugporøsitet - p_s (%)			10,07 %	10,46 %	10,22 %		
Makroporøsitet - p_m (%)			5,3 %	4,6 %	3,9 %		
Totalporøsitet - p_t (%)			15,4 %	15,0 %	14,1 %		
PF-verdi			34,4 %	30,5 %	27,6 %		
Kapillær vannmetningsgrad - DCS			88,0 %	89,2 %	88,0 %		
Total vannmetningsgrad - DS			59,2 %	63,9 %	65,3 %		

Core BTM:



Statens vegvesen

Region Øst
Sentrallaboratoriet / Regionlaboratoriet
 Arbeidsskjema for laboratorieanalyser

210.426-3/4 Kapillær vannmetningsgrad og porøsitet, PF-metoden							Side 1 av 2
Oppdragsnr.	Utført dato				Signatur		
Prosjekt: E39	Prøve er merket: BTM				25 år		
	Prøvens alder:						
Start forsøk:	dato:	tid (ttmm):					
Dato	Kl.	Vekt (g) etter:	Prøvestykket merket				
			BTM-1_0-50	BTM-1_50-100	BTM-1_100-150		
09.04.2018	09:00	Utpakking/Splitting - g_0	540,51	263,21	470,1		
		1 uke vannsug - g_6	542,07	263,84	471,54		
07.05.2018		1 uke tørking (105 °C) - g_1	516,09	251,33	450,37		
14.05.2018		1 uke vannsug	540,77	263,07	470,55		
14.05.2018							
14.05.2018		i vann - g_3	313,16	153	272,67		
30.05.2018		Trykkmetting i 2 døgn (luft) - g_4	550,64	267,54	479,67		
06.06.2018		1 uke tørking (105 °C) - g_7	514,25	250,5	449,01		
Målt		sidekant a / diameter d (mm)					
		sidekant b (mm)					
		høyde (mm)					
For utregninger, se formler på side 2							
Prøvestykkets volum - V (cm ³)			227,6	110,1	197,9		
Tørredensitet - ρ_t (kg/m ³)			2267,4	2283,4	2276,0		
Densitet faststoff - ρ_s (kg/m ³)			2673	2678	2672		
Sugmettet densitet ρ_s (kg/m ³)			2375,9	2390,0	2378,0		
Sugporøsitet - p_s (%)			10,84 %	10,67 %	10,20 %		
Makroporøsitet - p_m (%)			4,3 %	4,1 %	4,6 %		
Totalporøsitet - p_t (%)			15,2 %	14,7 %	14,8 %		
PF-verdi			28,6 %	27,6 %	31,1 %		
Kapillær vannmetningsgrad - DCS			94,0 %	95,0 %	93,2 %		
Total vannmetningsgrad - DS			70,7 %	73,3 %	67,3 %		

Core BSM:



210.426-3/4 Kapillær vannmetningsgrad og porøsitet, PF-metoden Side 1 av 2

Oppdragsnr. _____ Utført dato _____ Signatur _____

Prosjekt: E39 _____ Prøve er merket: _____
 Provens alder: _____

Start forsøk: _____ dato: _____ tid (ttmm): _____

Dato	Kl.	Vekt (g) etter:	Prøvestykket merket			
			BSM-1_0-50	BSM-1_50-100	BSM-1_100-150	
09.04.2018	09:00	Utpakking/Splitting - g ₀	506,36	468,10	513,28	
		1 uke vannsug - g ₆	506,37	468,81	513,88	
07.05.2018		1 uker tørking (105 °C) - g ₁	477,52	446,13	489,46	
14.05.2018		1 uke vannsug	i luft - g ₂	502,76	467,74	512,11
14.05.2018			i vann - g ₃	290,75	271,40	298,99
30.05.2018		Trykkmetting i 2 døgn (luft) - g ₄	511,02	475,49	519,55	
06.06.2018		1 uke tørking (105 °C) - g ₇	475,50	444,74	487,83	
Mål		sidekant a / diameter d (mm)				
		sidekant b (mm)				
		høyde (mm)				
For utregninger, se formler på side 2						
Prøvestykkets volum - V (cm ³)			212,0	196,3	213,1	
Tørredensitet - ρ _t (kg/m ³)			2252,3	2272,2	2296,6	
Densitet faststoff - ρ _s (kg/m ³)			2675	2672	2674	
Sugmettet densitet ρ _s (kg/m ³)			2371,4	2382,3	2402,9	
Sugporøsitet - p _s (%)			11,91 %	11,01 %	10,63 %	
Makroporøsitet - p _m (%)			3,9 %	3,9 %	3,5 %	
Totalporøsitet - p _t (%)			15,8 %	15,0 %	14,1 %	
PF-verdi			24,7 %	26,4 %	24,7 %	
Kapillær vannmetningsgrad - DCS			100,0 %	96,9 %	97,5 %	
Total vannmetningsgrad - DS			86,1 %	74,8 %	79,2 %	

Core EAM:



210.426-3/4 Kapillær vannmetningsgrad og porøsitet, PF-metoden Side 1 av 2

Oppdragsnr. _____ Utført dato _____ Signatur _____

Prosjekt: E39 _____ Prøve er merket: EAM _____
 Provens alder: _____

Start forsøk: _____ dato: _____ tid (ttmm): _____

Dato	Kl.	Vekt (g) etter:	Prøvestykket merket			
			EAM-1_0-60	EAM-1_60-100	EAM-1_100-150	
09.04.2018	09:00	Utpakking/Splitting - g ₀	577,66	221,97	558,19	
		1 uke vannsug - g ₆	581,38	223,21	561,61	
07.05.2018		1 uker tørking (105 °C) - g ₁	552,74	212,58	536,93	
14.05.2018		1 uke vannsug	i luft - g ₂	581,98	223,53	562,25
14.05.2018			i vann - g ₃	339,67	131,95	333,59
30.05.2018		Trykkmetting i 2 døgn (luft) - g ₄	589,54	225,62	567,65	
06.06.2018		1 uke tørking (105 °C) - g ₇	552,77	212,59	536,87	
Mål		sidekant a / diameter d (mm)				
		sidekant b (mm)				
		høyde (mm)				
For utregninger, se formler på side 2						
Prøvestykkets volum - V (cm ³)			242,3	91,6	228,7	
Tørredensitet - ρ _t (kg/m ³)			2281,1	2321,2	2348,2	
Densitet faststoff - ρ _s (kg/m ³)			2690	2707	2713	
Sugmettet densitet ρ _s (kg/m ³)			2401,8	2440,8	2458,9	
Sugporøsitet - p _s (%)			12,07 %	11,96 %	11,07 %	
Makroporøsitet - p _m (%)			3,1 %	2,3 %	2,4 %	
Totalporøsitet - p _t (%)			15,2 %	14,2 %	13,4 %	
PF-verdi			20,5 %	16,0 %	17,6 %	
Kapillær vannmetningsgrad - DCS			87,0 %	88,3 %	86,1 %	
Total vannmetningsgrad - DS			67,7 %	72,0 %	69,2 %	

Core ETM:



210.426-3/4 Kapillær vannmetningsgrad og porøsitet,PF-metoden Side 1 av 2

Oppdragsnr. Utført dato Signatur

Prosjekt: E39 Prøve er merket: ETM
 Provens alder:

Start forsøk: dato: tid (tt:mm):

Dato	Kl.	Vekt (g) etter:	Prøvestykket merket		
			ETM-1_0-50	ETM-1_50-100	ETM-1_100-150
09.04.2018	09:00	Utpakking/Splitting - g ₀	463,94	433,85	481,72
		1 uke vannsug - g ₆	465,20	435,09	483,02
07.05.2018		1 uke tørking (105 °C) - g ₁	440,94	413,03	460,49
14.05.2018		i luft - g ₂	465,12	434,94	482,72
14.05.2018		i vann - g ₃	270,75	253,67	283,37
30.05.2018		Trykkmetting i 2 døgn (luft) - g ₄	472,09	440,87	488,56
06.06.2018		1 uke tørking (105 °C) - g ₇	440,82	412,92	460,20
Mål		sidekant a / diameter d (mm)			
		sidekant b (mm)			
		høyde (mm)			
For utregninger, se formler på side 2					
Prøvestykkets volum - V (cm ³)			194,4	181,3	199,4
Tørredensitet - ρ _t (kg/m ³)			2268,6	2278,5	2310,0
Densitet faststoff - ρ _s (kg/m ³)			2702	2692	2689
Sugmettet densitet ρ _s (kg/m ³)			2393,0	2399,4	2421,5
Sugporøsitet - p _s (%)			12,44 %	12,09 %	11,15 %
Makroporøsitet - p _m (%)			3,6 %	3,3 %	2,9 %
Totalporøsitet - p _t (%)			16,0 %	15,4 %	14,1 %
PF-verdi			22,4 %	21,3 %	20,8 %
Kapillær vannmetningsgrad - DCS			94,8 %	94,4 %	94,2 %
Total vannmetningsgrad - DS			73,8 %	74,8 %	75,6 %

Core ESM:



210.426-3/4 Kapillær vannmetningsgrad og porøsitet,PF-metoden Side 1 av 2

Oppdragsnr. Utført dato Signatur

Prosjekt: E39 Prøve er merket: ESM
 Provens alder:

Start forsøk: dato: tid (tt:mm):

Dato	Kl.	Vekt (g) etter:	Prøvestykket merket		
			ESM-1_0-50	ESM-1_50-100	ESM-1_100-150
09.04.2018	09:00	Utpakking/Splitting - g ₀	370,71	491,75	380,96
		1 uke vannsug - g ₆	372,15	493,29	382,13
07.05.2018		1 uke tørking (105 °C) - g ₁	352,11	468,91	363,99
14.05.2018		i luft - g ₂	371,80	493,07	382,03
14.05.2018		i vann - g ₃	217,27	289,17	224,95
30.05.2018		Trykkmetting i 2 døgn (luft) - g ₄	376,62	499,58	385,66
06.06.2018		1 uke tørking (105 °C) - g ₇	351,98	468,73	363,83
Mål		sidekant a / diameter d (mm)			
		sidekant b (mm)			
		høyde (mm)			
For utregninger, se formler på side 2					
Prøvestykkets volum - V (cm ³)			154,5	203,9	157,1
Tørredensitet - ρ _t (kg/m ³)			2278,6	2299,7	2317,2
Densitet faststoff - ρ _s (kg/m ³)			2708	2707	2688
Sugmettet densitet ρ _s (kg/m ³)			2406,0	2418,2	2432,1
Sugporøsitet - p _s (%)			12,74 %	11,85 %	11,48 %
Makroporøsitet - p _m (%)			3,1 %	3,2 %	2,3 %
Totalporøsitet - p _t (%)			15,9 %	15,0 %	13,8 %
PF-verdi			19,7 %	21,2 %	16,8 %
Kapillær vannmetningsgrad - DCS			92,8 %	93,7 %	93,6 %
Total vannmetningsgrad - DS			75,9 %	74,5 %	78,3 %

Core FAM:



210.426-3/4 Kapillær vannmetningsgrad og porøsitet,PF-metoden Side 1 av 2

Oppdragsnr. _____ Utført dato _____ Signatur _____

Prosjekt: E39 Prøve er merket: FAM
 Prøvens alder: _____

Start forsøk: _____ dato: _____ tid (ttmm): _____

Dato	Kl.	Vekt (g) etter:	Prøvestykket merket						
			FAM-1_0-50	FAM-1_50-110	FAM-1_110-150				
09.04.2018	09:00	Utpakking/Splitting - g_0	542,28	553,85	445,41				
		1 uke vannsug - g_6	544,93	556,63	448,18				
07.05.2018		1 uker tørking (105 °C) - g_1	513,36	524,91	422,77				
14.05.2018		1 uke vannsug	i luft - g_2	544,72	556,64	448,01			
14.05.2018			i vann - g_3	319,70	326,35	263,90			
30.05.2018		Trykkmetting i 2 døgn (luft) - g_4	548,43	560,56	450,76				
06.06.2018		1 uke tørking (105 °C) - g_7	513,27	524,86	422,66				
Mål		sidekant a / diameter d (mm)							
		sidekant b (mm)							
		høyde (mm)							
For utregninger, se formler på side 2									
Prøvestykkets volum - V (cm ³)			225,0	230,3	184,1				
Tørredensitet - ρ_t (kg/m ³)			2281,4	2279,3	2296,3				
Densitet faststoff - ρ_s (kg/m ³)			2703	2697	2708				
Sugmettet densitet ρ_s (kg/m ³)			2420,8	2417,1	2433,4				
Sugporøsitet - p_s (%)			13,94 %	13,78 %	13,71 %				
Makroporøsitet - p_m (%)			1,6 %	1,7 %	1,5 %				
Totalporøsitet - p_t (%)			15,6 %	15,5 %	15,2 %				
PF-verdi			10,6 %	11,0 %	9,8 %				
Kapillær vannmetningsgrad - DCS			91,6 %	91,2 %	89,1 %				
Total vannmetningsgrad - DS			82,5 %	81,2 %	80,9 %				

Core FTM:



210.426-3/4 Kapillær vannmetningsgrad og porøsitet,PF-metoden Side 1 av 2

Oppdragsnr. _____ Utført dato _____ Signatur _____

Prosjekt: E39 Prøve er merket: FTM
 Prøvens alder: _____

Start forsøk: _____ dato: _____ tid (ttmm): _____

Dato	Kl.	Vekt (g) etter:	Prøvestykket merket						
			FTM-1_0-50	FTM-1_50-100	FTM-1_100-150				
09.04.2018	09:00	Utpakking/Splitting - g_0	286,44	398,61	518,64				
		1 uke vannsug - g_6	287,26	400,00	520,07				
07.05.2018		1 uker tørking (105 °C) - g_1	269,89	375,20	489,30				
14.05.2018		1 uke vannsug	i luft - g_2	286,97	399,51	519,52			
14.05.2018			i vann - g_3	168,57	232,18	304,09			
30.05.2018		Trykkmetting i 2 døgn (luft) - g_4	289,01	403,20	523,05				
06.06.2018		1 uke tørking (105 °C) - g_7	269,72	375,06	489,12				
Mål		sidekant a / diameter d (mm)							
		sidekant b (mm)							
		høyde (mm)							
For utregninger, se formler på side 2									
Prøvestykkets volum - V (cm ³)			118,4	167,3	215,4				
Tørredensitet - ρ_t (kg/m ³)			2279,5	2242,3	2271,3				
Densitet faststoff - ρ_s (kg/m ³)			2718	2693	2693				
Sugmettet densitet ρ_s (kg/m ³)			2423,7	2387,6	2411,5				
Sugporøsitet - p_s (%)			14,43 %	14,53 %	14,03 %				
Makroporøsitet - p_m (%)			1,7 %	2,2 %	1,6 %				
Totalporøsitet - p_t (%)			16,1 %	16,7 %	15,7 %				
PF-verdi			10,7 %	13,2 %	10,5 %				
Kapillær vannmetningsgrad - DCS			95,3 %	94,4 %	95,4 %				
Total vannmetningsgrad - DS			86,6 %	83,6 %	86,9 %				

Core FSM:

210.426-3/4 Kapillær vannmetningsgrad og porøsitet, PF-metoden Side 1 av 2

Oppdragsnr. _____ Utført dato _____ Signatur _____

Prosjekt: E39 _____ Prøve er merket: FSM
 Prøvens alder: _____

Start forsøk: _____ dato: _____ tid (tmm): _____

Dato	Kl.	Vekt (g) etter:	Prøvestykket merket						
			FSM-1_0-40	FSM-1_40-100	FSM-1_100-150				
09.04.2018	09:00	Utpakking/Splitting - g_0	277,35	367,94	479,63				
		1 uke vannsug - g_2	277,68	368,59	480,79				
07.05.2018		1 uker tørking (105 °C) - g_1	260,10	346,73	453,78				
14.05.2018		1 uke vannsug i luft - g_2	276,80	367,91	480,09				
14.05.2018		1 uke vannsug i vann - g_3	162,80	215,89	283,16				
30.05.2018		Trykkmetting i 2 døgn (luft) - g_4	278,30	370,22	482,96				
06.06.2018		1 uke tørking (105 °C) - g_7	259,84	346,50	453,62				
Mål		sidekant a / diameter d (mm)							
		sidekant b (mm)							
		høyde (mm)							
For utregninger, se formler på side 2									
Prøvestykkets volum - V (cm ³)			114,0	152,0	196,9				
Tørredensitet - ρ_t (kg/m ³)			2281,6	2280,8	2304,3				
Densitet faststoff - ρ_s (kg/m ³)			2715	2698	2705				
Sugmettet densitet ρ_s (kg/m ³)			2428,1	2420,1	2437,9				
Sugporøsitet - p_s (%)			14,65 %	13,93 %	13,36 %				
Makroporøsitet - p_m (%)			1,3 %	1,5 %	1,5 %				
Totalporøsitet - p_t (%)			16,0 %	15,5 %	14,8 %				
PF-verdi			8,2 %	9,8 %	9,8 %				
Kapillær vannmetningsgrad - DCS			98,1 %	97,0 %	95,7 %				
Total vannmetningsgrad - DS			94,8 %	90,3 %	88,6 %				

The following equations were applied:

$$V = \frac{g_2 - g_3}{1}$$

$$\rho_{fs} = 1000 \cdot \frac{g_1}{V - \left(\frac{g_4 - g_1}{1} \right)}$$

$$\left. \begin{aligned} p_s &= \frac{g_2 - g_1}{V \cdot 1} \\ p_m &= \frac{g_4 - g_2}{V \cdot 1} \end{aligned} \right\} p_t = p_s + p_m$$

$$DS = 100 \cdot \frac{g_0 - g_1}{g_4 - g_1}$$

Appendix 7: Chloride profile results

Measurements performed by SINTEF Community

Table 7: Chloride concentration by dry weight of concrete of reference cores (without cracks) taken from concrete Beam B

Depth	BAR	BTR	BSR
(mm)	% Cl ⁻ by dry weight of concrete		
0-3	0.433	0.444	0.666
3-6	0.343	0.352	0.594
6-10	0.285	0.312	0.56
10-15	0.247	0.274	0.55
15-20	0.183	0.257	0.473
20-30	0.079	0.161	0.37
30-40	0.02	0.074	0.292
40-50	0.005	0.036	0.218

Table 8: Chloride concentration by dry weight of concrete of reference cores (without cracks) taken from concrete Beam E

Depth	EAR	ETR	ESR
(mm)	% Cl ⁻ by dry weight of concrete		
0-3	0.27	0.245	0.305
3-6	0.327	0.281	0.373
6-10	0.235	0.223	0.269
10-15	0.185	0.169	0.228
15-20	0.119	0.105	0.163
20-30	0.033	0.036	0.073
30-40	0.005	0.005	0.023
40-50	0.005	0.005	0.005

Table 9: Chloride concentration by dry weight of concrete of reference cores (without cracks) taken from concrete Beam F

Depth	FAR	FTR	FSR
(mm)	% Cl ⁻ by dry weight of concrete		
0-3	0.279	0.495	0.676
3-6	0.194	0.362	0.527
6-10	0.165	0.302	0.474
10-15	0.138	0.228	0.45
15-20	0.07	0.175	0.39
20-30	0.033	0.053	0.333
30-40	0.005	0.02	0.212
40-50	0.005	0.005	0.083

Appendix 8: Ingress of chloride and sulfate in cracks and along reinforcement measured with μ -XRF

Figures prepared by Tobias Danner

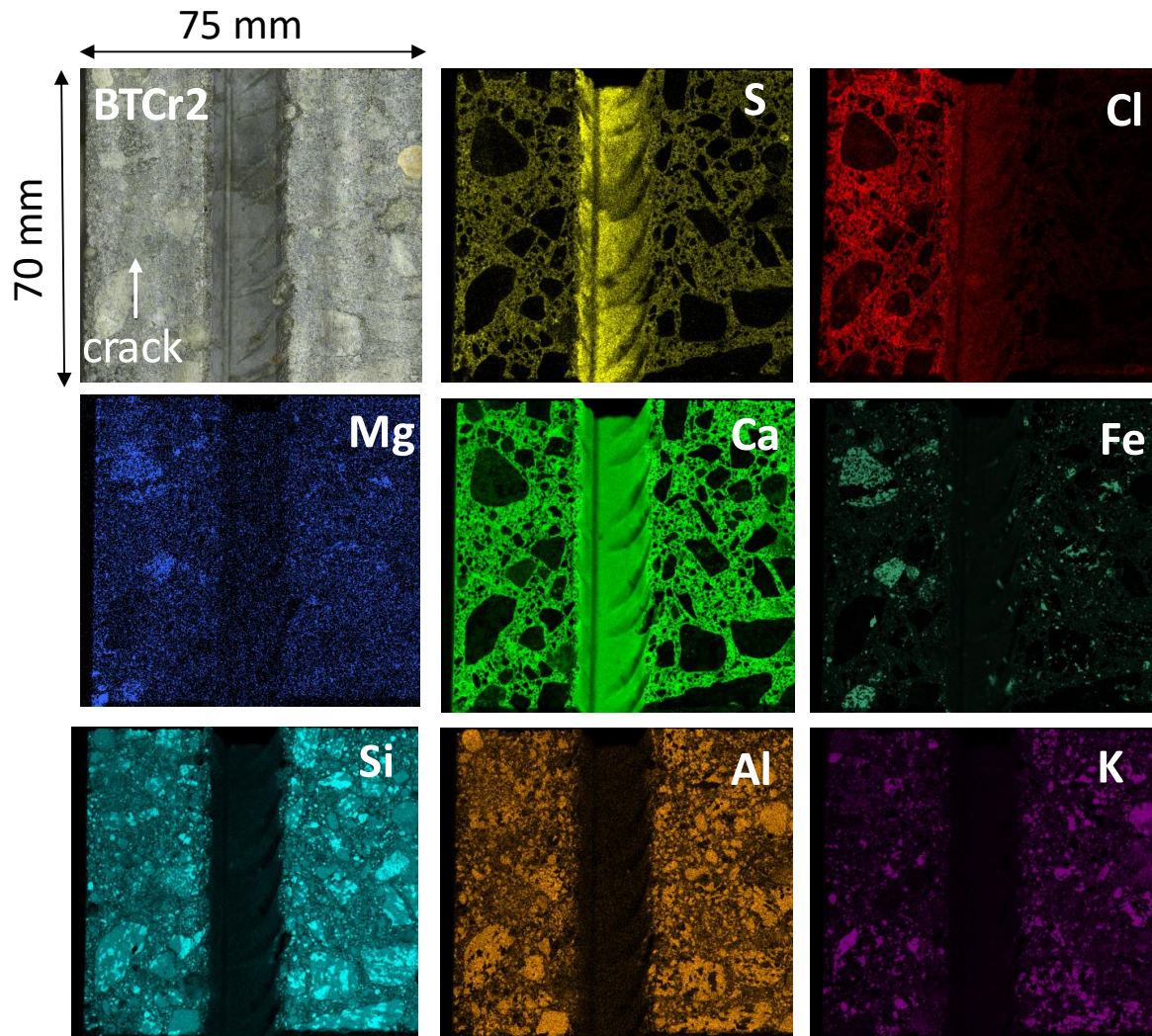


Figure 17: μ -XRF elemental mapping (S, Cl, Mg, Ca, Fe, Si, Al and K) of core BTCr2

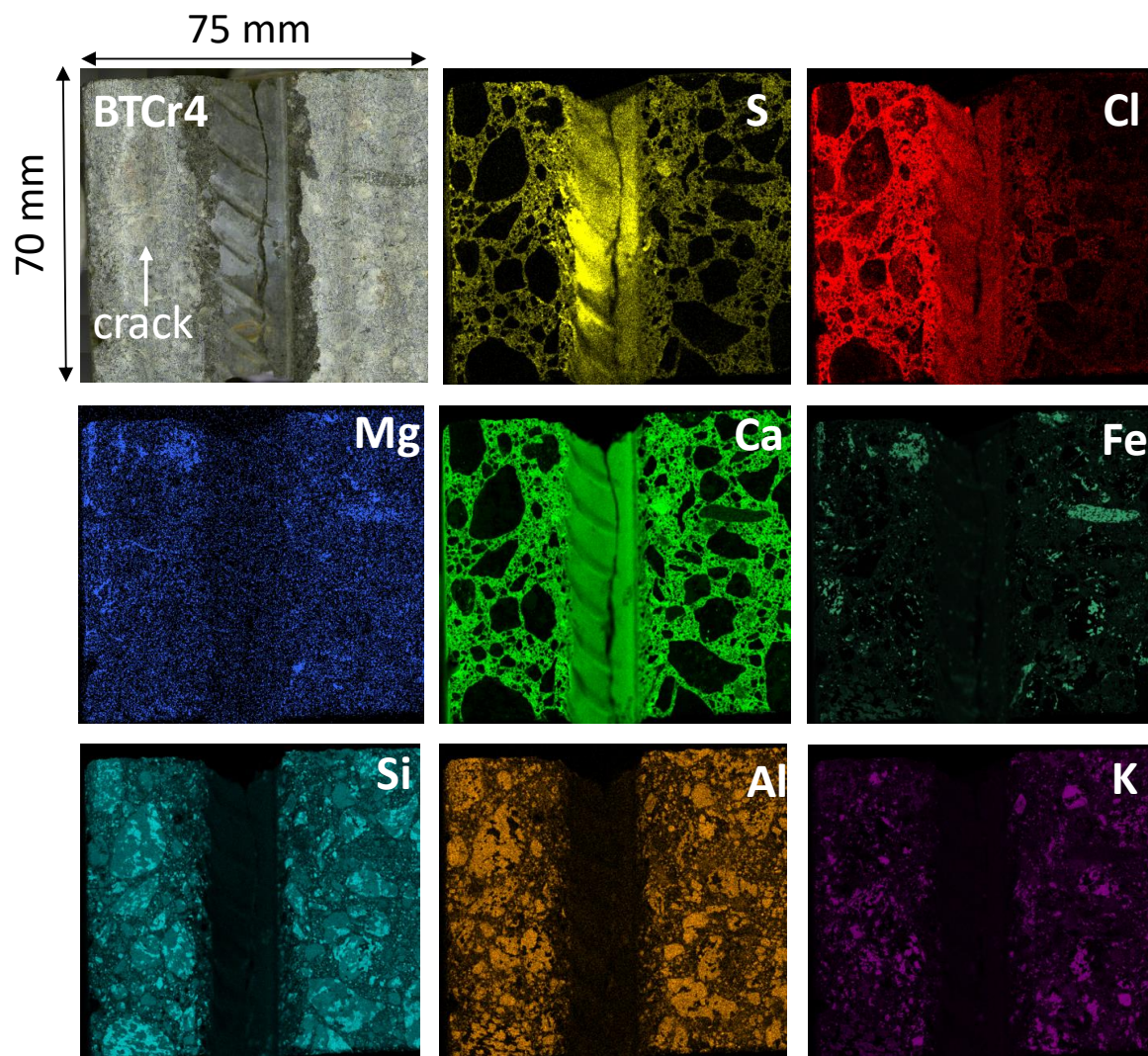


Figure 18: μ -XRF elemental mapping (S, Cl, Mg, Ca, Fe, Si, Al and K) of core BTCr4

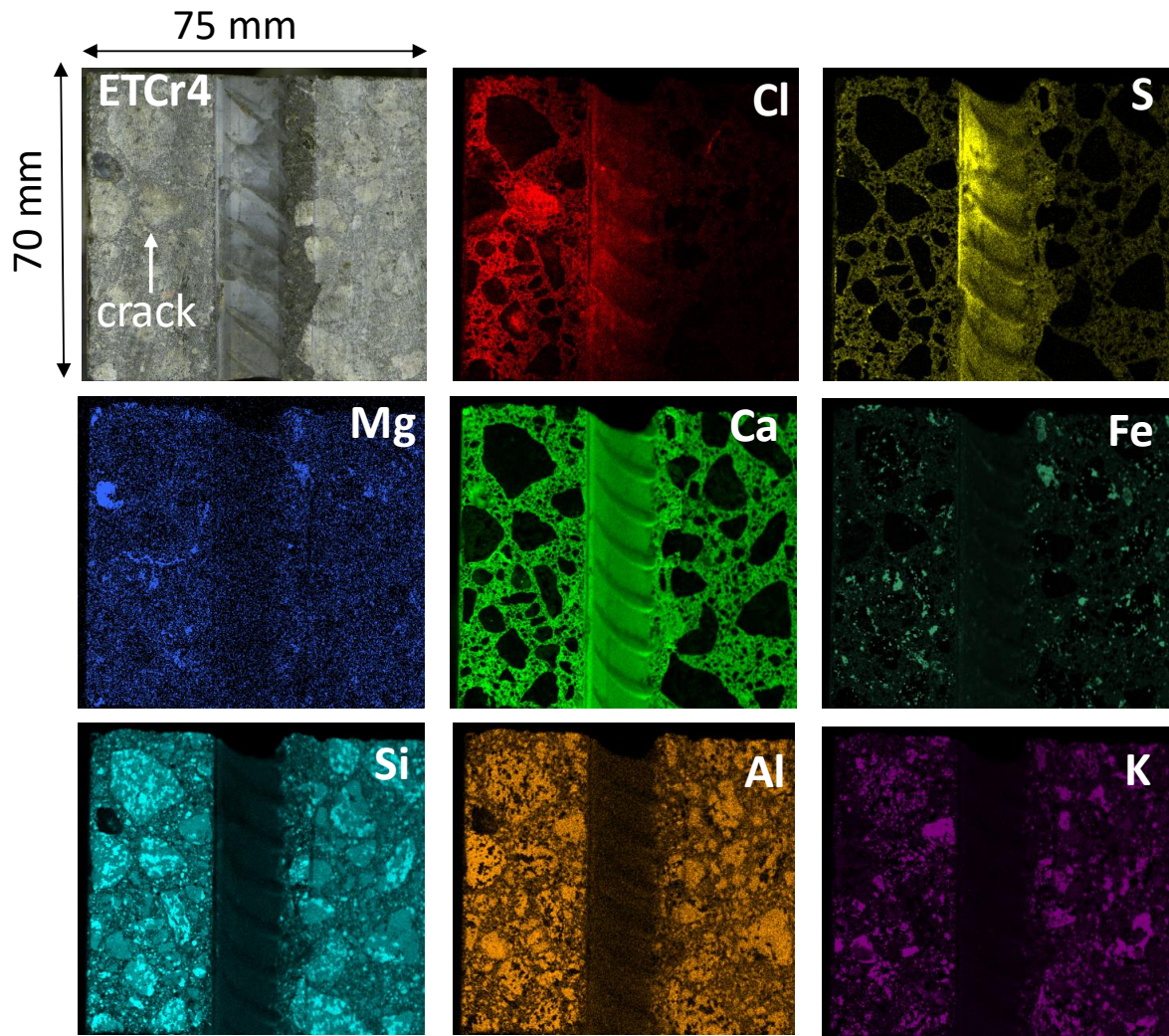


Figure 19: μ -XRF elemental mapping (S, Cl, Mg, Ca, Fe, Si, Al and K) of core ETCr4

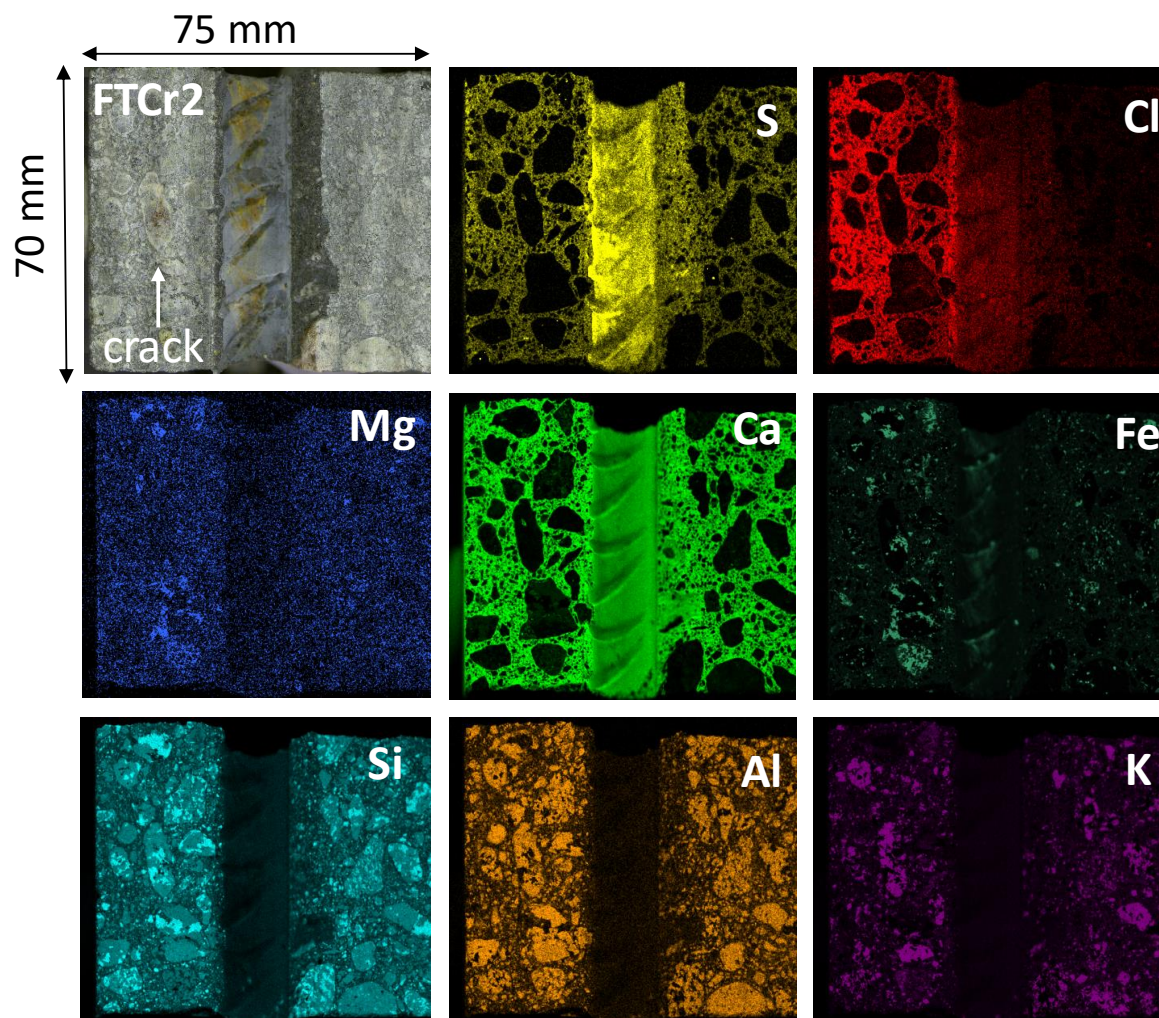


Figure 20: μ -XRF elemental mapping (S, Cl, Mg, Ca, Fe, Si, Al and K) of core FTCr2

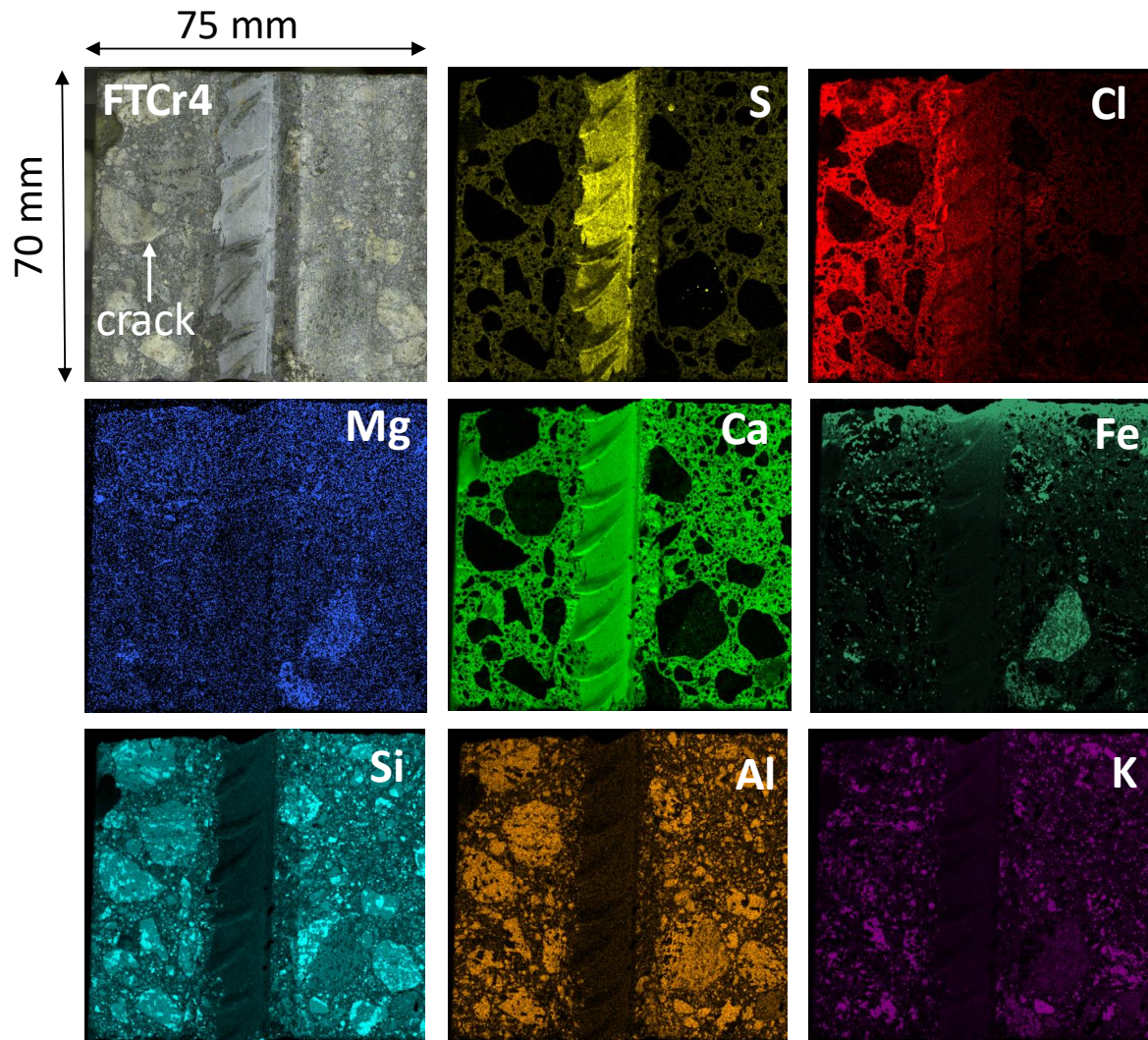


Figure 21: μ -XRF elemental mapping (S, Cl, Mg, Ca, Fe, Si, Al and K) of core FTCr4

Appendix 9: Overview and detailed pictures of self-healing in cracks

Figures prepared by Tobias Danner

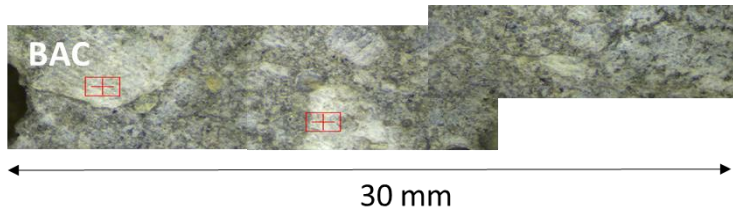


Figure 22: Overview picture of the crack in core BAC

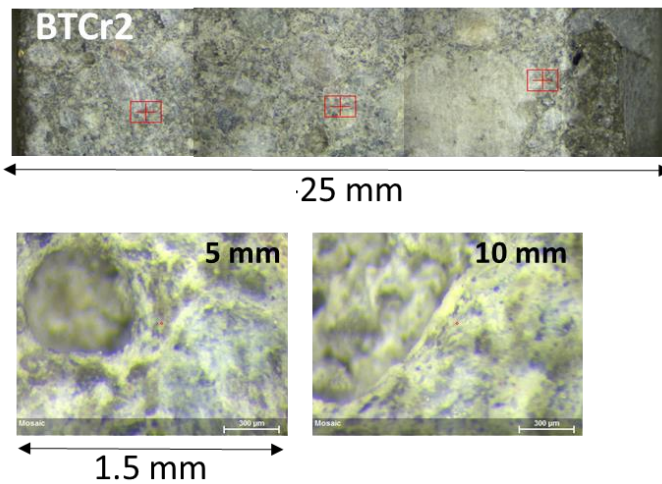


Figure 23: Overview picture and detailed pictures at different crack depth of the crack in core BTCr2

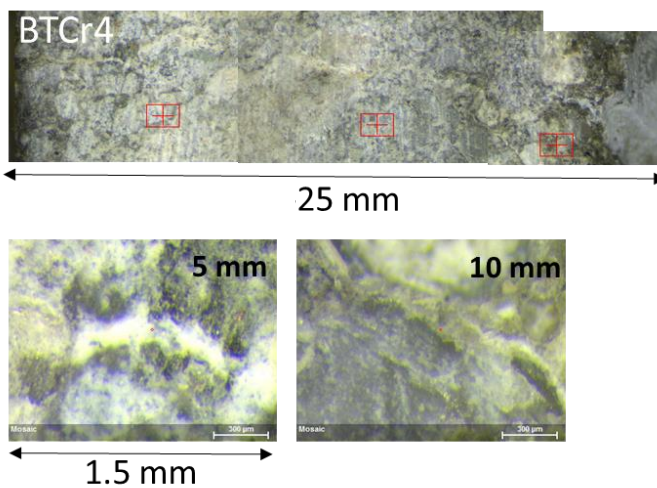


Figure 24: Overview picture and detailed pictures at different crack depth of the crack in core BTCr4

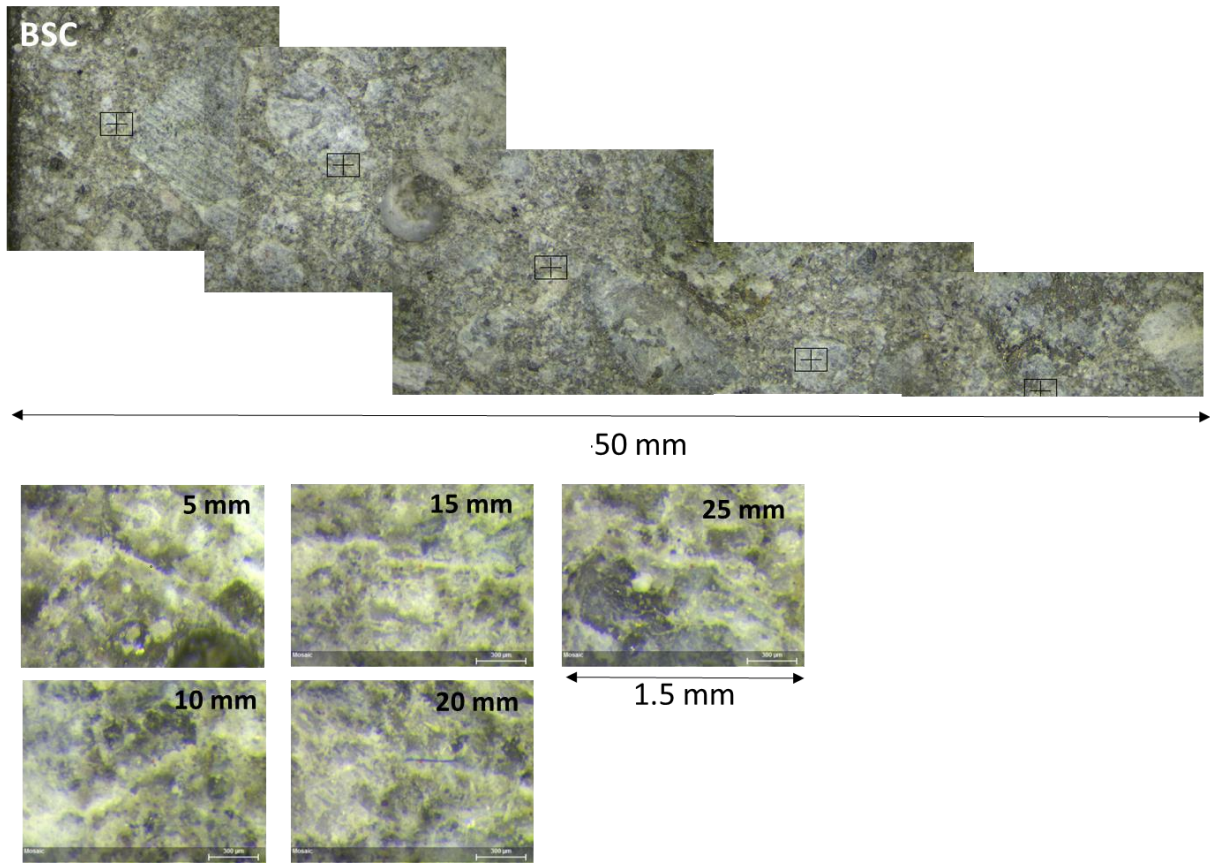


Figure 25: Overview picture and detailed pictures at different crack depth of the crack in core BSC

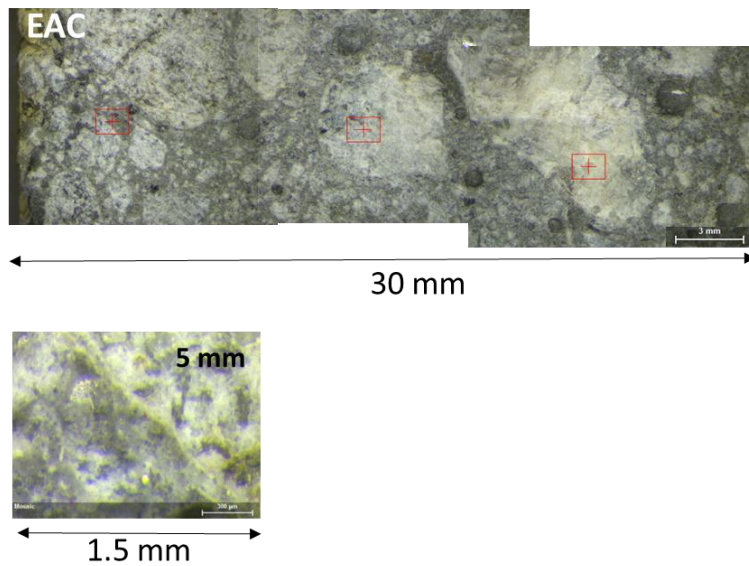


Figure 26: Overview picture and detailed pictures at different crack depth of the crack in core EAC

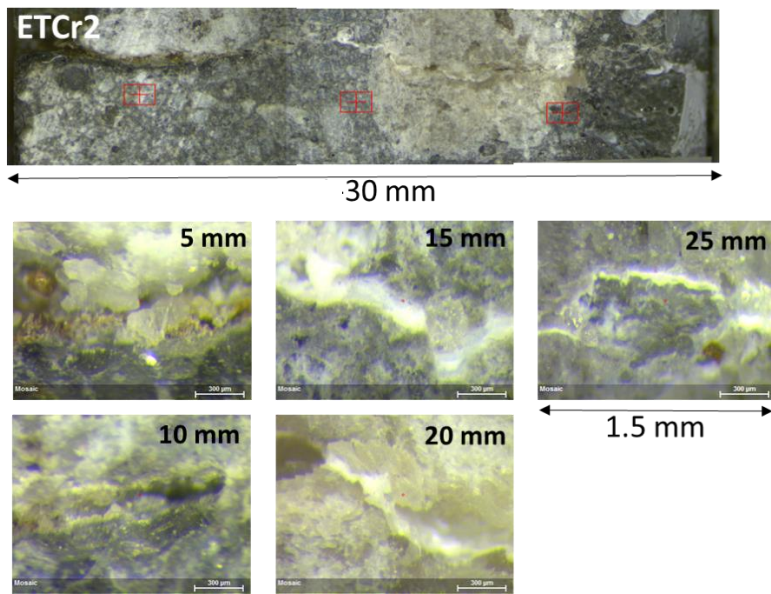


Figure 27: Overview picture and detailed pictures at different crack depth of the crack in core ETCr2

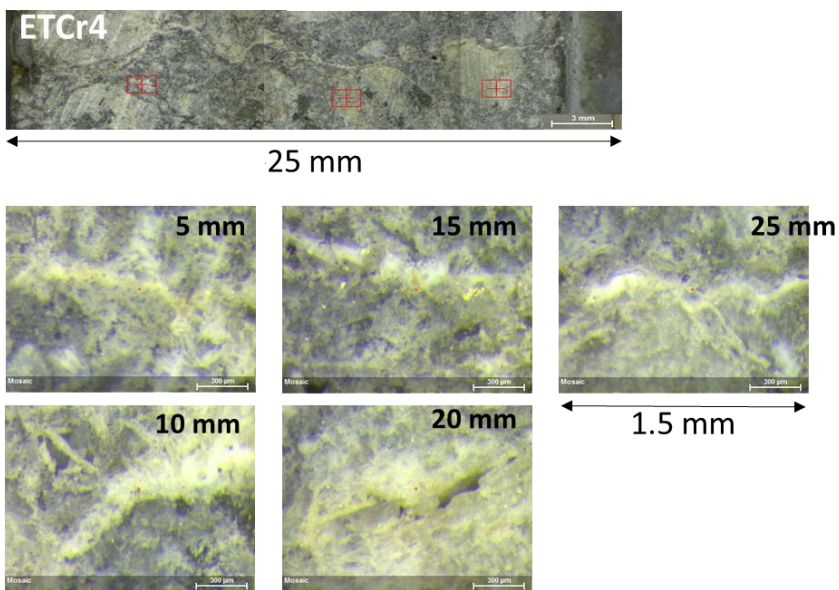


Figure 28: Overview picture and detailed pictures at different crack depth of the crack in core ETCr4

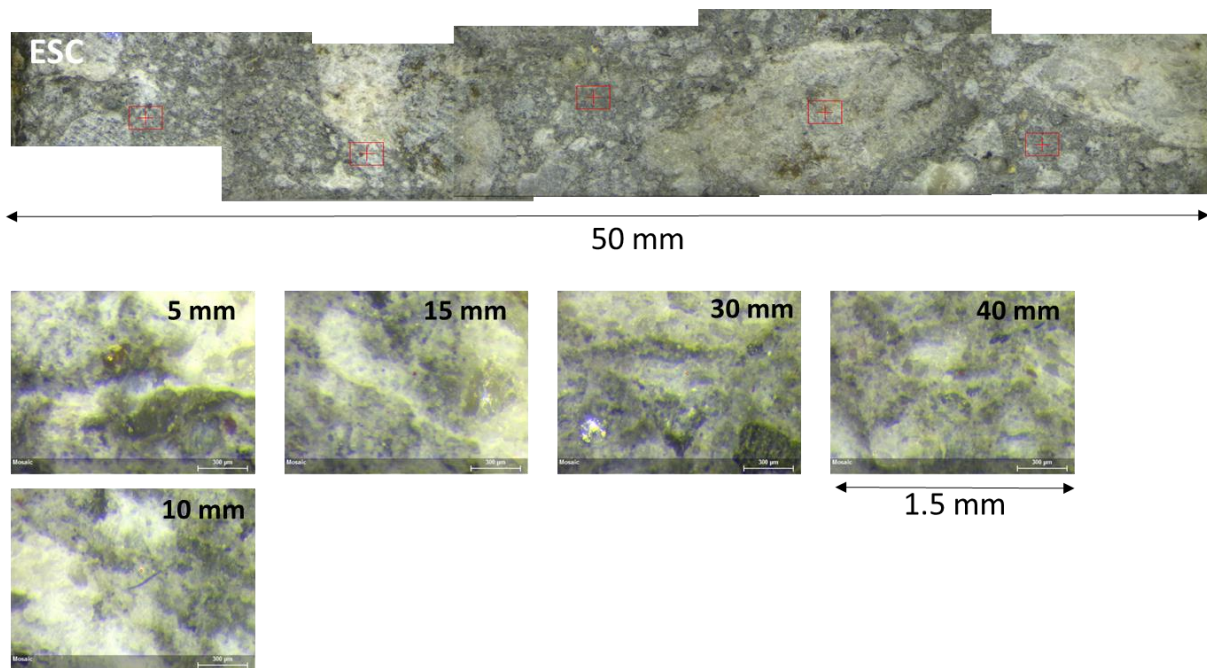


Figure 29: Overview picture and detailed pictures at different crack depth of the crack in core ESC

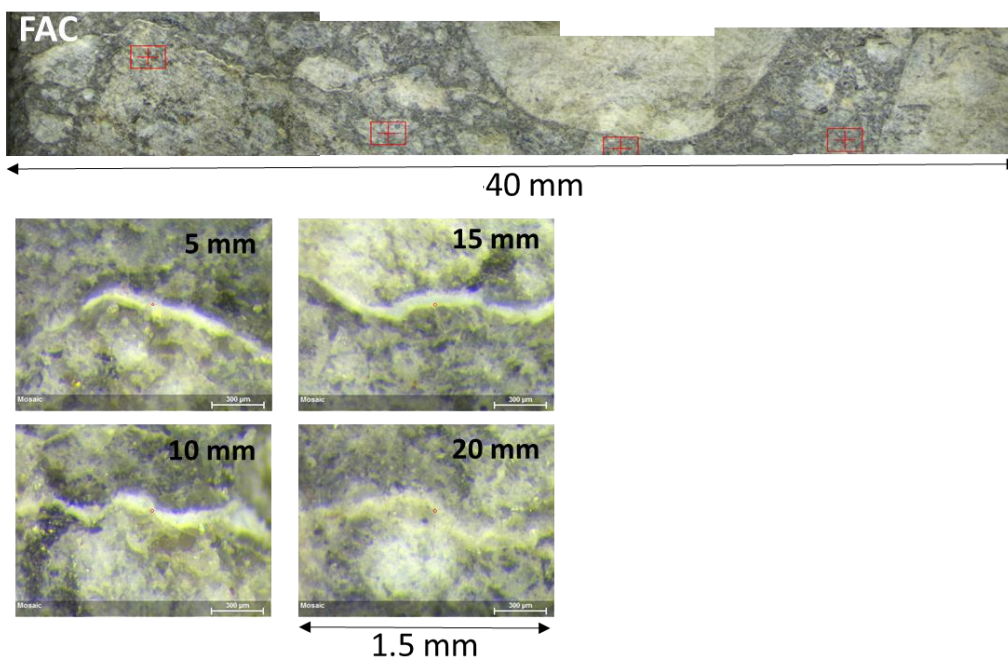


Figure 30: Overview picture and detailed pictures at different crack depth of the crack in core FAC

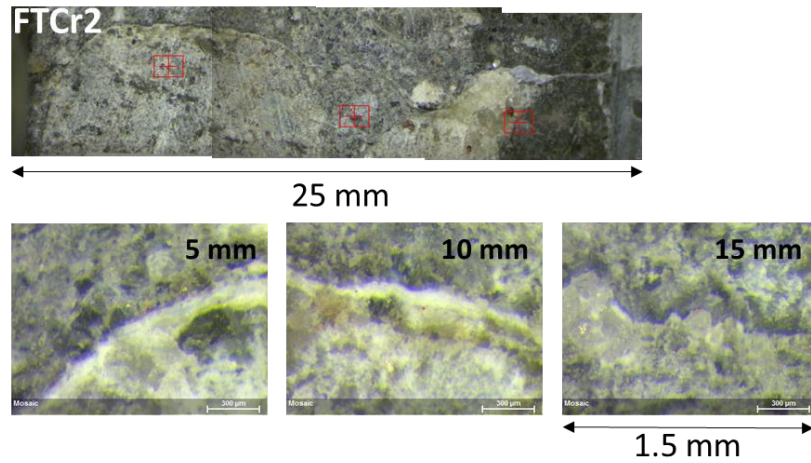


Figure 31: Overview picture and detailed pictures at different crack depth of the crack in core FTCr2

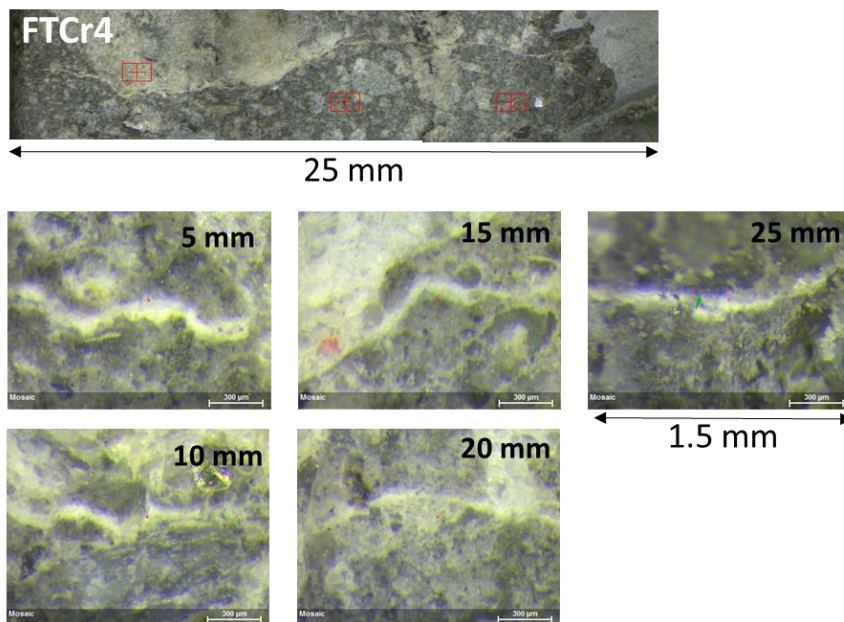


Figure 32: Overview picture and detailed pictures at different crack depth of the crack in core FTCr4

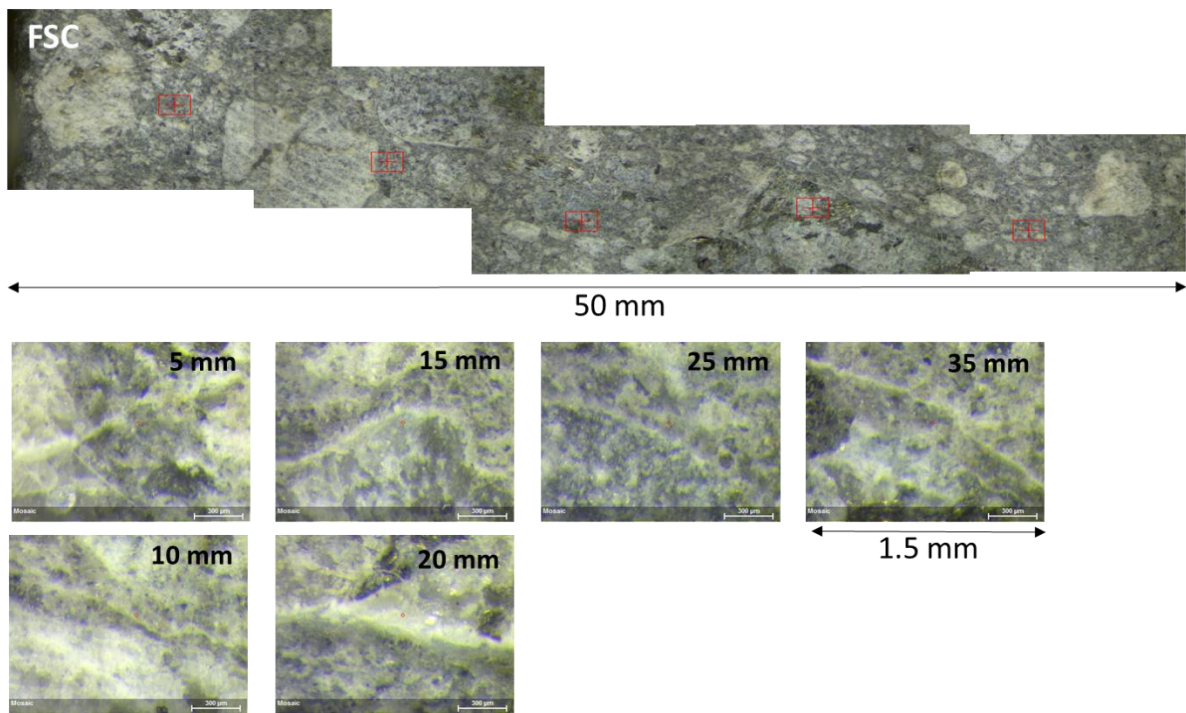


Figure 33: Overview picture and detailed pictures at different crack depth of the crack in core FSC

Appendix 10: Pictures of the split concrete beams

Pictures and figures prepared by Andres Belda Revert

First, the beams were cut in sections of ca. 50 cm in length. Table 10 presents an overview of the cut sections. Then the beams were cut longitudinally from the bottom side following reinforcement lines 2 and 4 to a depth of ca. 100 mm (without cutting the reinforcement), see Figure 34. Each of the 50 cm long pieces was then split along the cut notches. Pictures including the reinforcement imprint at line 2 and 4 are presented in Figure 35 to Figure 52. The figures include the cut and split surfaces facing the cover (C) and the bulk (B). The labelling includes <beam>-<line>-<section>-<cover/bulk>.

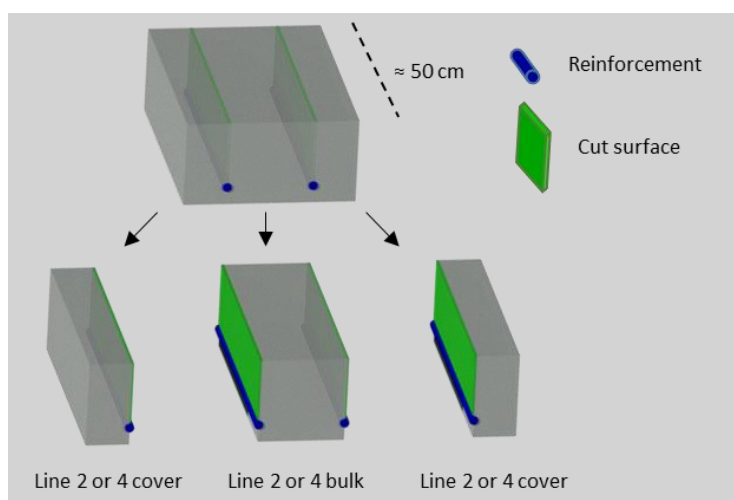


Figure 34: Illustration of cutting and splitting the concrete beams. 50 cm long sections of the beams were first longitudinally cut to a certain depth (green section) and afterwards opened using hammer and chissel

Table 10: Cut concrete sections

Beam	Line	Length (cm)	Zone
B	2 4	0-40, 40-85, 85-140, 140-200, 200-245, 245-300	Cover Bulk
E		0-45, 45-95, 95-150, 150-200, 200-250, 250-300	
F		0-45, 45-95, 95-145, 145-205, 205-255, 255-300	

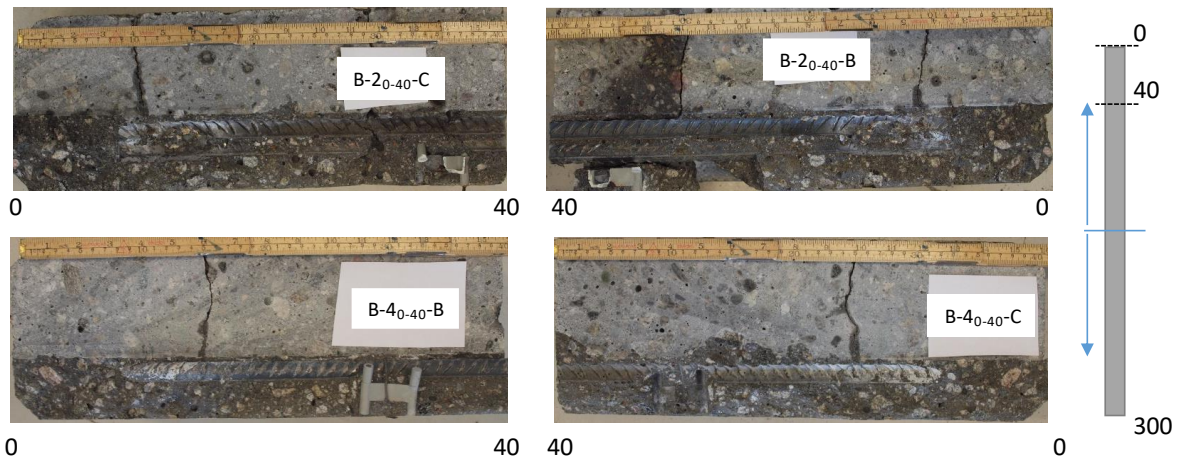


Figure 35: Steel-concrete interface of beam B section 0 to 40 cm. The large visible crack was due to the mounting of the pair of concrete beams. Near the crack white precipitate was observed at the steel-concrete interface

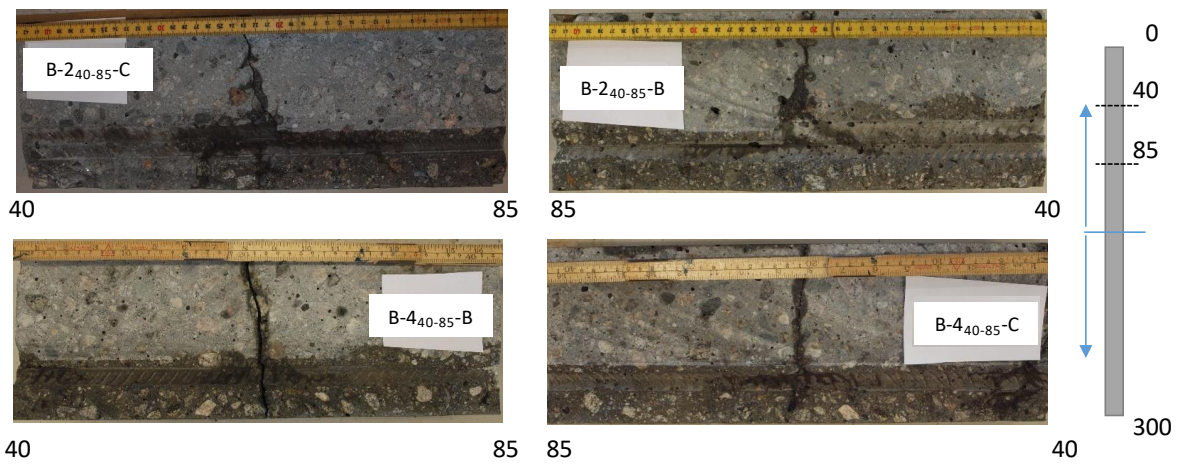


Figure 36: Steel-concrete interface of beam B section 40 to 85 cm

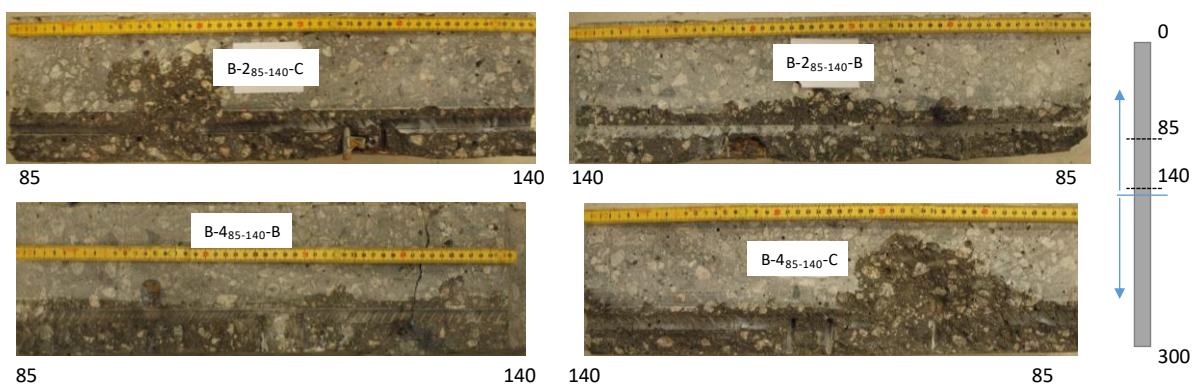


Figure 37: Steel-concrete interface of beam B section 85 to 140 cm. White precipitate at the steel-concrete interface near cracks. Localized corrosion at the spacer

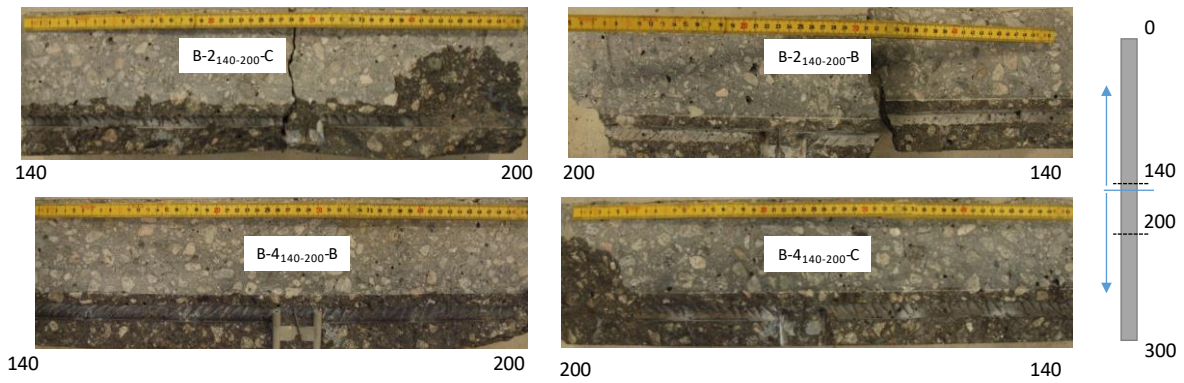


Figure 38: Steel-concrete interface of beam B section 140 to 200 cm. White precipitate at the cracks and spread over the steel-concrete interface. Localized corrosion at the spacer

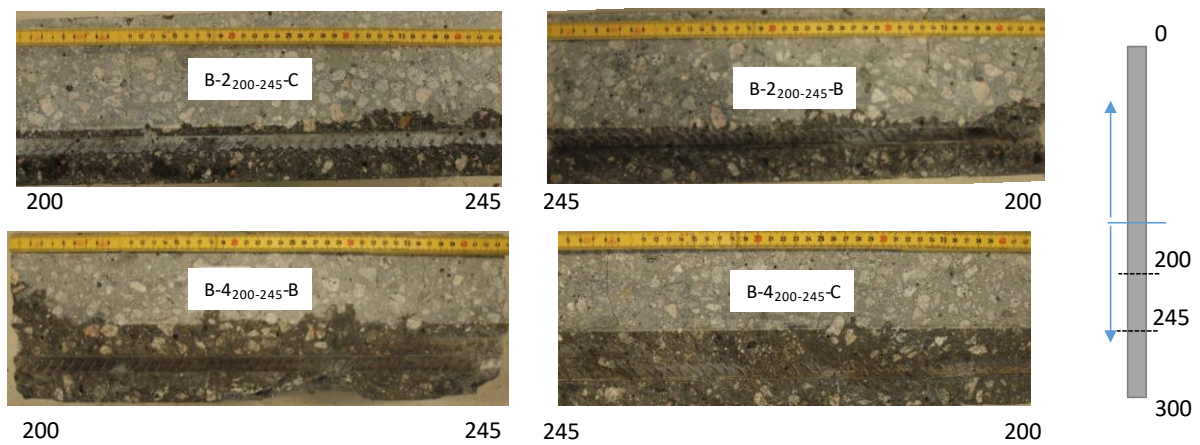


Figure 39: Steel-concrete interface of beam B section 200 to 245 cm. White precipitate at the cracks and spread over the steel-concrete interface

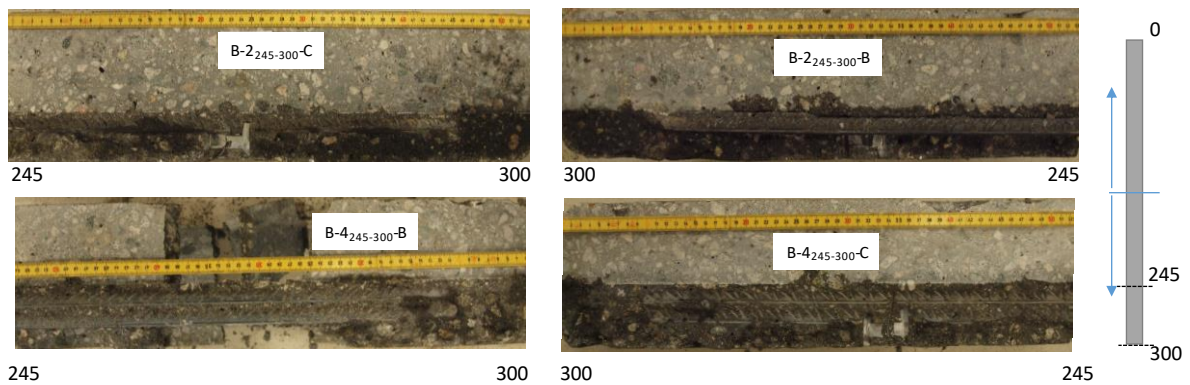


Figure 40: Steel-concrete interface of beam B section 245 to 300 cm. Localized corrosion at the spacer and distributed pitting 10 cm away from spacer

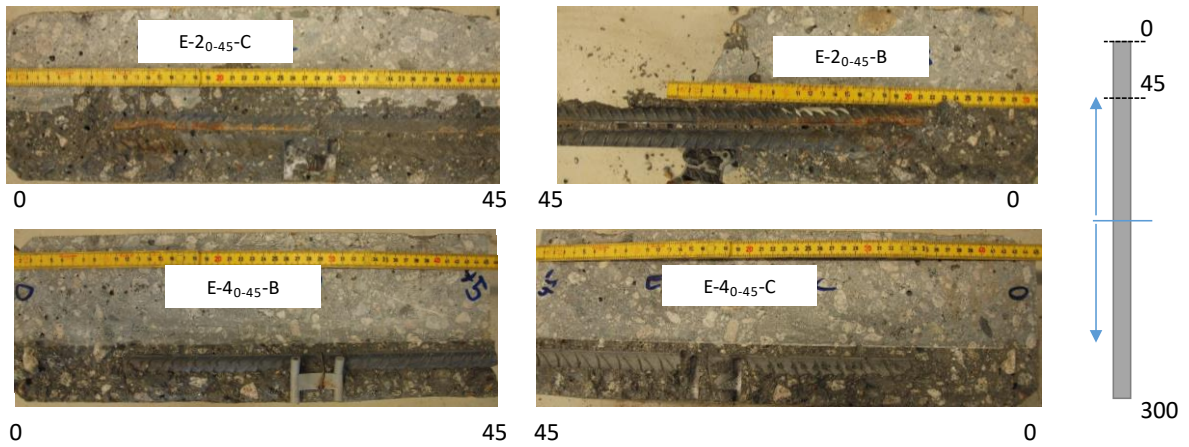


Figure 41: Steel-concrete interface of beam E section 0 to 45 cm. Superficial rust.

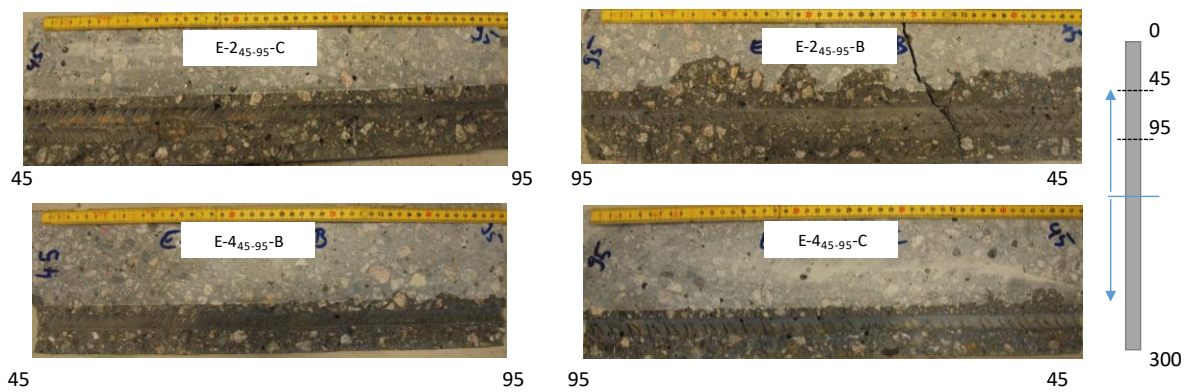


Figure 42: Steel-concrete interface of beam E section 45 to 95 cm. White precipitate at the cracks and spread over the steel-concrete interface. Superficial rust

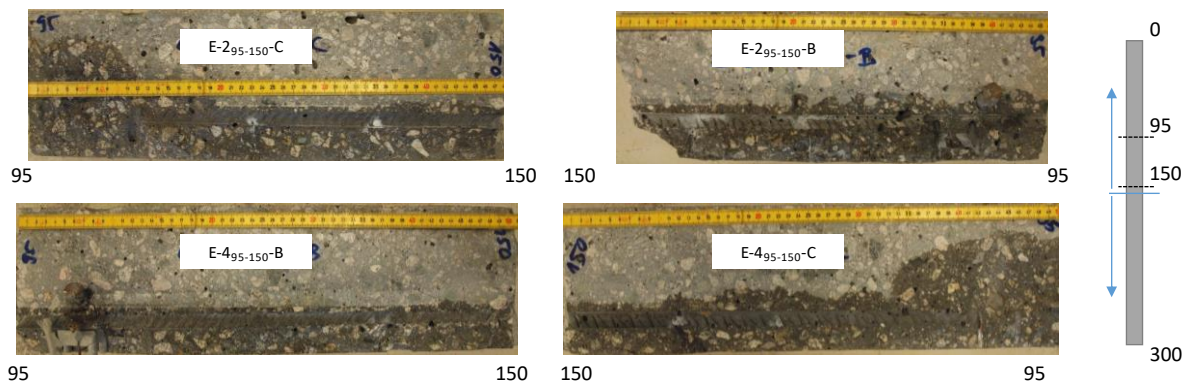


Figure 43: Steel-concrete interface of beam E section 95 to 150 cm. White precipitate at the cracks and spread over the steel-concrete interface. Localized corrosion at the spacer and a crack

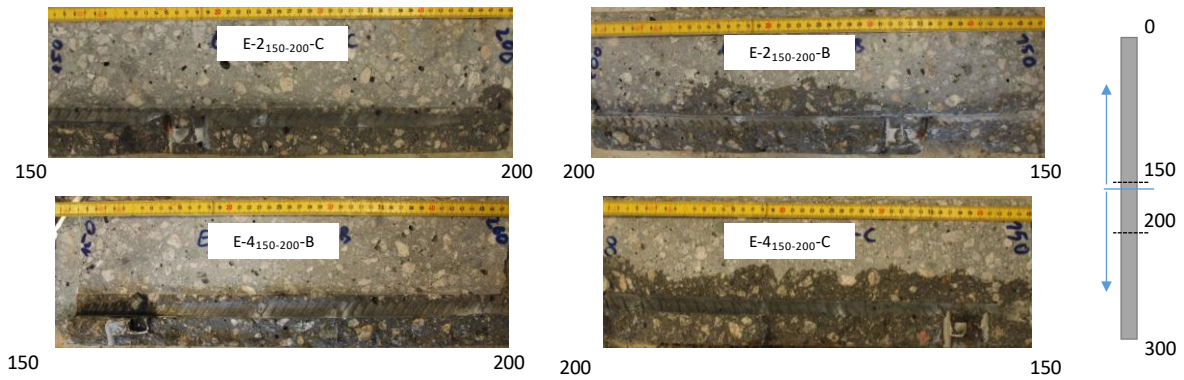


Figure 44: Steel-concrete interface of beam E section 150 to 200 cm. White precipitate at the cracks and spread over the steel-concrete interface. Localized corrosion at the spacer

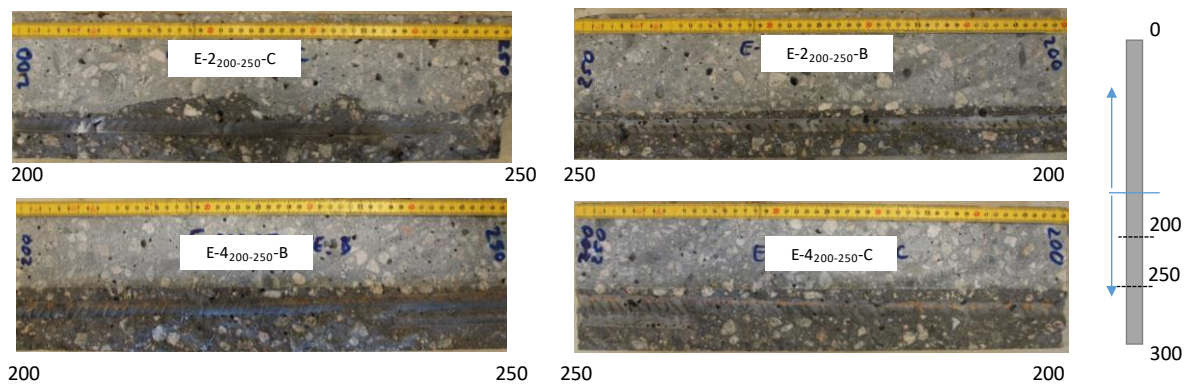


Figure 45: Steel-concrete interface of beam E section 200 to 250 cm. White precipitate at the cracks and spread over the steel-concrete interface. Superficial rust

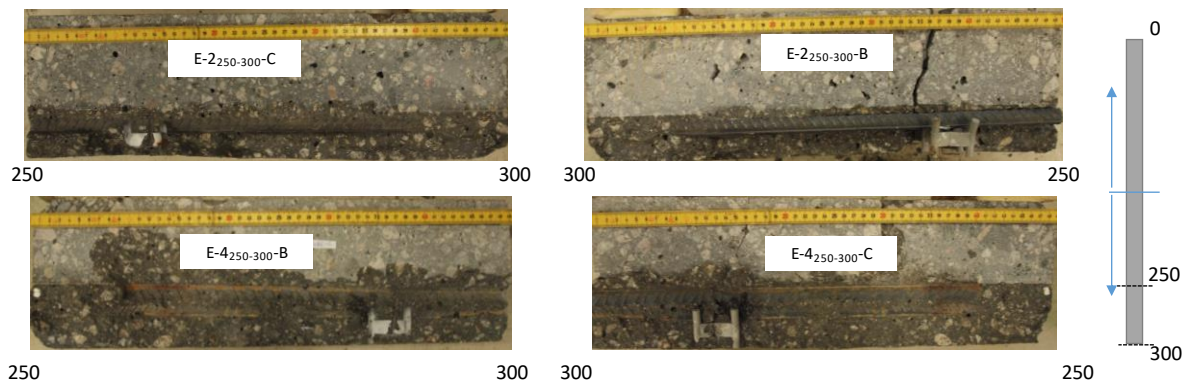


Figure 46: Steel-concrete interface of beam B section 250 to 300 cm. Superficial rust

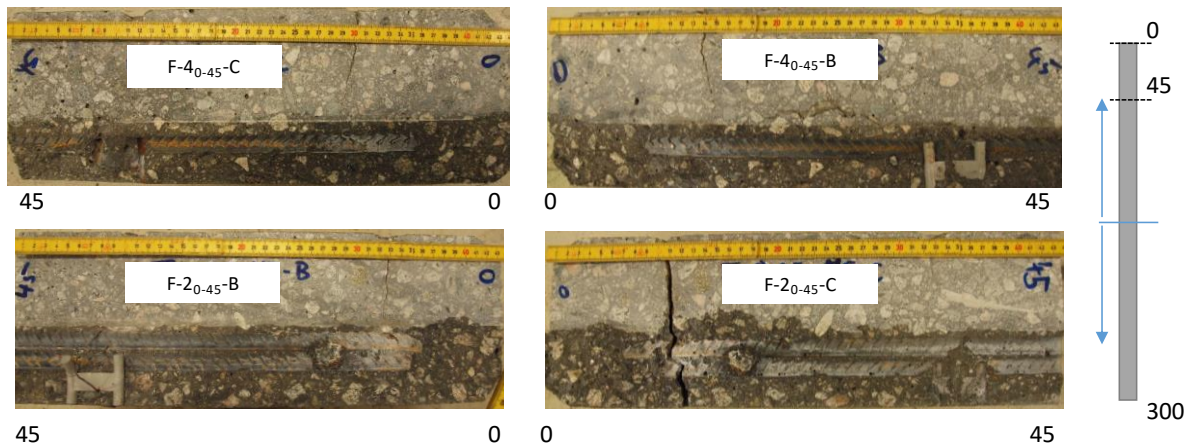


Figure 47: Steel-concrete interface of beam F section 0 to 45 cm. Crack close to the hanging-screw which presented white precipitate and spread on steel-concrete interface. Superficial rust

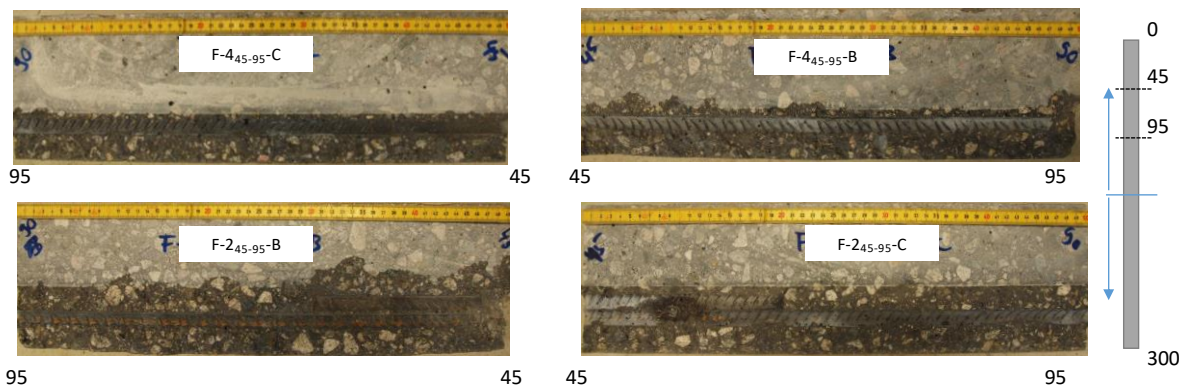


Figure 48: Steel-concrete interface of beam F section 40 to 95 cm White precipitate at the cracks and spread over the steel-concrete interface. Superficial rust

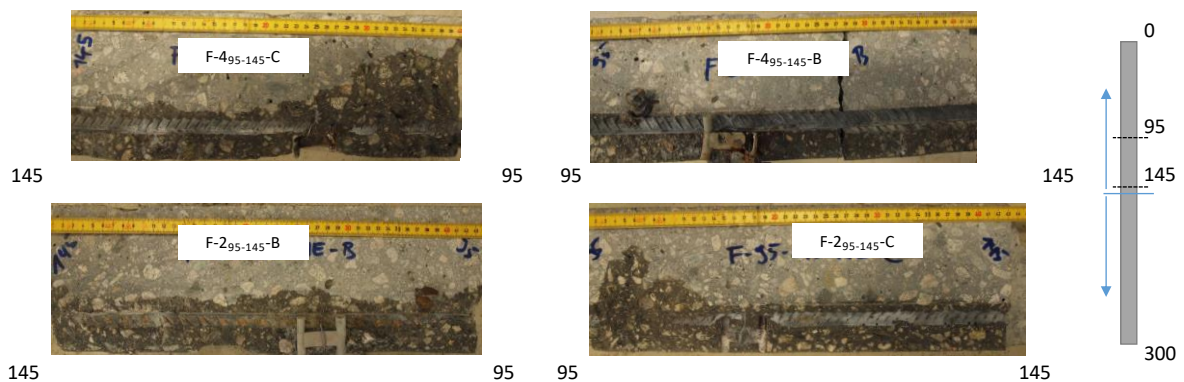


Figure 49: Steel-concrete interface of beam B section 95 to 145 cm. White precipitate at the cracks and spread over the steel-concrete interface. Superficial corrosion. Localized corrosion at the spacer

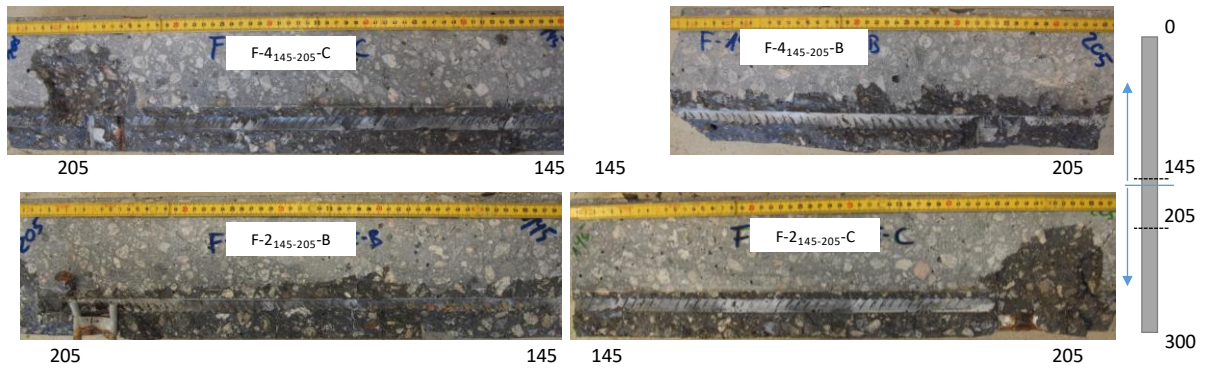


Figure 50: Steel-concrete interface of beam F section 145 to 205 cm. White precipitate at the cracks and spread over the steel-concrete interface. Localized corrosion at the spacer

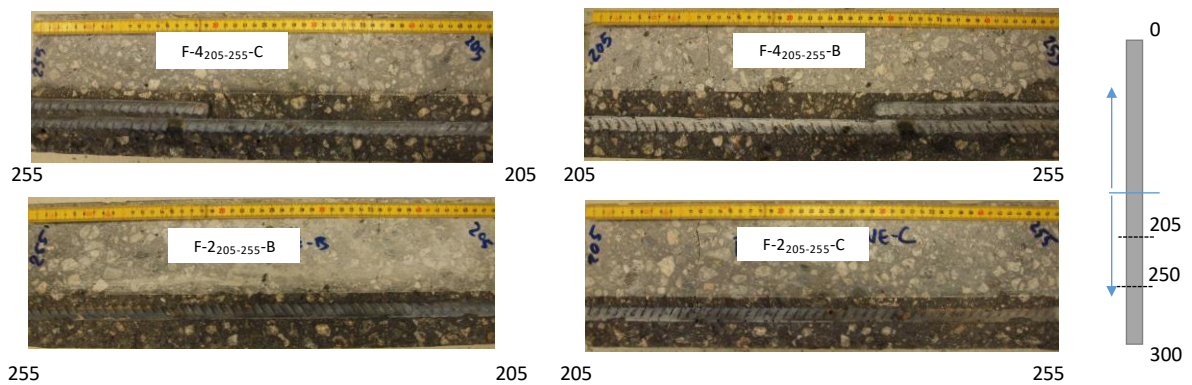


Figure 51: Steel-concrete interface of beam F section 205 to 255 cm. White precipitate at the cracks and spread over the steel-concrete interface. Superficial rust

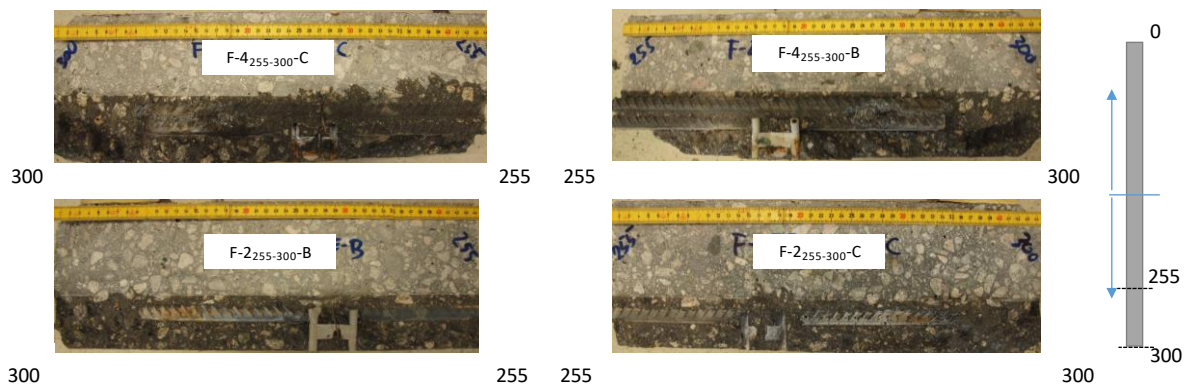


Figure 52: Steel-concrete interface of beam B section 245 to 300 cm. White precipitate at the cracks and spread over the steel-concrete interface. Superficial rust



Statens vegvesen
Pb. 1010 Nordre Ål
2605 Lillehammer

Tlf: (+47)22073000
firmapost@vegvesen.no

ISSN: 1893-1162

vegvesen.no

Trygt fram sammen